



NTNU – Trondheim
Norwegian University of
Science and Technology

Finite Element Implementation of Fibre-Reinforced Materials Model in Abaqus/Explicit

Ole Vestrum

Master of Science in Mechanical Engineering

Submission date: June 2015

Supervisor: Odd Sture Hopperstad, KT

Co-supervisor: Arild Clausen, KT
Petter Henrik Holmstrøm, KT
David Morin, KT

Norwegian University of Science and Technology
Department of Structural Engineering

MASTER'S THESIS 2015

SUBJECT AREA: Computational mechanics	DATE: June 2015	NO. OF PAGES: 14 + 108 + 10
--	--------------------	--------------------------------

TITLE:

Finite element implementation of fibre-reinforced materials model in Abaqus/Explicit.

BY:

Ole Vestrum



SUMMARY:

This thesis is concerned with the constitutive modelling of short fibre-reinforced composites in the finite element code Abaqus/Explicit. The model is presented as a generic framework which is based on a two-phase representation of the composite material. The fibres and matrix define the two phases. The fibre phase is characterised by its volume fraction and a discrete representation of the orientation distribution where each discrete representative is modelled with a simple one-dimensional elastic constitutive relation. The matrix phase is modelled with a pressure sensitive elastic-plastic mechanical behaviour, but the generic framework allows for the easy implementation of other constitutive relations as well. The contributions from both phases are scaled based on their respective volume fractions and added together to form a tangible stress state.

The model is then implemented in FORTRAN. The implementation is verified through a series of comparisons to other existing models and solutions. The verification process yielded reasonable results and the model is assumed to be working according to the established foundation.

Experimental data from uniaxial tensile tests of fibre-reinforced polypropylene retrieved from a literature source were used in the validation of the model. The validation process disclosed the potency of the model, but also some shortcomings. Finally, concrete suggestions for improving the model are presented.

RESPONSIBLE TEACHER: Professor Odd Sture Hopperstad
SUPERVISOR(S): Professor Arild Holm Clausen, Dr. David Morin and PhD candidate Petter Henrik Holmstrøm
CARRIED OUT AT: SIMLab, Department of Structural Engineering, NTNU.

MASTEROPPGAVE 2015

FAGOMRÅDE: Beregningsmekanikk	DATO: Juni 2015	ANTALL SIDER: 14 + 108 + 10
----------------------------------	--------------------	--------------------------------

TITTEL:

Implementering av materialmodell for fiberarmerte materialer i elementmetodeprogramvaren Abaqus/Explicit.

UTFØRT AV:

Ole Vestrum



SAMMENDRAG:

Denne avhandlingen tar for seg den konstitutive modelleringen av kortfiberarmerte komposittmaterialer i elementmetodeprogramvaren Abaqus/Explicit. Modellen presenteres som et generisk rammeverk hvor komposittet er representert ved to faser. Fiberene og matriksen definerer disse to fasene. Fiberfasen karakteriseres gjennom sin volumfraksjon og en diskrete representasjon av retningsfordelingen. Hver diskrete representasjon er modellert med en-dimensjonal elastisk materialoppførsel. Matriksfasen er modellert med en trykksensitiv elastisk-plastisk mekanisk oppførsel, men det generelle rammeverket åpner også for en enkel implementering av andre konstitutive modeller. Bidraget fra hver fase skaleres ut i fra deres respektive volumfraksjoner og kombineres til en endelig spenningstilstand.

Modellen implementeres så i programmeringsspråket FORTRAN. Implementasjonen verifiseres gjennom en rekke sammenligningsstudier med andre eksisterende modeller og løsninger. Verifikasjonsprosessen produserte fornuftige resultater og det forutsettes at modellen fungerer i samsvar med det etablerte rammeverket.

Eksperimentelle data fra enakset strekktester med fiberarmert polypropylen hentes fra en litteraturkilde og brukes til å validere modellen. Valideringsprosessen fremhever potensialet i modellen, men også noen mangler. Konkrete forslag til forbedringer av modellen er til slutt presentert.

FAGLÆRER: Professor Odd Sture Hopperstad
VEILEDER(E): Professor Arild Holm Clausen, Dr. David Morin og PhD kandidat Petter Henrik Holmstrøm
UTFØRT VED: SIMLab, Institutt for konstruksjonsteknikk, NTNU.

MASTER'S THESIS 2015

for

Ole Vestrum

Finite element implementation of fibre-reinforced materials models in Abaqus/Explicit

1. INTRODUCTION

Low weight and excellent formability make polymer materials attractive for an increasing number of applications. However, the comparatively low stiffness and strength of these materials is a challenge. These properties can be substantially improved by including fibres during the production process. According to today's design practice, for instance in the automotive and offshore industry, most parts in a structure, including those made of polymers, are modelled and analysed with the finite element method. To accurately predict the behaviour of the materials, the designers need reliable material models. For fibre-reinforced polymers, however, the existing models still need improvements.

2. OBJECTIVES

The research project has three main objectives: (1) to implement a material model for fibre-reinforced polymers in the nonlinear finite element code Abaqus; (2) to verify and validate the implementation by use of experimental, analytical and numerical results from the literature; (3) to apply the material model in a parametric study on the behaviour of fibre-reinforced polymer components.

3. A SHORT DESCRIPTION OF THE RESEARCH PROJECT

The main topics in the research project will be as follows;

1. Literature review: Perform a literature review on the behaviour and modelling of fibre-reinforced polymers and on characterization methods for fibre content and fibre distribution.
2. Model formulation: Establish the mathematical formulation of the material model for fibre-reinforced polymers.
3. Numerical implementation: Establish the algorithms for integration of the rate constitutive equations and implement the material model in Abaqus.
4. Verification and validation: Use existing experimental, analytical and numerical results to verify and validate the implemented material model.
5. Parameter identification: Establish a method for identifying the model parameters based on experimental data with particular emphasis on the effects of the fibres.
6. Numerical study: Perform a parametric study on the behaviour of fibre-reinforced polymer components as a function of the fibre content and fibre distribution.

Supervisors: Petter Henrik Holmstrøm, Arild Clausen, Odd Sture Hopperstad, David Morin (NTNU)

The candidate may agree with the supervisors to pay particular attention to specific parts of the investigation, or to include other aspects than those already mentioned. The thesis must be written as a research report, according to current requirements and submitted to Department of Structural Engineering, NTNU, no later than June 10th, 2015.

NTNU, January 14th, 2015

Odd Sture Hopperstad
Professor

Acknowledgements

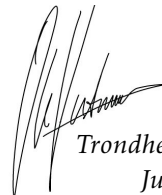
The thesis presented herein was conducted at, the Centre for Research-based Innovation, Structural Impact Laboratory (SIMLab) which is housed at the Department of Structural Engineering at the Norwegian University of Science and Technology during the spring of 2015.

I would like to express my heartfelt gratitude to each and everyone of my supervisors. Their contributions were numerous and not easily summarised, but here goes:

- My main supervisor Professor Odd Sture Hopperstad for his unprecedented guidance in moments of despair —no questions I ever had were left unanswered.
- Professor Arild Holm Clausen for sharing his extraordinary insight in the complex field of polymeric materials.
- Dr. David Morin for his significant contributions to the software aspects of this thesis. The implementation of the matrix model used herein is accredited him.
- PhD candidate Petter Henrik Holmstrøm for his continuous support, positive nature and practical understanding.

I would not only like to commend them for their outstanding individual support, but also their excellent collective guidance during our weekly meetings. Every single one of them contributed with their individual expertise which have made this thesis possible. Their efforts have truly been invaluable.

I also want to extend a special thanks to my fellow students Bjørn Håkon Frødal, Bjørn Harald Snersrud and Heidi Valle for their inputs to both relevant and irrelevant discussions at the lunch table. A thanks is also due to Teodor Heggelund for providing opinions on preliminary drafts of this thesis report.



*Trondheim, Norway
June 10, 2015*

Abstract

This thesis is concerned with the constitutive modelling of short fibre-reinforced composites in the finite element code Abaqus/Explicit. The model is presented as a generic framework which is based on a two-phase representation of the composite material. The fibres and matrix define the two phases. The fibre phase is characterised by its volume fraction and a discrete representation of the orientation distribution where each discrete representative is modelled with a simple one-dimensional elastic constitutive relation. The matrix phase is modelled with a pressure sensitive elastic-plastic mechanical behaviour, but the generic framework allows for the easy implementation of other constitutive relations as well. The contributions from both phases are scaled based on their respective volume fractions and added together to form a tangible stress state.

The model is then implemented in FORTRAN. The implementation is verified through a series of comparisons to other existing models and solutions. The verification process yielded reasonable results and the model is assumed to be working according to the established foundation.

Experimental data from uniaxial tensile tests of fibre-reinforced polypropylene retrieved from a literature source were used in the validation of the model. The validation process disclosed the potency of the model, but also some shortcomings. Finally, concrete suggestions for improving the model are presented.

Contents

- Acknowledgements i
- Abstract iii

- 1 Introduction 1**
 - 1.1 Motivation 1
 - 1.2 Objectives 2
 - 1.3 Scope 3
 - 1.4 Overview of thesis 3

- 2 Essential theory 5**
 - 2.1 Expected prior knowledge 5
 - 2.2 Materials science 5
 - 2.2.1 Directional dependency 5
 - 2.2.2 Composite materials 6
 - 2.2.3 Injection molding 9
 - 2.3 X-ray computed tomography 9
 - 2.4 Materials mechanics 10
 - 2.4.1 Large deformations 10
 - 2.4.2 Constitutive relation 13
 - 2.4.3 Transformation of stress 17
 - 2.5 Euclidean space 18
 - 2.5.1 Spherical coordinate system 18
 - 2.5.2 Coordinate system conversion 19
 - 2.5.3 Coordinate transformations 19
 - 2.6 Statistical theory 20
 - 2.6.1 Normal distribution 20

2.6.2	Monte Carlo cycles	22
2.7	Abaqus interface	23
2.7.1	Subroutine interfaces	23
2.7.2	The Abaqus Scripting Interface	24
3	Short Fibre-Reinforced Materials - model	27
3.1	Framework	27
3.1.1	Matrix phase	28
3.1.2	Fibre phase	29
3.1.3	Combining of phases	30
3.1.4	Discretisation of fibre orientation	31
3.2	Pseudo formulation	36
3.3	FORTRAN implementation	39
3.3.1	Source code structure	39
3.4	Applied matrix model	40
3.5	User-defined parameters	41
4	Verification	43
4.1	Preliminary controls	43
4.2	Comparison with native Abaqus model	44
4.3	Comparison with semi-analytical solution	45
4.3.1	Model and analyses description	45
4.3.2	Results	47
4.4	Comparison with literature	47
4.4.1	Model and analyses description	49
4.4.2	Uncertainties in the comparison	51
4.4.3	Results from tension	52
4.4.4	Results from compression	52
4.5	Evaluation of verification	52
5	Validation	59
5.1	Materials	59
5.2	Calibration of the SFRM-model	60
5.2.1	Weight fraction conversion	60
5.2.2	Calibration of matrix model	61
5.3	Tensile test specimen	67

5.3.1	Finite element model	67
5.4	Fibre orientation distribution mapping	71
5.4.1	Scan of PP10 sample	71
5.4.2	Analysis of PP10 sample	74
5.5	Comparison with experimental results	77
5.5.1	PP	79
5.5.2	PP10	79
5.5.3	PP30	85
5.6	Evaluation of validation	89
6	Conclusion	93
7	Future work	97
7.1	Failure modes	97
7.2	Constitutive modelling of fibre phase	98
7.3	Including other fibre properties	99
7.4	Development of fibre distribution cases	101
7.5	Further exploration	102
	Bibliography	103
A	Source code	109
A.1	SFIBER.for	109
A.2	SFD.for	113

Chapter 1

Introduction

1.1 Motivation

In an ever demanding technological era, the interaction between material and component design is becoming increasingly important. High requirements in material properties such as formability, weight, stiffness, strength and especially the combinations of all of these, often make traditional engineering materials such as metals, insufficient. As a results of this increase in efficiency requirements, the spotlight shines increasingly brighter on composite materials. The automotive industry is just one of the examples of industries that embraces and develop the potential in these kind of materials.

There are numerous attempts for estimating the macroscopic mechanical response for composites based on microscopic properties. Kelly and Tyson [1] presents the basic concept of the now well known rule-of-mixture which weights the phase contribution based on volume fraction. Bowyer and Bader [2] accounts for the length and orientation of the fibres by enriching the rule-of-mixture by correctional parameters. More recent models have also been developed [3, 4]. According to present day demands, more complex methods of analysis are needed. Today, many structures are analysed with the finite element method which needs reliable material models to properly predict the capabilities of components [5, 6]. Notta-Cuvier et al. presented an efficient material model for short fibre-reinforced composites in [7] in 2013. The proposed model uses a two-dimensional representation of the fibre orientations within the fibre phase. The contribution from all fibres are calculated based

on the mechanical response of discrete fibre representatives. The individual responses are superimposed through a rule-of-mixture along with the contribution from the matrix phase. Some of the same authors have proposed extensions of the model in [7] in a series of papers [8, 9, 10] where more complex fibre orientations and implementation of damage phenomena in both matrix and fibres have been included. Large parts of the thesis herein has been concerned with creating and implementing a very similar model to the one proposed in [7]. The model described in [7] is essentially a framework which can be easily remodelled to be used along with existing models developed at SIMLab.

Although the popularity in the study of short fibre-reinforced composites has been on composites where fibres are applied as reinforcements to polymers, the application for the following concepts is not necessarily restricted to reinforced plastics as demonstrated in [7]. The model presented in this thesis is therefore dubbed the *Short Fibre-Reinforced Materials*-model or simply the *SFRM*-model.

1.2 Objectives

The objective of this thesis is to create and quality assure the foundation and implementation of a constitutive material model for short fibre-reinforced materials which takes the distribution of fibre orientations and fibre volume content into account. The objective is divided into sub-objectives which includes

1. the establishment of the mathematical foundation for the material model,
2. the implementation of the material model to be used in the nonlinear finite element code Abaqus/Explicit,
3. a verification process of the implementation by comparison with existing solutions,
4. and a validation process of the established model through comparison with experimental uniaxial tensile data.

1.3 Scope

The scope of the thesis presented herein is confined to the following:

- Rate-independent constitutive modelling of both phases.
- No modelling of damage for fibres, matrix nor fibre/matrix-interphase.
- Verification and validation are confined to uniaxial tensile test specimens.

1.4 Overview of thesis

This thesis report is divided into chapters which presents the development of the SFRM-model in chronological order. A short description of each chapter is found below.

Chapter 2: Essential theory

Chapter 2 contains a presentation of the theoretical foundation which is needed to fully grasp the concepts and results presented herein.

Chapter 3: SFRM-model

Chapter 3 presents the SFRM-model starting with the overall framework and ending with the actual source code implementation. The chapter is designed to give the reader a structured and intuitive understanding of the model through illustrations and pseudo formulations of various notions.

Chapter 4: Verification

Chapter 4 sets out to present the verification process of the implemented model. The chapter presents an outline of the preliminary controls made during development and a series of comparisons of the SFRM-model to different solutions.

Chapter 5: Validation

Chapter 5 applies the SFRM-model to experimental tensile test results of fibre-reinforced polypropylene retrieved from the master's thesis of Anne Amundsen [11].

Chapter 6: Future work

Chapter 6 presents concrete suggestions for future development and work related to the SFRM-model.

Chapter 7: Conclusion

Chapter 7 presents a summary of the results produced in this thesis along with concluding remarks.

Chapter 2

Essential theory

2.1 Expected prior knowledge

When reading this thesis, the reader is presumed to have prior knowledge in the fields: materials mechanics, continuum mechanics, numerical methods, linear algebra, computer programming, material science, statistical theory and the Abaqus FEA software suite. The following sections are meant to give the reader an understanding of the theories which are needed to fully understand the SFRM-model. It is not meant as an thorough introduction, but as a refreshment of prior knowledge. In order to fully grasp the concepts, the reader is referred to the listed literature references at the end of each section. The theory presented in the following sections are based upon these listed sources.

2.2 Materials science

2.2.1 Directional dependency

If a material's properties are invariant of direction, the material properties are said to be *isotropic*. Material properties that exhibits different behaviour with respect to material direction is said to be *anisotropic*. The degree of anisotropy that a property may exhibit is related to the degree of symmetry within the material. Several material processes may introduces anisotropic behavior in a material such as extrusion of component members and reinforcements in a composite.

For a better understanding on the topic of the directional dependencies of material properties, the reader is referred to [12, 13, 14].

2.2.2 Composite materials

The field of composites is as vast as it is complex. This section sets aim to give the reader a notion of the type of composites and material phenomena which the SFRM-model seeks to model.

While composites can be said to have existed for a long time in nature in the form of materials such as wood and bone the popularity of these tailor-made materials have greatly risen during the past decades. Callister and Rethwisch [14] gives a general definition of composites; *...a composite is considered to be any multiphase material that exhibits a significant proportion of the properties of both constituent phases such that a better combination of properties is realized.* The constituent phases are chemically different and have a distinguishable interface that separates them. Although they can be made up of multiple constituent phases, composites often consist of only two. One phase is dispersed in the other. The continuous and surrounding phase is known as the *matrix phase* and holds the second phase which is known as the *dispersed phase*. A general categorisation of composites can be made based on the geometry of the dispersed phase. Figure 2.1 illustrate a simple hierarchical classification of some different composite types. The bluish coloured path in the figure is the topical composite type for this thesis.

Common materials used as the matrix phase are polymers, metals and ceramics. Due to lack of toughness in ceramic materials, the introduction of a dispersed phase, such as fibres, counteracts the matrix' disposition to catastrophic failure. This differs from the general perception of composites where the fibres are thought to carry most of the applied load. The latter applies to composites with polymers and metals as the matrix phase [15].

In fibre-reinforced composites, the material consists of a matrix and a fibrous dispersed phase. Most composites are reinforced with fibres as materials tend

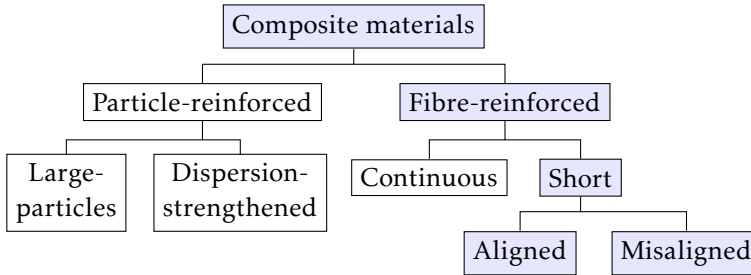


Figure 2.1: General categorization of composites.

to be stronger and stiffer as fibres compared to other forms [15]. The orientations of fibres may vary as illustrated in Figure 2.2. The figure on the left shows fibres uniformly aligned in one direction. A uniform distribution of fibres is often desired in order to achieve ideal anisotropic material properties. This is often not possible due to the nature of commonly used fabrication processes such as injection molding presented in Section 2.2.3. Fibre-reinforced composites are further classified based on the length of the fibres. Long *continuous* fibres make up one sub-classification. Continuous fibres are normally aligned and make the reinforcement more effective. The theme for this thesis, is composites with short fibres in its dispersed phase. Although short (discontinuous) fibres are not as effective as reinforcements, short fibre-reinforced composites can be made to have elastic stiffness moduli and tensile strengths up to 90% of their continuous fibre analogue [14].

Callister and Rethwisch [14] states that there exists a critical fiber length l_c which is necessary for effectively transferring the applied load between the matrix and fibre phases. Equation 2.1 defines l_c as a function of the ultimate tensile strength σ_f^{UTS} and the diameter d of the fibre, and the phase-interface bond strength (or the shear yield stress of the matrix - whichever has the smallest value) τ_c .

$$l_c = \frac{\sigma_f^{UTS} d}{2\tau_c} \quad (2.1)$$

Fibres with length $l \ll l_c$ are termed discontinuous or short. The limit that separates discontinuous from continuous fibres is normally set to $l = 15l_c$ [14].

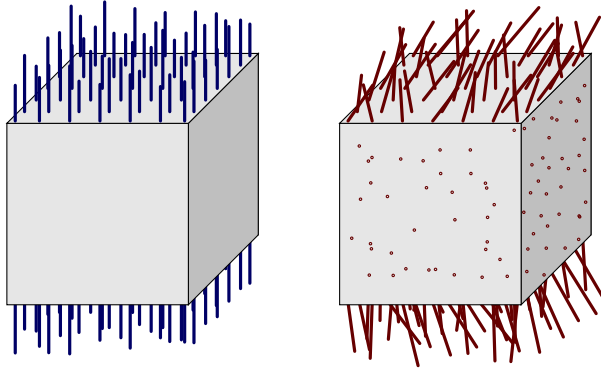


Figure 2.2: Aligned and misaligned fibres inside a matrix material.

Fabrication processes such as injection molding tend to produce composites with short fibres shorter than l_c with an unfavorable fibre orientations [16].

2.2.2.1 Short fibre reinforced composites

The use of short fibre-reinforced composites (SFRC) in load bearing structures is becoming increasingly attractive in industrial application due to their many favorable attributes such as inexpensive fabrication and formability. However, the formability of SFRCs comes at a cost in terms of efficiency of the reinforcing fibres. As mentioned above, common fabrication techniques produces short fibres with lower reinforcing efficiency. The lower efficiency is partly due to the reduced ability to transfer load from the matrix to the fibres, but also the non-optimal orientations of the fibres [14, 17, 16, 18]. The SFRCs mechanical properties are also seen to be functions of the fibre content [16, 19, 11].

The reader is referred to [15, 14] for further reading on the subject of general composites.

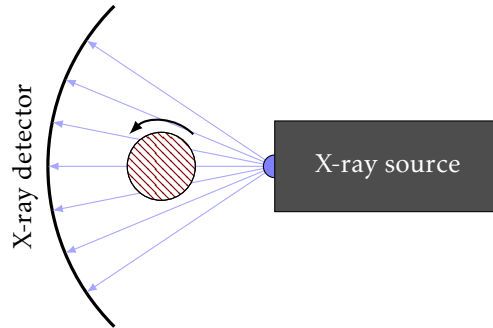


Figure 2.3: A simple illustration of the principle of X-ray computed tomography.

2.2.3 Injection molding

Injection molding is the most widely used fabrication process for thermoplastic materials. The technique allows for short cycle times and the creation of components with complex geometries at low unit cost.

The process uses pelletized material which is fed through a feed hopper into a cylinder. In the cylinder, the material is pushed into a heated chamber by a hydraulic plunger or ram. The material is forced around a spreader in order to make contact with the heated walls of the chamber, and melts to form a viscous liquid. The molten material exits the heated chamber by extrusion through a nozzle and into a mould cavity where it cools and solidifies. The direction of which the molten material is injected is referred to as the *injection flow direction*. The process is explained with illustrations in [14].

2.3 X-ray computed tomography

X-ray computed tomography (i.e. X-ray CT) refers to the concept of reconstructing a three-dimensional image of an object based on a series of X-ray images sampled at different angles.

Figure 2.3 gives a simple illustration of the concept. An object is placed be-

tween a X-ray source and an X-ray detector. The source radiates the object with X-rays, which is partly absorbed by the object. The amount of X-rays absorbed is a function of the different densities present in the object. The detector detects the X-rays which passes through the object and produces an image of the internal structure. The object is slightly rotated by a given rotation and a new image is then produced. This procedure is repeated until a full mapping of the object is achieved. The set of X-ray images is then reconstructed into a three-dimensional visualisation.

For more information on subject of X-ray CT, the reader is referred to [20].

2.4 Materials mechanics

2.4.1 Large deformations

As the rotations and deformations of a continuum extends beyond the validity of the theory of small deformation, a more extensive theory is needed. This section presents the large deformation theory relevant for this thesis.

2.4.1.1 The deformation gradient

When describing large deformations of a continuum, it is important to differentiate between the *reference* (undeformed) and the *current* (deformed) configuration. Any material points in the reference and current configurations are given by the vectors \mathbf{X} and \mathbf{x} , respectively. These vectors are defined in a Cartesian coordinate system through the Equations 2.2 and 2.3.

$$\mathbf{X} = X_i e_i \quad (2.2)$$

$$\mathbf{x} = x_i e_i \quad (2.3)$$

e_i ($i = 1, 2, 3$) are the basis vectors for the Cartesian coordinate system. This is illustrated in Figure 2.4. Assuming that there exists a function $\zeta(\mathbf{X}, t)$ which maps the motion of the continuum, so that

$$\mathbf{x} = \zeta(\mathbf{X}, t). \quad (2.4)$$

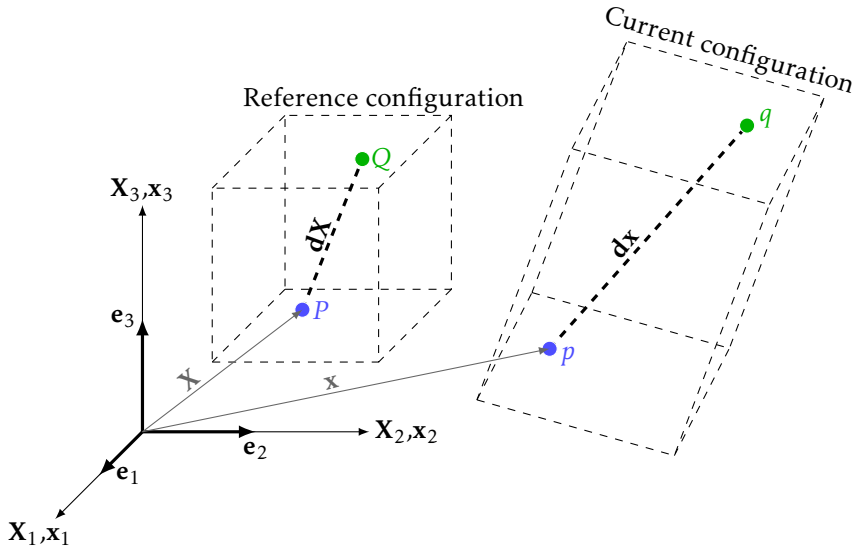


Figure 2.4: The reference and current configuration of a continuum.

ζ is assumed to be continuously differentiable with respect to \mathbf{X} . The deformation gradient $\mathbf{F}(\mathbf{X}, t)$ is then defined as

$$\nabla\zeta = \mathbf{F}(\mathbf{X}, t) = \frac{\partial\zeta}{\partial\mathbf{X}} = \frac{\partial\mathbf{x}}{\partial\mathbf{X}} \quad \text{or} \quad F_{ij} = \frac{dx_i}{dX_j} = \frac{d\zeta_i}{dX_j}. \quad (2.5)$$

An infinitesimal line segment $d\mathbf{X}$ is spanned between two material point, P and Q , in the continuum in the reference configuration. The mapping of these two points in the current configuration is denoted p and q and the corresponding infinitesimal line segment between is $d\mathbf{x}$. Thus, the relation between the two line segments in the reference and current configuration of the continuum are given by

$$d\mathbf{x} = \mathbf{F}d\mathbf{X} \quad \text{or} \quad dx_i = F_{ij}dX_j. \quad (2.6)$$

The theory presented in this section was collected from [13, 21, 22, 23]

2.4.1.2 Stretch ratio

The stretch ratio λ is a measure of the extensional strain of a differential line segment. It is defined as the ratio between the lengths of a differential line segment in its current and reference configuration, respectively. The stretch ratio is explicitly stated in Equation 2.7 where l_{cur} is the length in the current configuration while l_{ref} is the length in the reference configuration.

$$\lambda = \frac{l_{cur}}{l_{ref}} \quad (2.7)$$

Seen in context with what stated in Section 2.4.1.1, λ can be expressed as

$$\lambda = \frac{\|d\mathbf{x}\|}{\|d\mathbf{X}\|} = \sqrt{\mathbf{N}^T \cdot \mathbf{F}^T \cdot \mathbf{F} \cdot \mathbf{N}}. \quad (2.8)$$

where $\|d\mathbf{x}\|$ and $\|d\mathbf{X}\|$ denotes the euclidean norm of $d\mathbf{x}$ and $d\mathbf{X}$, respectively. \mathbf{N} is the directional vector of the line segment $d\mathbf{X}$. The reader is referred to [21] for a more in-depth review on this subject.

2.4.1.3 Corotational reference frame

The deformation of a continuum may be separated into rigid-body motion and straining. Rigid-body motion can be subdivided into rotations and translations. A corotated reference frame translate and rotates with the continuum as the global coordinate system remains fixed. This is illustrated in Figure 2.5. It often necessary to formulate certain theories in a corotated framework, rather than in the global coordinate system. For further reading, the reader is referred to [21, 24].

2.4.1.4 True strain

The relationship between the stretch ratio λ and the true strain ε , is given by Equation 2.9.

$$\varepsilon = \int_{l_{ref}}^{l_{cur}} \frac{dl}{l} = \ln\left(\frac{l_{cur}}{l_{ref}}\right) = \ln(\lambda) \quad (2.9)$$

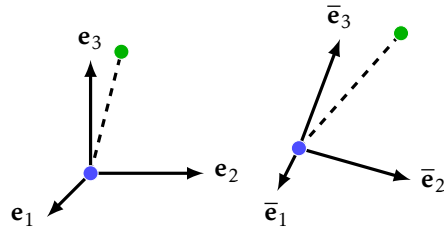


Figure 2.5: Illustration of a fixed global coordinate system to the left and a corotated reference frame to the right.

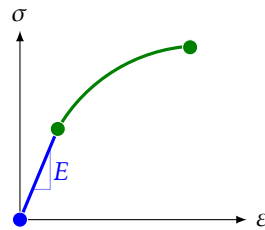


Figure 2.6: The blue and green portions of the graph illustrate linear elastic and plastic material response, respectively.

2.4.2 Constitutive relation

A constitutive relation is the relation which relates two physical quantities. In this thesis, constitutive relations are used to relate stresses and strains. Figure 2.6 illustrates the relationships between stress and strain for the concepts presented in the following sections.

2.4.2.1 Linear elasticity

If the relationship between the stresses and strains are linear and the deformation is reversible, the material behavior is said to be linear elastic. Linear elastic material behavior can be expressed through Hooke's law. Hooke's law is stated for a complex stress state in Equation 2.10.

$$\sigma_{ij} = \frac{E}{(1 + \nu_e)} \left[\varepsilon_{ij} + \frac{\nu_e}{(1 - 2\nu_e)} \delta_{ij} \varepsilon_{kk} \right] \quad (2.10)$$

E and ν_e are the material-specific Young's modulus and elastic Poisson's ratio. For a one-dimensional stress state, Equation 2.10 reduces to Equation 2.11.

$$\sigma_{11} = E\varepsilon_{11} \quad \Rightarrow \quad \sigma = E\varepsilon \quad (2.11)$$

The blue line in Figure 2.6 illustrates this one dimensional stress state.

2.4.2.2 Plasticity

The theory of plasticity defines the mechanical response in a solid as it deforms beyond the validity of theory of elasticity. The response is highly material dependent and the plastic material modelling is therefore based on experimental observations. However, there are three main concepts that are used to describe plastic material behavior; the yield criterion, the flow rule and the work-hardening rule. In this section the definition of these concepts and their individual roles in describing plasticity will be explained.

As a solid is subjected to force it deforms. If the deformation is permanent when the force is removed, the solid is said to have undergone irreversible plastic deformation. This deformation occurs after the stress state passes a critical value known as the *yield limit* and mathematically this limit is defined through a *yield criterion*. The yield criterion is expressed as Equation 2.12.

$$f(\sigma) = 0 \quad (2.12)$$

The yield criterion consists of a *yield function* f that is a continuous function of the stress state σ . The yield criterion in Equation 2.12 can be geometrically interpreted as a surface in the vector space defined by the components of σ . This surface is referred to as the *yield surface*. As the stress state is below the critical yield limit, and therefore on the inside of the yield surface, the deformation is elastic and $f(\sigma) < 0$. It is worth mentioning that $f(\sigma) > 0$ is not acceptable. An illustration of the yield surface is given in Figure 2.7.

The formulation of the yield function f depends on the chosen yield criterion. The choice of a suitable yield criterion is dependent on the material in use, and is often based on experience and experiments. For materials such

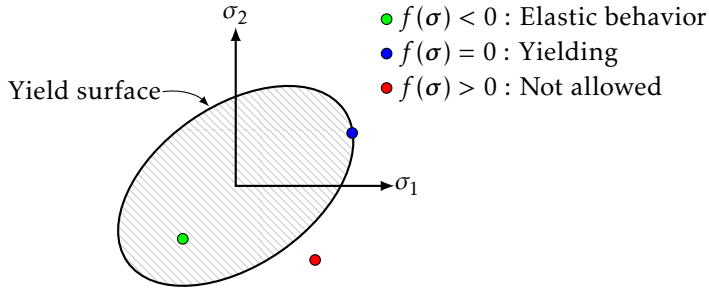


Figure 2.7: Geometric interpretation of the von Mises yield surface in two dimensions. σ_1 and σ_2 are the principal stress components.

as metals and alloys, the yield criterion is often assumed to only be dependent on the deviatoric stress state, σ' . These materials are said to be *pressure insensitive* and the yield function take the form of Equation 2.13.

$$f(\sigma') = 0 \quad (2.13)$$

Other materials such as soils, concretes and some polymers, may be assumed to be *pressure sensitive*. The yield function for these materials may be defined as a function of both σ' and the hydrostatic stress, σ_H , and written as in Equation 2.14

$$f(\sigma', \sigma_H) = 0 \quad (2.14)$$

A convenient way of writing the yield function is through Equation 2.15 in terms of *effective stress*, σ_e , and *flow stress*, σ_y . The different yield criteria differs in the way the yield function is defined. Table 2.1 gives some examples of common yield criteria.

$$f(\sigma) = \sigma_e(\sigma) - \sigma_y \quad (2.15)$$

Most materials experience some sort of evolution of their yield surfaces during plastic deformation. There are two main notions when it comes to material hardening; isotropic hardening and kinematic hardening. Equation 2.16 presents a general yield function with material hardening where p is the *equivalent plastic strain* and χ is known as the back stress that represents a transla-

Table 2.1: Common yield criteria.

Name	Yield function
Von mises / J_2	$\sqrt{\frac{3}{2}\sigma'_{ij}\sigma'_{ij}} - \sigma_Y$
Tresca	$\max(\sigma_1 - \sigma_2 , \sigma_2 - \sigma_3 , \sigma_3 - \sigma_1) - \sigma_Y$
Drucker-Prager	$\frac{\sqrt{\frac{3}{2}\sigma'_{ij}\sigma'_{ij} + \alpha\frac{1}{3}\sigma_H}}{1+\alpha} - \sigma_Y$

tion of the yield surface.

$$f(\boldsymbol{\sigma}, p) = \sigma_e(\boldsymbol{\sigma} - \boldsymbol{\chi}(p)) - \sigma_y(p) \quad (2.16)$$

Equation 2.17 mathematically defines the cases of hardening. Perfect plasticity represents no evolution of the yield surface, while the two other cases are illustrated in Figure 2.8.

$$\begin{aligned} \chi(p) = 0, \frac{\partial \sigma_y(p)}{\partial p} = 0 &\Rightarrow \text{perfect plasticity} \\ \chi(p) = 0, \frac{\partial \sigma_y(p)}{\partial p} > 0 &\Rightarrow \text{isotropic hardening} \\ \chi(p) \neq 0, \frac{\partial \sigma_y(p)}{\partial p} = 0 &\Rightarrow \text{kinematic hardening} \end{aligned} \quad (2.17)$$

The green line of Figure 2.6 illustrates the isotropic hardening of a material subjected to a one-dimensional stress state.

Equation 2.18 presents the decomposition of the total strain increment, $d\boldsymbol{\varepsilon}$, into an elastic contribution and a plastic contribution.

$$d\boldsymbol{\varepsilon} = d\boldsymbol{\varepsilon}^e + d\boldsymbol{\varepsilon}^p \quad (2.18)$$

A flow rule is used to determine the plastic strain increment tensor $d\boldsymbol{\varepsilon}^p$ based on the stress tensor, $\boldsymbol{\sigma}$. It must be chosen in a way that ensures positive dissipation as plastic strains develop.

$$d\boldsymbol{\varepsilon}^p = d\lambda \frac{\partial g(\boldsymbol{\sigma})}{\partial \boldsymbol{\sigma}} \quad (2.19)$$

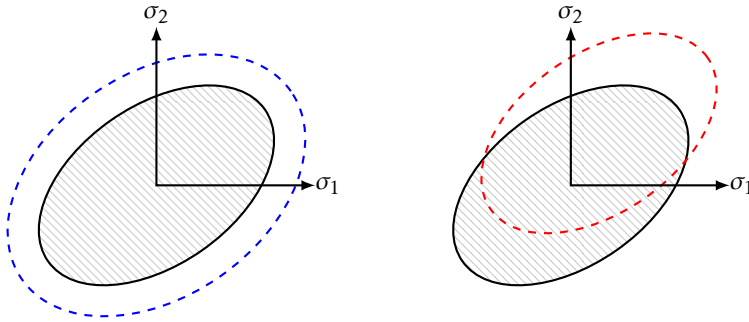


Figure 2.8: Evolution of a Von Mises yield surface due to work-hardening. The left figure illustrates the concept of isotropic hardening and the right figure illustrates kinematic hardening.

A general expression for the flow rule is presented Equation 2.19 where $d\lambda$ and $g(\sigma)$ are known as the plastic multiplier and plastic potential function, respectively. The stated flow rule is known as a *non-associated* flow rule. If the plastic potential function is chosen as the yield function f , the resulting flow rule is defined as *associated*.

For a detailed presentation of the presented concepts, the reader is referred to [25, 13, 12].

2.4.3 Transformation of stress

Transforming the stress tensor from one coordinate basis systems to another, can be done through Equation 2.20.

$$\bar{\sigma} = \mathbf{Q} \cdot \sigma \cdot \mathbf{Q}^T \quad (2.20)$$

See section 2.5.3 for the definition of the transformation matrix \mathbf{Q} . For a further review on the subject of stress transformation, the reader is referred to [26].

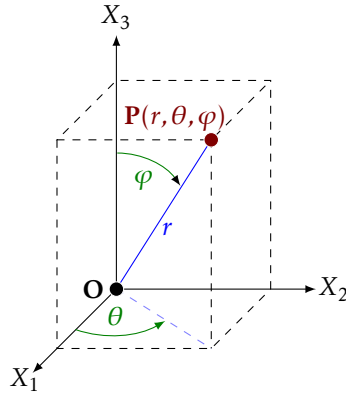


Figure 2.9: Convention for the spherical coordinate system.

2.5 Euclidean space

In order to develop the mathematical basis for the model, one must represent points in geometric space. The systems and techniques used to represent euclidean space are therefore defined in this section.

For further reading on the subjects of presented in Section 2.5.1 and 2.5.2, the reader is referred to [27].

2.5.1 Spherical coordinate system

The convention used for the spherical coordinate system is illustrated in Figure 2.9.

- The radial distance r is the euclidean distance between the origin O and the point P .
- The azimuthal angle θ is defined as the angle between the first axis in the reference Cartesian coordinate system, X_1 , and the projection of the line segment OP onto the reference plane spanned by X_1 and X_2 . Positive values for θ is given for positive rotations about the reference system's third axis X_3 as seen in Figure 2.9.

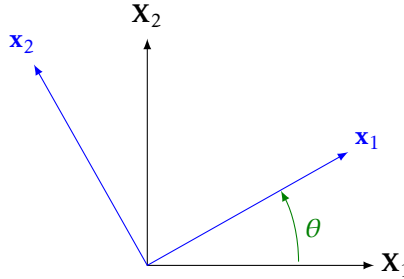


Figure 2.10: Rotation of coordinate basis in two dimensions.

- The inclination angle φ is defined as the angle between the reference system's third axis and the line segment OP.

2.5.2 Coordinate system conversion

The formulas for conversion between Cartesian and spherical coordinates are given in Equation 2.21.

$$\begin{aligned} X_1 &= r \sin(\varphi) \cos(\theta) \\ X_2 &= r \sin(\varphi) \sin(\theta) \\ X_3 &= r \cos(\varphi) \end{aligned} \quad (2.21)$$

2.5.3 Coordinate transformations

When describing an object in several bases it is important to establish the necessary operators. Figure 2.10 illustrates a basis which have been rotated with respect to a reference system. The relation between the reference system, \mathbf{X} , and the rotated basis, \mathbf{x} is given as

$$\mathbf{X} = \mathbf{R} \cdot \mathbf{x} \quad (2.22)$$

where \mathbf{R} is the *rotation matrix*. As \mathbf{R} is orthogonal, $\mathbf{R}^{-1} = \mathbf{R}^T$ i.e. $\mathbf{R}^T \mathbf{R} = \mathbf{I}$. \mathbf{R}^T is denoted \mathbf{Q} and referred to as the *transformation matrix*, giving rise to

$$\mathbf{x} = \mathbf{Q} \cdot \mathbf{X} \quad (2.23)$$

Transformation matrix, Q:

The coordinate system rotates while the object remains fixed.

Rotation matrix, R:

The object rotates while the coordinate system remains fixed.

As an example, the rotation matrix for the case in Figure 2.10 is

$$\mathbf{R} = \begin{bmatrix} \cos(\theta) & -\sin(\theta) \\ \sin(\theta) & \cos(\theta) \end{bmatrix}. \quad (2.24)$$

A general expression for the transformation matrix can be formulated for three dimensions as done in Equation 2.25.

$$\mathbf{Q} = \begin{bmatrix} x_1^1 & x_1^2 & x_1^3 \\ x_2^1 & x_2^2 & x_2^3 \\ x_3^1 & x_3^2 & x_3^3 \end{bmatrix} \quad (2.25)$$

where x_i^j is the j component of the i basis vector for the rotated coordinate system in the reference coordinate system.

For a more thorough presentation of the theory in Section 2.5.3, the reader is referred to [28] and [26].

2.6 Statistical theory

This section presents the concepts of the statistical theories that are relevant for this thesis. Normal distributions have been used to represent the random variation in fibre properties such as the orientation of fibres in dispersed in the matrix material, but the concepts also apply to other statistical distributions.

2.6.1 Normal distribution

The normal distribution goes under many names; Bell curve, Gaussian distribution, Gaussian bell curve, etc. The normal distribution is a continuous probability distribution which is used to model the random variation of stochastic variables.

2.6.1.1 Univariate

The *univariate* normal distribution is the simplest form of normal distribution. It represents the random variation of *one single* stochastic variable. The normal *probability density function* f is presented in Equation 2.26.

$$f(x, \mu, \sigma) = \frac{1}{\sqrt{2\pi}\sigma} e^{-\frac{1}{2}\left(\frac{x-\mu}{\sigma}\right)^2} \quad (2.26)$$

The standard deviation σ is the square root of variance of x which is the stochastic variable of the univariate distribution and μ is the expected value of x . The definition of the *cumulative distribution function* P is defined in 2.27.

$$P(-\infty \leq X \leq a) = P(X \leq a) = \int_{-\infty}^a f(x, \mu, \sigma) dx \quad (2.27)$$

$P(X \leq a)$ represents the probability of X taking a value of $\leq a$. The cumulative distribution function for the normal distribution becomes

$$P(X \leq a) = \frac{1}{2} \left[1 + \frac{1}{\sqrt{\pi}} \int_{-\frac{a-\mu}{\sigma}}^{\frac{a-\mu}{\sigma}} e^{-\frac{1}{2}\left(\frac{x-\mu}{\sigma}\right)^2} dx \right]. \quad (2.28)$$

2.6.1.2 Multivariate

A system is often dependent on more than one stochastic variable. The variables may then be modeled with a multivariate distribution. The multivariate normal distribution is a generalisation of the univariate normal distribution and represents the random distribution of a set of stochastic variables. The single distributed variable of the univariate distribution becomes a k -dimensional vector of distributed values $\mathbf{x} = \{X_1, X_2, \dots, X_k\}$. The probability density function for the multivariate normal distribution is presented in Equation 2.29.

$$f(\mathbf{x}, \boldsymbol{\mu}, \boldsymbol{\Sigma}) = \frac{1}{\sqrt{(2\pi)^k |\boldsymbol{\Sigma}|}} e^{-\frac{1}{2}(\mathbf{x}-\boldsymbol{\mu})^T \boldsymbol{\Sigma}^{-1} (\mathbf{x}-\boldsymbol{\mu})} \quad (2.29)$$

where $\boldsymbol{\Sigma}$ is the covariance matrix with dimension $k \times k$ and entries $\Sigma_{ij} = \text{cov}(X_i, X_j)$, and the expected value vector $\boldsymbol{\mu} = \{E(X_1), E(X_2), \dots, E(X_k)\}$. Figure 2.11 illustrates a multivariate normal distribution of X_1 and X_2 where $\boldsymbol{\Sigma}$ has non-zero off-diagonal entries.

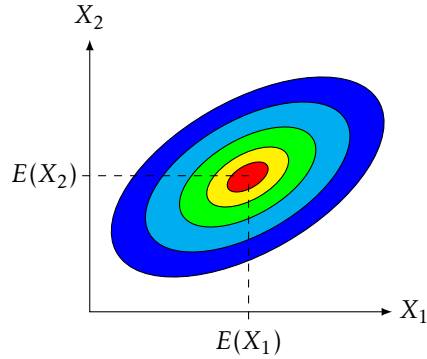


Figure 2.11: Illustration of the contours from a multivariate (bivariate) distributed normal density function.

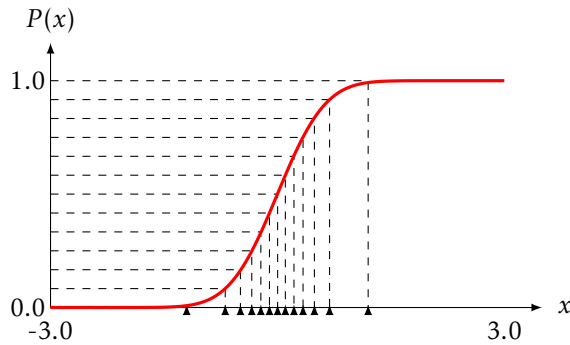


Figure 2.12: Cumulative probability function for a univariate normal distribution with $\sigma^2 = 0.5$ and $\mu = 0$.

2.6.2 Monte Carlo cycles

In Monte Carlo analysis, values are generated from a given probability distribution. It is used to model complex systems which depend on one or more stochastic variables where the resulting distribution of the system is not easily obtained. In the SFRM-model, Monte Carlo iterations are used to generate distributed fibre orientations.

A method of generating random variables according to a given probability distribution is to first generate values in the range $[0, 1]$ for a uniformly distributed variable U , find the inverse of the cumulative distribution function, P^{-1} , and then finally calculate $P^{-1}(U)$. Figure 2.12 illustrates the idea of using the inverse of P as a function of uniformly distributed U to generate a value sampled from a certain probability distribution. Unfortunately, a difficulty arises as the inverse of the normal cumulative probability function does not have a closed-form expression. Box and Muller [29] presents a method for overcoming this obstacle, called the Box Muller transform.

2.6.2.1 Box Muller

The procedure which Box and Muller [29] presents, generates a pair of values sampled from the same normal distribution, X_1 and X_2 , from a pair of uniformly distributed values U_1 and U_2 . U_1 and U_2 are both in the range of $[0, 1]$. The relationship between the two pairs, is presented in Equation 2.30.

$$\begin{aligned} X_1 &= \sqrt{-2\ln(U_1)} \cos(2\pi U_2) \\ X_2 &= \sqrt{-2\ln(U_1)} \sin(2\pi U_2) \end{aligned} \quad (2.30)$$

The details concerning the derivation of Equation 2.30 is presented in [29]

2.7 Abaqus interface

2.7.1 Subroutine interfaces

As an option to customise the software, Abaqus provides a set of interfaces in the form of programmable subroutines. Through these *user subroutines*, the user can control and modify analysis features such as specifying prescribed boundary conditions, element formulation, mechanical constitutive behaviour of materials, etc. The subroutines that specify the mechanical constitutive behaviour of materials are named UMAT and VUMAT for Abaqus/Implicit and Abaqus/Explicit, respectively. According the Abaqus Documentation [30], Abaqus FEA supports user subroutines implemented in the programming languages FORTRAN and C/C++. The SFRM-model is implemented in FORTRAN for Abaqus/Explicit (i.e. subroutine VUMAT). Figure

2.13 gives a simple overview of an analysis in Abaqus/Explicit and where the constitutive material modelling (via VUMAT) is required.

2.7.2 The Abaqus Scripting Interface

Abaqus FEA also provides another useful interface; The Abaqus Scripting Interface. This is an application programming interface (API) developed as a customised extension of the Python programming language. It gives the user access to many functionalities such as modelling of components, submitting of analysis to the solvers and quick extraction of analysis results. The use of this feature may not be reflected explicitly in this thesis report, but it has served as a valuable tool in the development of the SFRM-model.

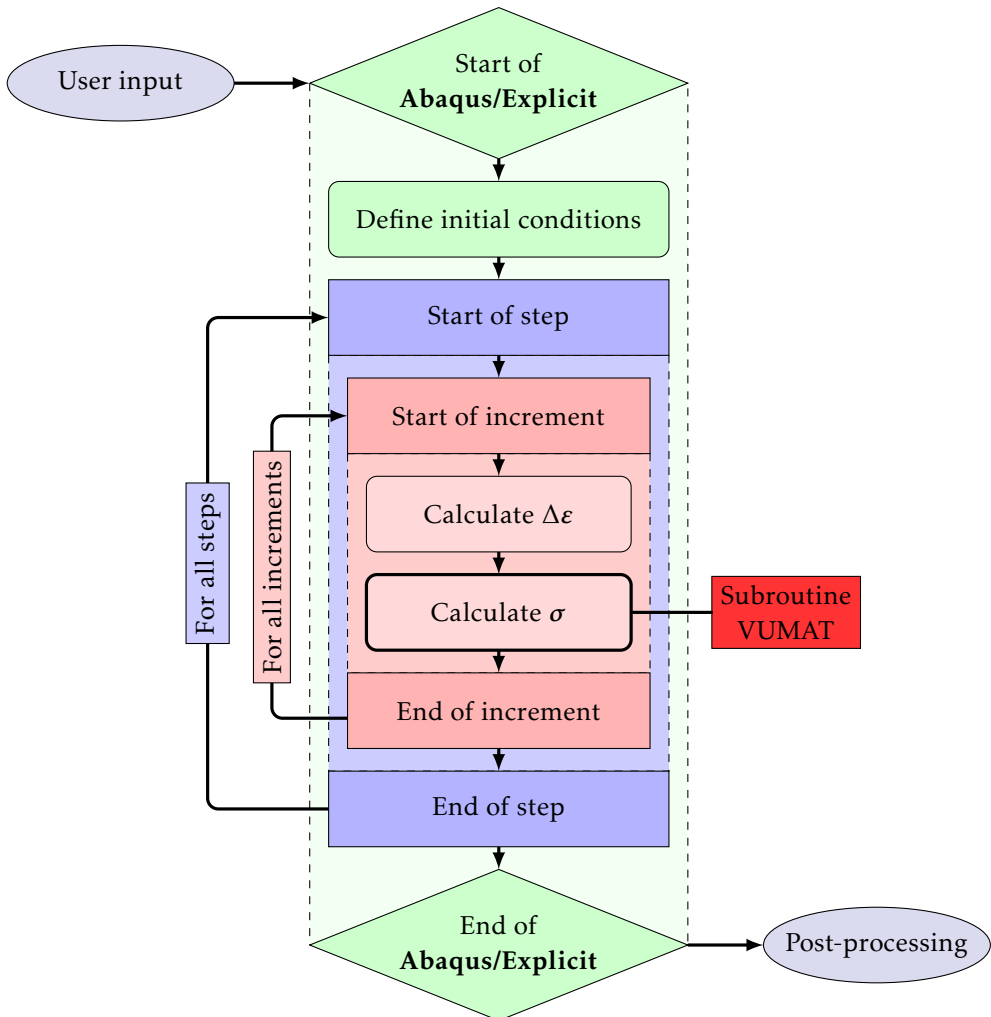


Figure 2.13: Overview of an analysis in Abaqus/Explicit. The colour codes give an indication of the levels within the analysis.

Chapter 3

Short Fibre-Reinforced Materials - model

In this chapter, the Short Fibre-Reinforced Materials-model (SFRM-model) is presented. The overall framework of the model will first be explained in order to give the reader a conceptual idea along with the mathematical definition of features related to the model. Following this, a condensed pseudo formulation of the model will be presented where some of the equations are restated. Finally, aspects concerning the software implementation in FORTRAN will be discussed.

The SFRM-model is similar to what was presented in [7], but with some exceptions. The model in [7] will later be used as a means to verify the implementation of the SFRM-model.

3.1 Framework

In the SFRM-model, the fibre reinforced material is thought to consist of two phases; a matrix phase and a fibre phase. In the model, the two phases are managed somewhat separately. The two phases are decomposed, the stress tensor for each phase is calculated and the contributions are then superimposed to a tangible stress tensor for the material as a whole. The matrix material model can be modeled with an arbitrary constitutive relation that the user finds suitable. The focus of this thesis has not been the implementation of matrix constitutive relation, but the development of the foundation for the dispersed fibre phase.

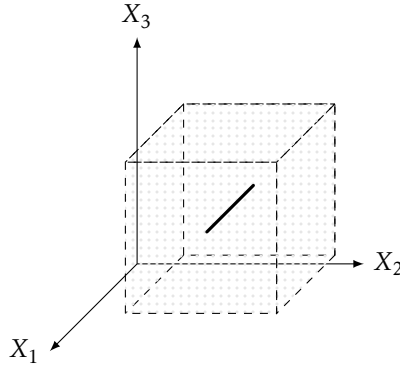


Figure 3.1: Single fibre in a surrounding matrix phase.

For a given short fibre reinforced material, a given number of fibres are dispersed in the continuous matrix phase, but for the following three sections, the reader should picture a single fibre surrounded by a continuous matrix like the illustration in Figure 3.1. Both fibre and matrix take up a given fraction of the volume, v_f and v_m . The fibre has a given orientation characterised by a unit vector \mathbf{N}_f in a reference coordinate system \mathbf{X} . The model assumes an iso-strain state for the fibre and matrix phase. The single-fibre-explanation will later be expanded to include multiple fibres in a continuous matrix with variation in orientation.

3.1.1 Matrix phase

As mentioned above, the constitutive material behavior of the matrix is not the main focus of this thesis. The matrix can, for example, be modelled with an arbitrary elastic-plastic material behavior as described in Section 2.4.2.2. The matrix model which was used during the development of the SFRM-model is presented in Section 3.4.

The matrix phase is subjected to a strain increment, calculated at each increment in the explicit analysis, and the constitutive material relation gives a stress state as the Cauchy stress tensor σ_m expressed in the global reference

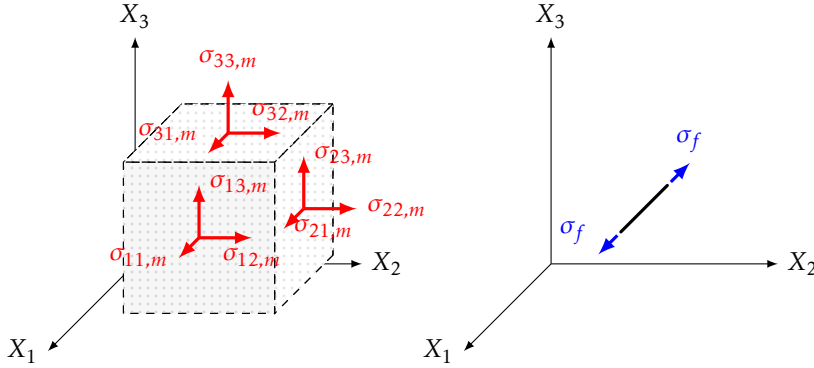


Figure 3.2: Stress state in the two phases.

system **X**. The illustration on the left in Figure 3.2 illustrates the stress state in the matrix phase.

$$\boldsymbol{\sigma}_m = \begin{bmatrix} \sigma_{11,m} & \sigma_{12,m} & \sigma_{13,m} \\ \sigma_{21,m} & \sigma_{22,m} & \sigma_{23,m} \\ \sigma_{31,m} & \sigma_{32,m} & \sigma_{33,m} \end{bmatrix}$$

3.1.2 Fibre phase

The constitutive material response of the fibre, is modelled as linear elastic with a given stiffness modulus, E_f . The fibre is assumed to only deform in its longitudinal direction. At each increment in the explicit analysis, a deformation gradient \mathbf{F} is calculated and passed to the VUMAT. The list that follows outlines the procedure that calculates the fibre stress σ_f in the direction of the fibre orientation (\mathbf{N}_f) as illustrated in Figure 3.2.

1. The stretch λ_f that occurs in the fibre is calculated from \mathbf{F} and the fibre orientation \mathbf{N}_f from Equation 2.8.
2. λ_f is converted to true strain ε_f with Equation 2.9.
3. The fibre stress σ_f is calculated with Equation 2.11 using ε_f and E_f .

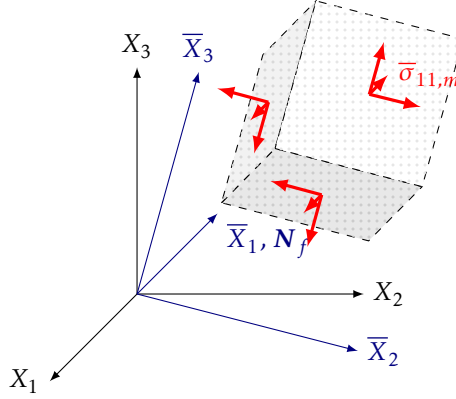


Figure 3.3: Orthonormal basis $\bar{\mathbf{X}}$ with \bar{X}_1 -axis parallel to \mathbf{N}_f and the illustration of the stress tensor $\bar{\sigma}_m$.

4. An orthonormal basis $\bar{\mathbf{X}}$ in \mathbb{R}^3 with \mathbf{N}_f as the first axis, is established.

3.1.3 Combining of phases

After the σ_m and σ_f have been calculated, the contributions need to be combined into a final stress tensor. The procedure for combining the contributions is summarised as

1. Transform σ_m into $\bar{\mathbf{X}}$ using the theory presented in Section 2.4.3, and denote the resulting stress tensor $\bar{\sigma}_m$. $\bar{\sigma}_m$ and $\bar{\mathbf{X}}$ are illustrated in Figure 3.3.
2. Replace $\bar{\sigma}_{11,m}$ with σ_f . The resulting stress tensor is denoted $\bar{\sigma}_f$.
3. Transform $\bar{\sigma}_f$ into \mathbf{X} , and denote it the fibre stress tensor σ_f .
4. The contributions are then superimposed in a rule-of-mixture stated in Equation 3.1.

$$\boldsymbol{\sigma} = \sigma_f v_f + \sigma_m v_m \quad (3.1)$$

The volume fraction of the fibre $v_f \in [0, 1]$ gives the volume fraction of the matrix as $v_m = 1 - v_f$.

3.1.4 Discretisation of fibre orientation

In the previous sections, the model framework was presented using a single fibre surrounded by a matrix phase. This single-fibre-representation of the total dispersed fibre phase volume fraction v_f would be sufficient to represent all fibre contributions to Equation 3.1 if all fibres had the same orientation (i.e. aligned). The following presents a means of representing fibre contribution in a short fibre reinforced material where fibres are misaligned.

3.1.4.1 Grouping and weighting of similar fibres

Fibres with similar orientation are assorted in group i and represented by orientation vector \mathbf{N}_f^i . The number of fibres in i make up the fraction W_f^i out of the total number of fibres. If there are a total of k groups of fibres, then

$$\sum_{i=1}^k W_f^i = 1$$

W_f^i can be viewed as a weight of the group i . The fibre stress tensor that is calculated for group i , according to the procedure for the fiber phase, is σ_f^i . The total fibre stress tensor for the weighted and summed contribution for all groups, becomes

$$\sigma_f = \sum_{i=1}^k \sigma_f^i W_f^i$$

The rule-of-mixture in Equation 3.1 can now be expanded to include a fibre phase with multiple fibre orientations as in Equation 3.2.

$$\sigma = \left(\sum_{i=1}^k \sigma_f^i W_f^i \right) v_f + \sigma_m v_m \quad (3.2)$$

The amount of fibres that is associated with each group may be modelled with a given distribution such as the an uniform- or normal distribution. After the orientations have been discretised into groups, the density function for the specific distribution may then be used to weight the groups according to Equation 3.3.

$$W_f^i = \frac{f(\theta^i, \varphi^i)}{\sum_{n=1}^m f(\theta^n, \varphi^n)} \quad (3.3)$$

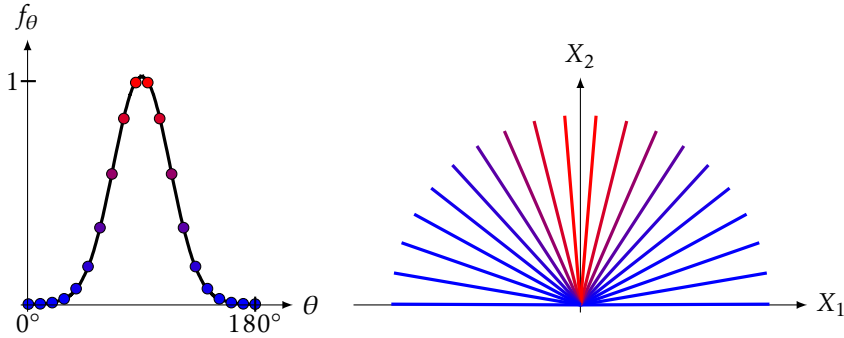


Figure 3.4: Fibre discretisation and weighting where $\theta \sim \mathcal{N}(\mu = 90^\circ, \sigma = 22.5^\circ)$.

An example: In-plane fibre distribution

Picture a fibre phase where all fibres lie in the X_1X_2 -plane (i.e. $\varphi = 90^\circ$). The variation in orientation in the X_1X_2 -plane is given as a Normal distributed θ with expected value $\mu = 90^\circ$ and standard deviation $\sigma = 22.5^\circ$. Figure 3.4 illustrates a discretisation of 20 groups for the given distribution of θ . The unit vector \mathbf{N}_f^i for each group is described by $(\theta, \varphi) = (\theta_i, 90^\circ)$ in spherical coordinates. The figure to the left illustrates the density function of the distribution and each marker is a group with a corresponding density value, $f_\theta(\theta^i)$. The figure to the right illustrates \mathbf{N}_f^i with color variation based on each group's weight W_f^i . Red to blue color variation illustrates a decreasing weight.

3.1.4.2 Representing fiber orientation

In the SFRM-model, the orientation of each group i is uniquely described by its unit vector \mathbf{N}_f^i which is given by the spherical angles θ^i and φ^i . The domain which is needed for any of the two angles to give a unique orientation, is $[0^\circ, 180^\circ)$. For example, $\theta^i = 230^\circ (= \overline{\theta^i})$ would be the equivalent of $\theta^i = 50^\circ$ like illustrated in Figure 3.5. A generalised scheme for sorting angular values

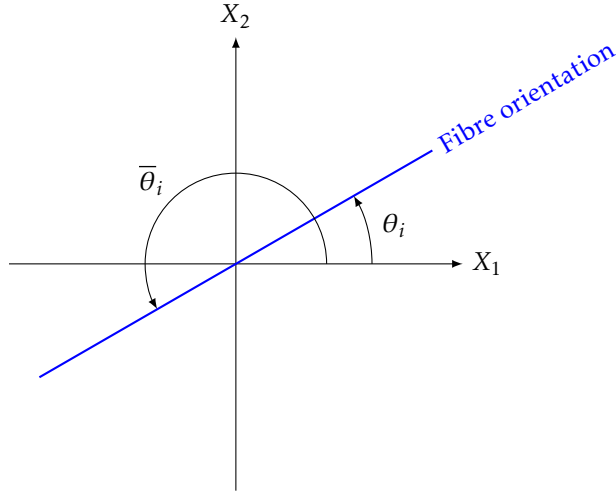


Figure 3.5: Illustration of θ_i and $\bar{\theta}_i$.

into the given domain needs to be established as the user may wish to input a distribution which has large portions of its population below 0° or above 180° . If $\bar{\theta}^i$ and $\bar{\varphi}^i$ defines the angular discretisation of user specified domain, then θ^i and φ^i defines the equivalent values within $[0^\circ, 180^\circ)$. Equation 3.4 establishes $\bar{\theta}^i$ and $\bar{\varphi}^i$.

$$\begin{aligned}\bar{\theta}^i &= \bar{\theta}_{min}^{domain} + \frac{\bar{\theta}_{max}^{domain} - \bar{\theta}_{min}^{domain}}{(k_\theta - 1)}(i - 1) \\ \bar{\varphi}^i &= \bar{\varphi}_{min}^{domain} + \frac{\bar{\varphi}_{max}^{domain} - \bar{\varphi}_{min}^{domain}}{(k_\varphi - 1)}(i - 1)\end{aligned}\quad (3.4)$$

k_θ and k_φ are the requested number of discretisation points for each spherical angle. For $\bar{\theta}$, $\bar{\theta}_{max}^{domain}$ and $\bar{\theta}_{min}^{domain}$ are the upper- and lower bounds of the user domain, respectively. For a fibre phase distributed according to a Normal distribution with a standard deviation σ and expected value μ , the upper- and lower bounds can be defined through $(\mu + a \cdot \sigma)$ and $(\mu - a \cdot \sigma)$. $a = 3$ will

cover 99.8% of the occurrences. Equation 3.5 handles the mapping of the user defined domain into $[0^\circ, 180^\circ)$.

$$\begin{aligned}\theta^i &= \bar{\theta}^i - 180^\circ \left\lfloor \frac{\bar{\theta}^i}{180^\circ} \right\rfloor \\ \varphi^i &= \bar{\varphi}^i - 180^\circ \left\lfloor \frac{\bar{\varphi}^i}{180^\circ} \right\rfloor\end{aligned}\quad (3.5)$$

A reminder: *Mathematical notation* $\lfloor x \rfloor$

The mathematical notation of $\lfloor x \rfloor$ denotes rounding down the decimal number x to the largest integer which does not exceed x .

Equation 3.3 is used with $\bar{\theta}^i$ and $\bar{\varphi}^i$ to establish the corresponding weights, and becomes

$$W_f^i = \frac{f(\bar{\theta}^i, \bar{\varphi}^i)}{\sum_{n=1}^m f(\bar{\theta}^i, \bar{\varphi}^i)}$$

Figure 3.6 illustrates the concepts presented above with a Normal distribution representing the variation of θ . With expected value $\mu = 150^\circ$ and standard deviation $\sigma = 22.5^\circ$, a significant portion of the area under the density function extends above $\theta = 180^\circ$ (red dashed line). The blue dashed line shows the conversion of the domain that exceeds 180° , according to Equation 3.4.

3.1.4.3 Fibre distribution schemes

The establishing of the user requested discretisation scheme that produces the groups (orientation and weight) was solved with various fibre distribution cases. There are different routines for the each case and are invoked using user-defined flag parameters. One case may handle aligned fibres, another may distribute the fibres based on bivariate normal distributions for θ and φ . The similarity of all cases is that they produce the orthonormal basis (with \mathbf{N}_f as the first axis) and the group weight W_f for all groups. The majority of all the cases follows the methods described in the previous sections. The procedure that goes into creating every group i for all $i \in \{1, 2, \dots, k\}$ where k is still the number of requested groups, is as follows.

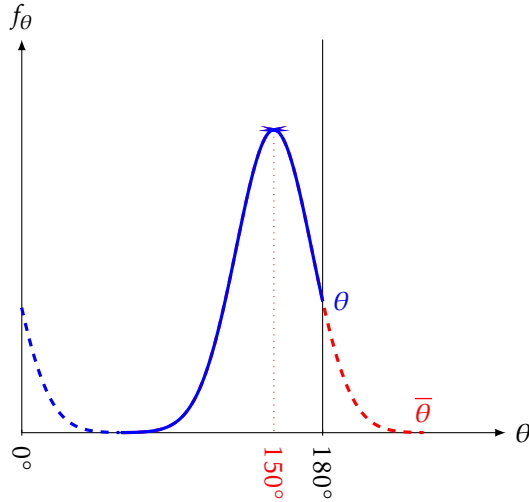


Figure 3.6: Normal density function for $\bar{\theta}$ converted into the domain of θ .

1. Establish $\bar{\theta}^i$ and $\bar{\varphi}^i$ based on requested domain and fibre distribution.
2. Establish W_f^i based on the given distribution parameters.
3. Convert $\bar{\theta}^i$ and $\bar{\varphi}^i$ to θ^i and φ^i
4. Establish N_f^i from θ^i and φ^i .
5. Establish the orthonormal basis \bar{X}^i based on N_f^i as first axis.
6. Establish transformation matrix Q^i from \bar{X}^i .

As the orientations of the fibres may vary from composite to composite, the complexity of the mathematical foundation needed to model the fibre distribution, will also vary. A handful of fibre distribution cases have been implemented in the present SFRM-model, but the user may need to add customised cases to the source code in order to model specific fibre distributions. The notion of cases creates an area within the FORTRAN source code where the user only needs to focus on developing the source code for step 1 through 3 in the

procedure stated above. In the presentation of the model framework in Section 3.1 and the example in Section 3.1.4.1, outlines for the cases which manage *aligned* and *in-plane univariate normal distributed* fibre phases were used to describe important aspects of the model. Table 3.1 presents an overview of all the cases currently implemented in SFRM-model. The corresponding figures in the table displays orientation vectors with colouring associated with the relative weight of each group. Red to blue color variation illustrates a decreasing relative weight exactly like in Figure 3.4.

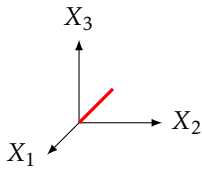
The only fibre distribution case that does not follow the outlined procedure stated above, is Case 5 in Table 3.1. This implementation uses Monte Carlo cycles which draw values for θ and φ from univariate normal distributions using the theory presented in Section 2.6.2. With this method, the whole fibre phase is represented by random samples rather than evaluating the fibre distribution through group discretisation. For every fibre sample a , a set of (θ^a, φ^a) values are drawn and used to create the orientation vector \mathbf{N}_f^a for the sample. All samples are weighted equal. If $k_{samples}$ is the total amount of samples drawn, then each sample weight W_f^a becomes

$$W_f^a = \frac{1}{k_{samples}}$$

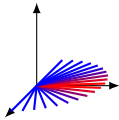
3.2 Pseudo formulation

With these concepts in place, a more compact formulation should be expressed to ease the source code implementation. The following section presents a pseudo formulation in Algorithm 1 of the SFRM-model. The first lines of establishing of the spherical angles are simplified and shortened due to the varying complexity in the fibre distribution cases.

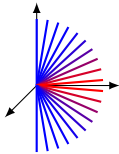
Table 3.1: Overview of implemented fibre distribution cases in the current SFRM-model.



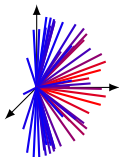
Case 1: Constant value θ and constant value φ .



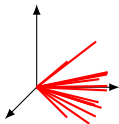
Case 2: Constant value for φ and univariate normal distribution for θ .



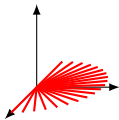
Case 3: Constant value for θ and univariate normal distribution for φ .



Case 4: Bivariate normal distribution for θ and φ .



Case 5: Monte Carlo cycling which draws from two individual univariate normal distributions for θ and φ .



Case 6: Uniform distribution of θ and constant value of φ .

```

for abaqus/explicit analysis using SFRM-model do
1  establish groups:  $\bar{\theta}^i$  and  $\bar{\varphi}^i \Rightarrow \theta^i$  and  $\varphi^i$ 
2  calculate  $W_f^i$ :  $W_f^i = \frac{f_{\theta,\varphi}^i(\bar{\theta}^i, \bar{\varphi}^i)}{\sum_{n=1}^m f_{\theta,\varphi}^n(\bar{\theta}^i, \bar{\varphi}^i)}$ 
3  establish  $N_f^i$ :  $N_f^i = [\sin(\varphi^i)\cos(\theta^i), \sin(\varphi^i)\sin(\theta^i), \cos(\varphi^i)]^T$ 
4  establish  $\bar{X}$ :
      if  $(1 - \textit{tolerance}) \leq |N_f^i \cdot X_1| \leq (1 + \textit{tolerance})$  then
         $\bar{X}^i = X$ 
      else
         $\bar{X}_1 = N_f^i$ ;  $\bar{X}_3 = \left( \frac{\bar{X}_1 \times X_2}{|\bar{X}_1 \times X_2|} \right)$ ;  $\bar{X}_2 = \bar{X}_3 \times \bar{X}_1$ 
      end
5  establish  $Q^i$ :
       $Q^i = \begin{bmatrix} (\bar{X}_1^1)^i & (\bar{X}_1^2)^i & (\bar{X}_1^3)^i \\ (\bar{X}_2^1)^i & (\bar{X}_2^2)^i & (\bar{X}_2^3)^i \\ (\bar{X}_3^1)^i & (\bar{X}_3^2)^i & (\bar{X}_3^3)^i \end{bmatrix}$ 
foreach step do
  foreach increment do
    foreach integration point do
      foreach group do
6        establish  $\sigma_m^j$ : from constitutive model for matrix phase
7        calculate  $\lambda_f^{j,i}$ :  $\lambda_f^{j,i} = \sqrt{(N_f^i)^T (E^j)^T (E^j) (N_f^i)}$ 
8        calculate  $\varepsilon_f^{j,i}$ :  $\varepsilon_f^{j,i} = \ln(\lambda_f^{j,i})$ 
9        calculate  $\sigma_f^{j,i}$ :  $\sigma_f^{j,i} = E_f \varepsilon_f^{j,i}$ 
10       calculate  $\bar{\sigma}_m^{j,i}$ :  $\bar{\sigma}_m^{j,i} = (Q^i)(\sigma_m^j)(Q^i)^T$ 
11       establish  $\bar{\sigma}_f^{j,i}$ 
          if conditions are met then
             $\bar{\sigma}_{11,m}^{j,i} = \sigma_f^{j,i}$ 
             $\bar{\sigma}_f^{j,i} = \bar{\sigma}_m^{j,i}$ 
          else
             $\bar{\sigma}_f^{j,i} = \bar{\sigma}_m^{j,i}$ 
          end
12       calculate  $\sigma_f^{j,i}$ :  $\sigma_f^{j,i} = (Q^i)^T (\bar{\sigma}_f^{j,i}) (Q^i)$ 
13       calculate  $\sigma^j$ :  $\sigma^j = \left( \sum_{i=1}^k \sigma_f^{j,i} W_f^i \right) v_f + \sigma_m^j (1 - v_f)$ 
      end
    end
  end
end
end

```

Algorithm 1: Pseudo formulation of SFRM-model.

3.3 FORTRAN implementation

The development of the FORTRAN implementation was made with the *Intel® Visual Fortran Composer XE 2013 Update 5* including *Intel® Visual Fortran Compiler Version 13.1.3*, and *Abaqus 6.14*.

The FORTRAN compiler supports automatic parallelization, so the source code was developed with parallel computing, software efficiency and readability in mind; i.e., shared memory dependency should be kept to a minimum to allow for parallel execution of the code. Difficulties arose when developing the implementation for the group weights and transformation matrices. These values should be established the first time the VUMAT subroutine is called (analysis time equals zero) and then be used throughout the analysis. Due to the design of the subroutine interface in Abaqus and the FORTRAN programming language, it proved difficult to pass these matrices (or multidimensional arrays) to the subroutine for each time the VUMAT is called. The chosen solution was to save these two arrays as *common blocks*. A Common block is a native feature in FORTRAN which allows several programs to share a specified part of memory between them. This use of common blocks may introduce memory dependencies within the subroutines.

3.3.1 Source code structure

The main flow of the FORTRAN implementation is presented in Algorithm 2. The implementation of the SFRM-model was solved by dividing the source code into several subroutines whilst trying to follow the logical flow presented in Section 3.1. As presented in Algorithm 2, the subroutine which calculates the stress of the matrix phase, *SMATRIX()*, is called each time the VUMAT subroutine is called. If the analysis time equals zero, the subroutine that handles the fibre discretisation and weighting, *SFD()*, is called. The subroutine that calculates the stress in the fibres and combines the contributions from the phases into a final stress tensor is denoted *SFIBER()* and is the final module to be called in the VUMAT. As the matrix definition is arbitrary, an explicit presentation of the implemented source code will not be included in this thesis. However, an outline of the currently applied matrix model is presented in Section 3.4. The full VUMAT subroutine with the SFRM-model implemented

contains over 900 lines of FORTRAN code. The FORTRAN source code for the SFIBER() and SFD() subroutines can be found in Appendix A.1 and Appendix A.2, respectively.

```

subroutine VUMAT()
1  |  subroutine SMATRIX()
   |  if analysis time equals zero then
2  |      subroutine SFD()
   |  end
3  |  subroutine SFIBER()
   end

```

Algorithm 2: Pseudo formulation of the FORTRAN implementation.

3.4 Applied matrix model

Although an arbitrary constitutive relation may be applied to model the matrix phase, a tangible implementation is needed in the following chapters herein. The matrix implementation presented in [7] will be used as a basis for the matrix phase in the further exploration of the SFRM-model. For a thorough presentation of the matrix implementation, the reader is therefore referred to [7]. However in the following section, the respective matrix model is rendered with respect to the theory presented in Section 2.4.2.

The matrix material is modelled with an elastic-plastic behavior. The elastic behavior is modelled with isotropic linear elasticity and a Drucker-Prager model is used for plasticity. The Drucker-Prager yield criterion is pressure sensitive i.e. dependent on the hydrostatic pressure and therefore often suitable for plasticity modelling of polymers which may experience phenomena such as void growth. The matrix model considers the initial yield stress to have different values for compression, $\sigma_{0,C}$, and tension, $\sigma_{0,T}$. The plastic retraction coefficient ν_p governs the matrix model's compressibility where $\nu_p = 0.5$ gives an incompressible plastic flow. The evolution of the flow stress σ_y is according to an isotropic hardening relation which is given in Equation 3.6.

$$\sigma_y = \sigma_{0,T} + R(p) \quad \text{where} \quad R(p) = k_1 p + k_2 [1 - \exp(-mp)] \quad (3.6)$$

Table 3.2: Table-structure for fibre parameters.

V_f	E_f	Groups	Case	Case variables
Fibre volume fraction.	Young's modulus for fibres.	Number of fibre groups.	Case number. See Tab. 3.1.	Case specific parameters. May range from 1 to 10 parameters.

Table 3.3: Table-structure for matrix parameters.

$\sigma_{0,T}$	$\sigma_{0,C}$	E_m	ν_e	ν_p	k_1	k_2	m
Initial yield stress in tension.	Initial yield stress in compression.	Young's modulus for matrix.	Elastic Poisson's ratio.	Plastic retraction coefficient.	See Eq. 3.6.	See Eq. 3.6.	See Eq. 3.6.

3.5 User-defined parameters

In order to systematically present the user-defined parameters that are used with the SFRM-model in the analyses for the succeeding chapters of this report, a table-structure was established. Two separate tables will be used to present the parameters used by the fibre modules (i.e. SFIBER and SFD) and the matrix module (i.e. SMATRIX). The structure of the two tables are presented in Table 3.2 and Table 3.3. In Table 3.2, a set of *Case variables* will present the parameters used by fibre distribution cases presented in Table 3.1. The numbers of parameters demanded by each case varies.

Chapter 4

Verification

«Are you building it right?»

In the development of the SFRM-model, there were possibly two major sources of error: Flaws in the mathematical foundation and mistakes in the software implementation of the mathematical foundation. This section presents the outline and some details of the effort that went into the reducing the chance of the latter.

4.1 Preliminary controls

In software development, the chance of software bugs¹ being introduced into the program is always present. During the development of the VUMAT subroutine in FORTRAN, a continuous quality control of the code was performed in order to verify the model implementation. Examples of the steps that went into this quality control are:

- Modularised prototypes of the model framework were implemented in Python in order to compare it to the results produced by the FORTRAN implementation of the SFRM-model. The prototyping of functions and subroutines in Python has served as a valuable tool.
- Symbolic matrix operations were preformed in MATLAB and transferred over to the FORTRAN source code in order to prevent mathematical errors.

¹A software bug is an error or flaw in a computer program.

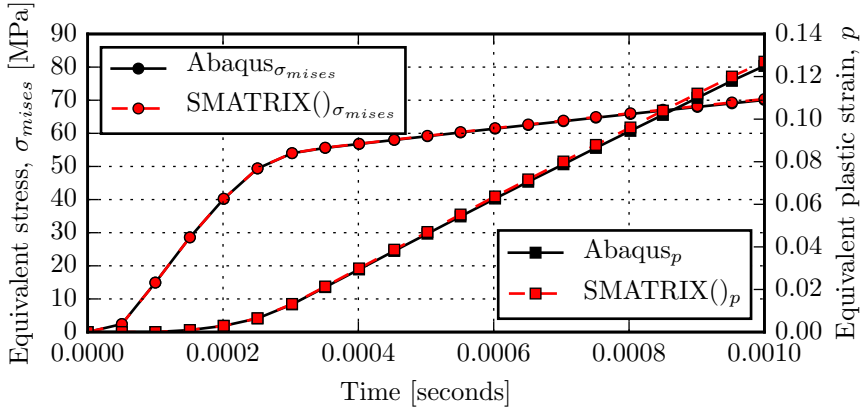


Figure 4.1: Comparison of the equivalent stress and equivalent plastic strain produced by the native Drucker-Prager plasticity model in Abaqus and the implemented SMATRIX().

- Raw data of preliminary results produced by the FORTRAN implementation was extracted and Python was used to produce graphical plots.
- Command line output of results produced by the FORTRAN implementation.
- Interpretation of results produced by preliminary analyses in Abaqus /Explicit running with the FORTRAN implementation.

4.2 Comparison with native Abaqus model

In order to isolate a possible source of error, the current matrix implementation of the SFRM-model was compared to the native Drucker-Prager plasticity model available in Abaqus. A simple analysis was run where two cubes, each with separate material definitions, were pulled in tension with the matrix parameters presented in Table 4.1. The equivalent plastic strain p and the von Mises equivalent stress σ_{mises} for the two models are presented in Figure 4.1. The results for σ_{mises} coincide while some minor deviations can be observed

Table 4.1: Matrix material data for the analysis in Section 4.2.

$\sigma_{0,T}$ [MPa]	$\sigma_{0,C}$ [MPa]	E_m [MPa]	ν_e	ν_p	k_1 [MPa]	k_2 [MPa]	m
20	-30	1500	0.4	0.1	139	32.7	319.4

for p . The small deviations seen may be related to how the equivalent plastic strain is calculated by Abaqus.

4.3 Comparison with semi-analytical solution

For configurations where fibres are aligned in the loading direction, a simple semi-analytical solution exists through Equation 3.1 which becomes

$$\sigma_{22} = v_f E_f \varepsilon_{22} + (1 - v_f) \sigma_{22,m}. \quad (4.1)$$

$\sigma_{22,m}$ is obtained by running an analysis where the pure matrix model ($v_f = 0.0$) is used. This gives a semi-analytical solution which depends on the finite element solution for the pure matrix material, and the analytical solution for the fibre contribution. This approach isolates and reveals possible inconsistencies in the fibre implementation of the SFRM-model.

4.3.1 Model and analyses description

The analyses were made with a single 1mm^3 C3D8 linear solid fully integrated element in Abaqus/Explicit with large strains. For aligned fibres, one group is sufficient to model the fibres contribution (i.e. $\mathbf{N}_f(\theta, \varphi)$ with $W_f = 1$). The model is illustrated in Figure 4.2 and fibre direction is illustrated in Figure 4.3. The different colours of the nodal sets refer to applied boundary conditions:

- The red node is fixed.
- The blue nodes are restrained from translation in the X_2 -direction.
- A displacement $u_2 = \pm 0.05\text{mm}$ is applied to the green nodes in X_2 -direction.

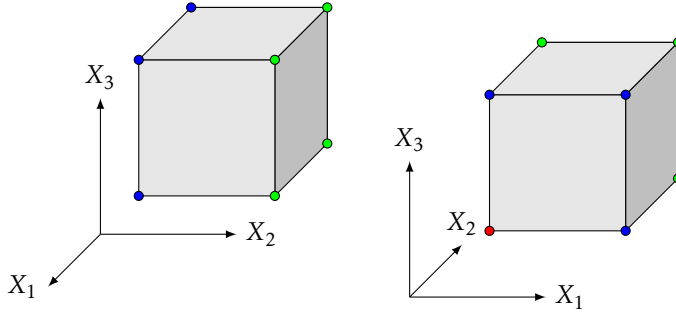


Figure 4.2: Finite element model used for comparison with semi-analytical solution. The colours of the nodal sets refer to varying boundary conditions.

A positive displacement $u_2 = 0.05\text{mm}$ results in a final true strain equal to

$$\varepsilon_{22}^{final} = \ln\left(1 + \frac{0.05}{1}\right) = 0.04879$$

while a negative displacement $u_2 = -0.05\text{mm}$ results in final true strain equal to

$$\varepsilon_{22}^{final} = \ln\left(1 + \frac{-0.05}{1}\right) = -0.05129.$$

Table 4.2: Fibre parameters applied in Section 4.3.

V_f	E_f [GPa]	Groups	Case	$\theta_{constant}$	$\varphi_{constant}$
0.3	72.0	1	1	90°	90°

Table 4.3 and Table 4.2 summarises the elastic-plastic material behavior for the matrix and the parameters related to the fibre implementation, respectively.

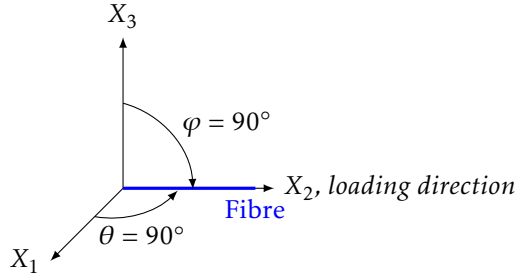


Figure 4.3: Illustration of the fibre alignment for comparison with the semi-analytical solution.

Table 4.3: Matrix material data for the analyses in Section 4.3.

$\sigma_{0,T}$ [MPa]	$\sigma_{0,C}$ [MPa]	E_m [MPa]	ν_e	ν_p	k_1 [MPa]	k_2 [MPa]	m
40	-40	2100	0.3	0.5	139	32.7	319.4

4.3.2 Results

The results from tension and compression are presented in Figure 4.4 and Figure 4.5, respectively. The results from the SFRM-model and semi-analytical solution (i.e. Equation 4.1) coincide, with

$$\begin{aligned} \sigma_{22}^{final} = 1099 \text{ MPa} & \quad \text{for} \quad \varepsilon_{22}^{final} = 0.04879 & \quad \text{and} \\ \sigma_{22}^{final} = -1168 \text{ MPa} & \quad \text{for} \quad \varepsilon_{22}^{final} = -0.05129. \end{aligned}$$

4.4 Comparison with literature

As a means of verification, the SFRM-model was compared to results presented in [7]. The analyses in the article examines a variety of modeling configurations, such as different element discretisations and boundary conditions, material models for the matrix material, fibre distributions and material

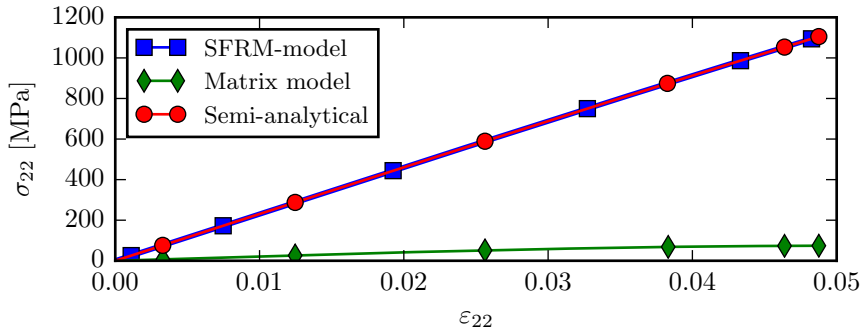


Figure 4.4: Results from tension (i.e. final $u_2 = 0.05mm$).

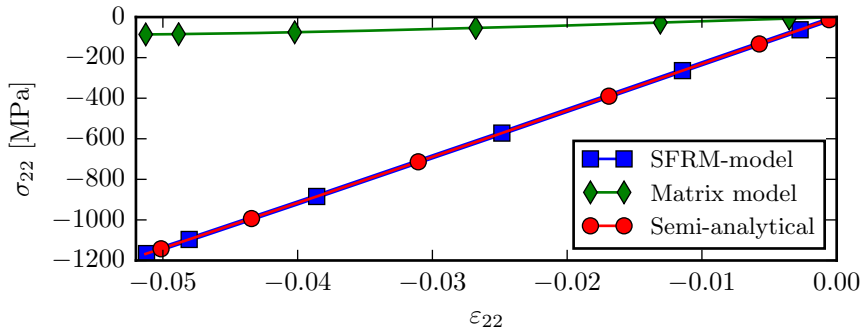


Figure 4.5: Results from compression (i.e. final $u_2 = -0.05mm$).

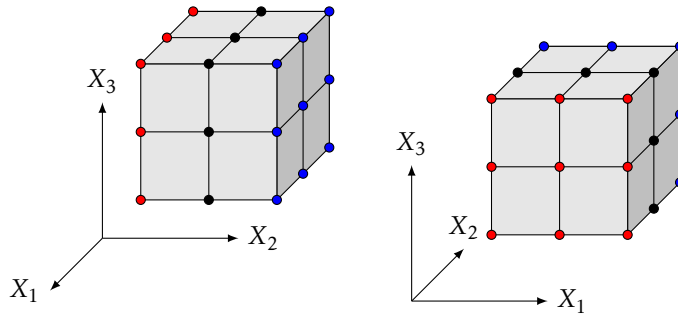


Figure 4.6: Finite element model for the tension and compression analyses presented in [7]. Nodal sets with different colours refers to different boundary conditions.

properties for the fibres. The focus of the verification process for the SFRM-model has been to replicate the tension and compression analyses in [7]. Since this section is dedicated to comparison with an existing model, discussion concerning the presented result is confined merely to deviations between the two models. For an evaluation of the results related to this section, the reader is referred to [7].

4.4.1 Model and analyses description

The finite element model consists of a 1 mm^3 cube discretised into eight C3D8 linear solid elements with full integration (i.e. eight integration points per element). Figure 4.6 illustrates the model discretisation along with colour codes for different nodal sets:

- The red nodes are fixed.
- The blue nodes are restrained from translation in the $X_1 X_3$ -plane ($u_1 = u_3 = 0$) and subjected to a prescribed displacement in the X_2 -direction which becomes $\pm 0.05 \text{ mm}$ at the end of the analyses.
- The black nodes are unrestrained.

The analysis time was sufficiently low to ensure quasi-static conditions.

Table 4.4: Fibre data for the analyses in Section 4.4. The notation seen under $\theta_{constant}$ is meant to be understood as a set with lower bound 0° , upper bound 90° and increment size 5° .

V_f	E_f [GPa]	Groups	Case	$\varphi_{constant}$	$\theta_{constant}$
0.3	72.0	1	1	90°	$\{0^\circ: 5^\circ:90^\circ\}$

A clarification

The described model configuration may at first seem unsuited for tensile and compression analyses. The applied boundary conditions heavily constrains the model which restricts transverse retraction at the boundaries. After inspecting the behaviour of the SFRM-model, it became evident that a model consisting of a few number of elements needs to be restrained in order to yield comparable results as the orientation of the fibres was varied. For example, the one-element-model which was used in Section 4.3 produces incomparable results in a set of analyses where the orientation of the fibre is varied. Fibre representations which are not axis-aligned results in skewing of the single element with uniaxial displacement and the strain amplitudes will not be comparable.

Also, the definition of θ in [7] is not the same as the definition in this report. This angle representation, and the subindices for strains and stresses have been changed to fit the coordinate systems and direction of loading of this report.

The analyses are meant to simulate an aligned orientation of fibres. The fibres are therefore represented with only one group for each analysis. For both tension and compression, 19 analyses were run where φ was kept equal to 90° and θ was changed for each analysis. θ was changed between 0° and 90° with step size of 5° . The data for the fibre is given in Table 4.4 and an illustration for the described fibre orientation is given in Figure 4.7.

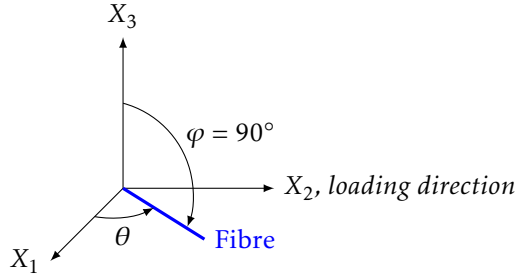


Figure 4.7: Illustration of the fibre alignment for the tension/compression analyses.

Table 4.5: Matrix material data for the analyses in Section 4.4.

$\sigma_{0,T}$ [MPa]	$\sigma_{0,C}$ [MPa]	E_m [MPa]	ν_e	ν_p	k_1 [MPa]	k_2 [MPa]	m
29	-40	2100	0.3	0.1 if $\sigma_H \geq 0$ 0.5 if $\sigma_H < 0$	139	32.7	319.4

In [7], the matrix was modelled with incompressible plastic flow in compression so the plastic retraction coefficient ν_p is set to 0.5 for $\sigma_H < 0$. When the matrix phase is subjected to tension $\sigma_H \geq 0$, the volume is allowed increase as $\nu_p = 0.1$. The matrix parameters which were used are stated in Table 4.5.

4.4.2 Uncertainties in the comparison

There are a few issues when attempting to replicate the results in [7].

- The article only specifies where the stress is sampled from for Fig.3². There, Notta-Cuvier et al. [7] presents a figure where *the axial stress is computed at the elements centroids*, though only presenting data corresponding to one variable set. The element model consists of eight fully integrated elements which, due to the nature of the model, produce different centroid values. There is no mention of where other variables are

²The Fig.-notation refers to the figure labels in [7].

sampled from. The data presented for the SFRM-model in the following sections are the average value of all integration points in the model (i.e. average for all centroids).

- The data sets were retrieved from the article using software developed for extracting data from graphical plots. This method of extracting raw data will most likely introduce some small deviations from the original data used.

4.4.3 Results from tension

Figure 4.8 states the results from Fig.2 along with the corresponding results from the SFRM-model. The SFRM-model yields considerable higher values of σ_{22} for $\theta > 50^\circ$. The stress deviation at $\theta = 90^\circ$ is 56 MPa. Figure 4.9 gives the transverse strains ε_{11} and ε_{33} at the end of the analyses for the SFRM-model and the data retrieved from Fig.5 including the corresponding pure matrix values for both models. The deviations are major, and also apparent in the comparison in Figure 4.10 which presents relative volume variations according to Equation 4.2.

$$\frac{\Delta V}{V_0} = \exp[\varepsilon_{11} + \varepsilon_{22} + \varepsilon_{33}] - 1 \quad (4.2)$$

Despite these deviations, the trends in both models are distinctively similar.

4.4.4 Results from compression

The results from the SFRM-model and the model in [7] corresponds much better in compression where the plastic flow is isochoric. Figure 4.11 illustrates the same deviation pattern as in Figure 4.8, but the compressive stresses are lower for the model developed in this thesis. The results from the figures related to the strains, Figure 4.12 and 4.13, corresponds better than for tension, yielding almost coinciding results for $\theta < 50$.

4.5 Evaluation of verification

As seen in the comparison of the native Drucker-Prager in Abaqus and the implemented SMATRIX(), the matrix model currently applied to the SFRM-

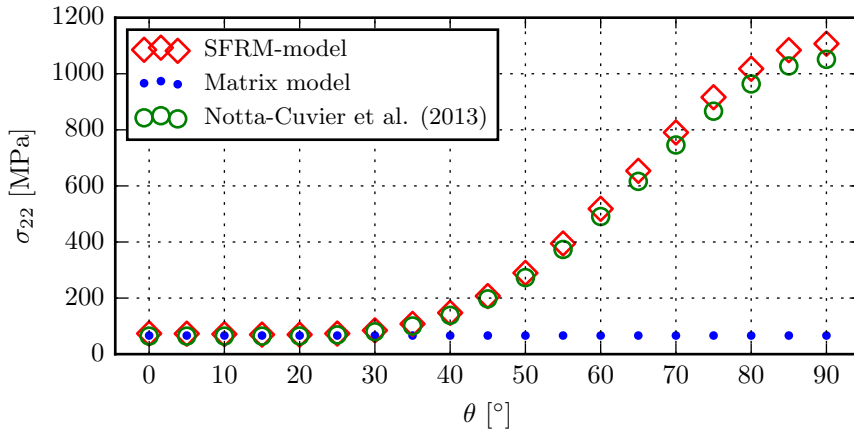


Figure 4.8: Results from tension at the end of the analyses. Comparison with Fig.2 in [7].

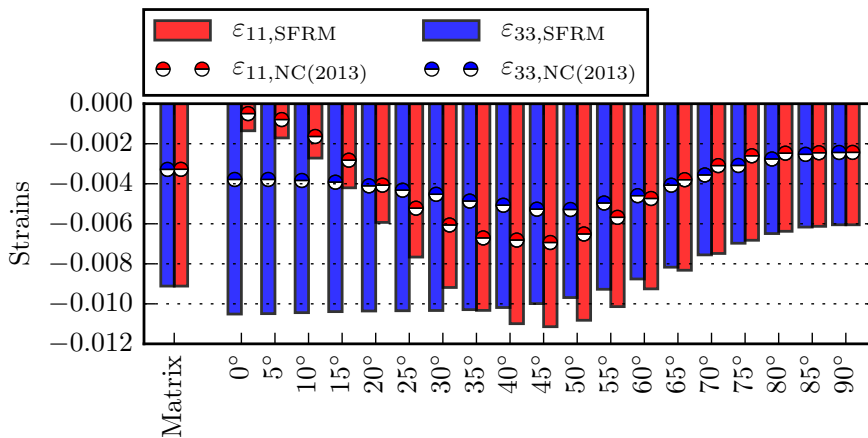


Figure 4.9: Results from tension at the end of the analyses. Comparison with Fig.5 in [7]. The notation NC(2013) refers to Notta-Cuvier et al. [7].

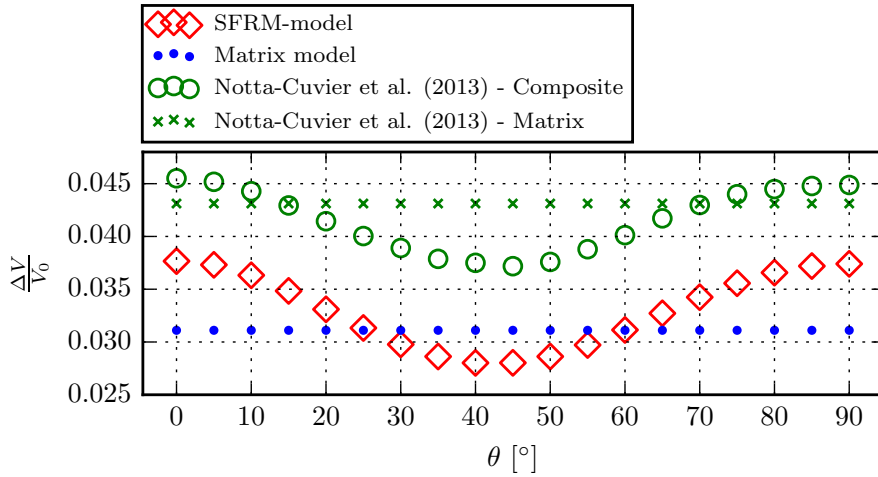


Figure 4.10: Results from tension at the end of the analyses. Comparison with Fig.6 in [7].

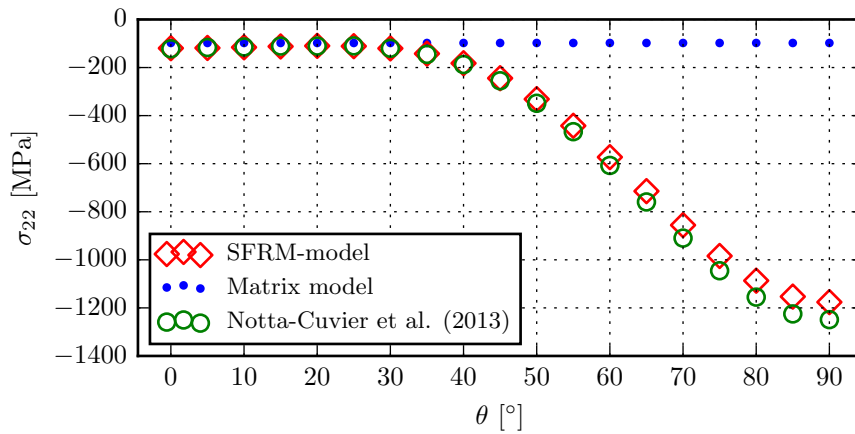


Figure 4.11: Results from compression at the end of the analyses. Comparison with Fig.9 in [7].

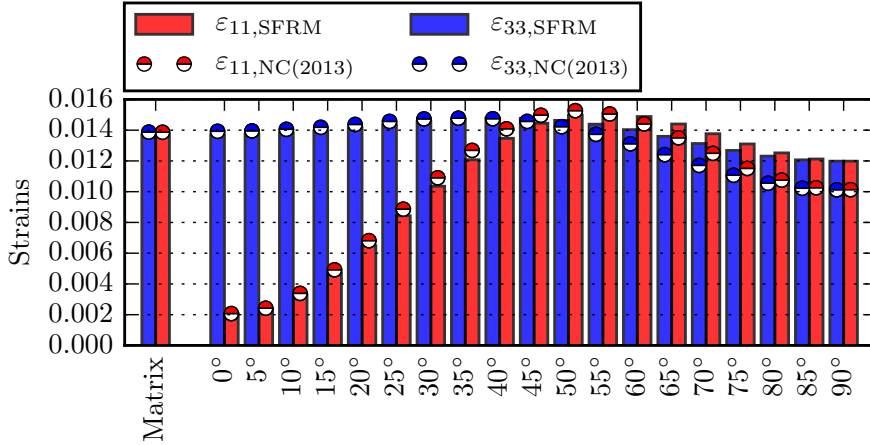


Figure 4.12: Results from compression at the end of the analyses. Comparison with Fig.12 in [7]. The notation NC(2013) refers to Notta-Cuvier et al. [7].

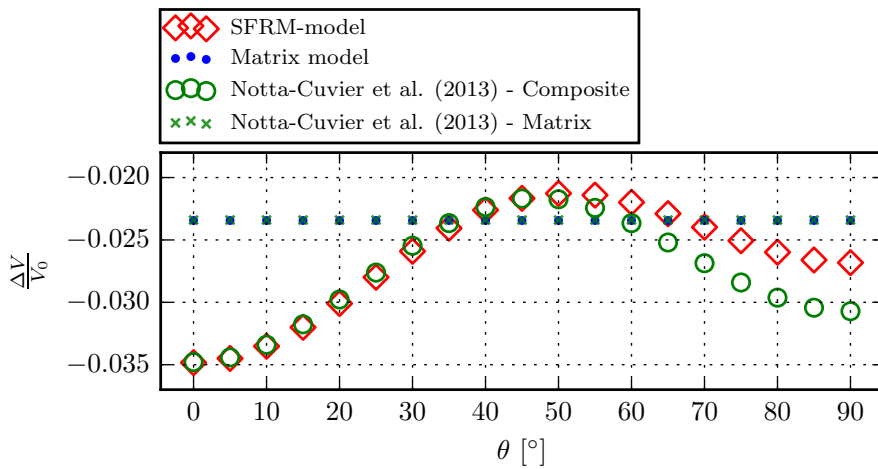


Figure 4.13: Results from compression at the end of the analyses. Comparison with Fig.6 in [7].

model seems to yield reasonable results. Some minor deviations were observed, but this is reasoned to be related to the computation of the equivalent plastic strain within Abaqus as the strain components from the analysis, coincide. It is concluded that the current implementation of SMATRIX() is working properly.

The comparison with the semi-analytical solution is seen to yield coinciding results. The analysis made with the SFRM-model in Section 4.3 may seem simple, but it verifies the majority of the core features implemented in the SFD() and SFIBER().

Deviations between the SFRM-model and the model from [7] for higher values of θ are observed in the figures displaying stress data, Figure 4.8 and Figure 4.11, for both tension and compression. Deviations in the same range of θ is also observed in the figure for the transverse strains, Figure 4.12, and the volume variations, Figure 4.13, for compression. However, major deviations are seen in the equivalent figures for tension, Figure 4.9 and Figure 4.10. A shift in the values are seen in both these figures which is also the case for the neat matrix model. Some of these deviation may be related to the uncertainties presented in Section 4.4.2, but as results from compression seem to almost coincide, this is reasoned not be the most prominent source of this deviation. A simple estimate of the transverse strains for the pure matrix material in the tension configuration are therefore made and presented in the framed box below.

An estimate: Transverse strains for matrix model

The longitudinal stress and longitudinal strain, i.e. in the direction of loading, for tension are about

$$\sigma = 65 \text{ MPa} \quad \text{and} \quad \varepsilon_l = 0.05.$$

By decomposition of the transverse and longitudinal strain, one has

$$\varepsilon_l = \varepsilon_l^{elastic} + \varepsilon_l^{plastic} \quad \text{and} \quad \varepsilon_w = \varepsilon_w^{elastic} + \varepsilon_w^{plastic}$$

where ε_w denotes the total transverse strain which can be related to ε_{11} and ε_{33} in Figure 4.9. The following relations are assumed to apply:

$$\varepsilon_l^{elastic} = \frac{\sigma}{E_m}, \quad \varepsilon_w^{elastic} = -\nu_e \varepsilon_l^{elastic} \quad \text{and} \quad \varepsilon_w^{plastic} = -\nu_p \varepsilon_l^{plastic}.$$

Finally,

$$\varepsilon_w = -\nu_e \frac{\sigma}{E_m} - \nu_p \left(\varepsilon_l - \frac{\sigma}{E_m} \right) = -0.3 \frac{65}{2100} - 0.1 \left(0.05 - \frac{65}{2100} \right) = -0.011.$$

From Figure 4.9,

$$\varepsilon_{11,SFRM} = \varepsilon_{33,SFRM} = -0.0093 \quad \text{and} \\ \varepsilon_{11,NC(2013)} = \varepsilon_{33,NC(2013)} = -0.0033$$

for the pure matrix.

The estimate of the transverse strains is expected to be lower than what yielded by the element discretisation in Section 4.3.1 due to the restrains at the boundaries. It is seen that the estimate coincides better with the results from the SFRM-model than with what presented by Notta-Cuvier et al. [7].

As the comparisons presented in this chapter seem to yield reasonable results, the SFRM-model is considered to be working according to the foundation presented in Chapter 3.

Chapter 5

Validation

«Are you building the right thing?»

An important requisite when building a material model is that it actually replicates the mechanical behaviour of the physical material. In this chapter, the SFRM-model will be applied to the experimental data presented in the master's thesis of Anne Amundsen [11]. The thesis evaluates the mechanical behaviour of injection moulded glass fibre reinforced polypropylene with varying fibre content. An extensive series of tests with multiple repetitions were performed for all relevant materials in uniaxial tension, bending and for a plate with a centric hole. This chapter is concerned with applying the SFRM-model to the uniaxial tension tests from this thesis.

5.1 Materials

Three materials with three different fibre contents were tested. The three materials were denoted *PP*, *PP10* and *PP30* which is polypropylene with fibre *weight contents* of 0%, 10% and 30%, respectively. The samples in [11] were cut out of plates made of the same materials as Andreas Koukal used in his PhD thesis [31]. Prior to testing, the materials used by Amundsen [11] were stored in an office at room temperature for more than one year.

Amundsen [11] lists some material properties found in the data sheets issued by the material producer SABIC. As the *PP10* was exclusively made for Koukal [31], no material data are supplied by the producer for this specific

Table 5.1: Nominal material data for PP, PP10 and PP30 retrieved from Amundsen [11].

Material	Material density ρ [kg/m ³]	Initial yield stress σ_0 [MPa]	Tensile modulus E [MPa]	Fibre weight fraction m_f
PP	905	36	1750	0
PP10	-	-	-	0.10
PP30	1120	-	6650	0.30

material. A relevant selection of the available material data are summarised in Table 5.1 of this thesis.

5.2 Calibration of the SFRM-model

In order for the SFRM-model to produce comparable results, some material parameters need to be established. The following section documents the process of determining suitable material parameters for the fibre and matrix modules of the SFRM-model.

5.2.1 Weight fraction conversion

The relationship between the fibre volume fraction v_f and the fibre weight fraction m_f of each material can be expressed by Equation 5.1 through the material densities of each phase.

$$m_f = \frac{M_f}{M_m + M_f} = \frac{\rho_f v_f}{(\rho_m v_m + \rho_f v_f)} \Rightarrow v_f = \frac{\rho_m}{\rho_f \left(\frac{1-m_f}{m_f} \right) + \rho_m} \quad (5.1)$$

It is reminded that $v_f = 1 - v_m$. M_f and M_m denotes the mass of the fibres and mass of the matrix, respectively. Assuming that the density of the unreinforced polypropylene (i.e. PP) equals the density of the matrix phase in the two other materials (i.e. ρ_m), ρ_f remains to be determined. By using the total

Table 5.2: Calculated values for PP, PP10 and PP30. Values with the colour red are calculated values.

Material	Material density ρ [kg/m ³]	Fibre weight fraction m_f	Fibre volume fraction v_f
PP	905	0.0	0.000
PP10	966	0.10	0.038
PP30	1120	0.30	0.134

density value for one of the fibre reinforced materials ρ , ρ_f can be established as done in Equation 5.2.

$$\rho = \frac{mass}{volume} = \frac{\rho_f v_f + \rho_m v_m}{v_f + v_m} \Rightarrow \rho_f = \frac{\rho - \rho_m(1 - v_f)}{v_f} \quad (5.2)$$

Inserting Equation 5.2 into Equation 5.1 results in Equation 5.3.

$$v_f = 1 - \frac{\rho}{\rho_m}(1 - m_f) \quad (5.3)$$

By using the total density value for PP30, the estimated fibre volume fraction and density becomes what is stated in Equation 5.4.

$$\begin{aligned} v_f &= 0.134 \\ \rho_f &= 2513 \text{ kg/m}^3 \end{aligned} \quad (5.4)$$

Equation 5.1 and the estimated value of ρ_f are consistent with what stated by Koukal [31]. Table 5.2 presents the fibre contents produced through these equations for the three materials.

5.2.2 Calibration of matrix model

The experimental tensile test results for PP presented in [11] was used to calibrate the model for the matrix phase. The results presented by Amundsen

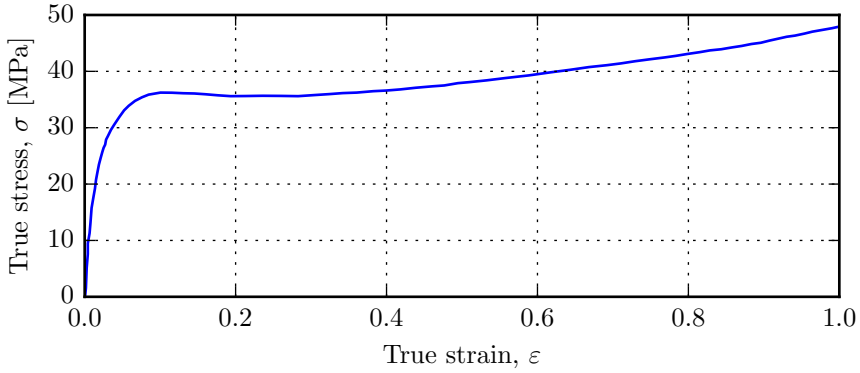


Figure 5.1: Experimental data from a representative data set for the uni-axial tensile test for unreinforced polypropylene (PP) in [11].

[11] revealed that this PP has an isotropic mechanical behaviour. The linear exponential hardening law from Equation 3.6 which is already implemented in the matrix model was used to model the isotropic evolution of the yield surface. However, the relationship needs to be calibrated to the experimental data in order to establish the coefficients k_1 , k_2 and m . The graphs presenting the transverse and longitudinal strain will be used to estimate the elastic Poisson's ratio and plastic retraction coefficient. The retrieved data sets from [11] are presented in Figure 5.1 and Figure 5.2.

5.2.2.1 Young's modulus

Table 5.1 contains the Young's modulus for PP retrieved from the material data sheets given by the material producer. Amundsen [11] found the Young's modulus to be equal 1508 MPa for PP. Therefore,

$$E_m = 1508 \text{ MPa.}$$

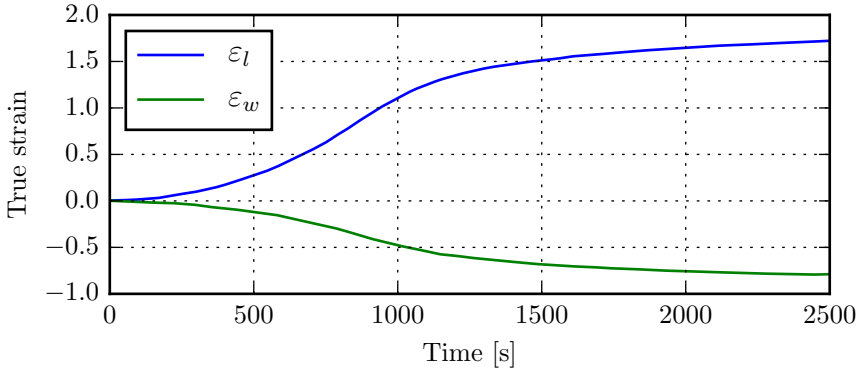


Figure 5.2: Longitudinal and transverse strains as a function of time retrieved from [11].

5.2.2.2 Retraction ratios

The longitudinal strain ε_l and the transverse strain ε_w from the uniaxial tensile tests of PP were retrieved from [11] and are presented in Figure 5.2. w and l corresponds to the X_1 - and X_2 -directions in Figure 5.8, respectively. From the sampled strain values for when $\varepsilon_l \ll 0.02$ ($\approx \frac{\sigma_0}{E_m}$), the elastic Poisson's ration was estimated as

$$\nu_e = -\frac{\varepsilon_w}{\varepsilon_l} \Big|_{\varepsilon_l \ll 0.02} \approx 0.48.$$

Koukal [31] found that $\nu_e = 0.41$, but it is here chosen to base the matrix parameters on the results of [11] as this is the source of comparison. The plastic retraction coefficient ν_p was established using the definition

$$\nu_p = -\frac{\varepsilon_w^p}{\varepsilon_l^p} \quad (5.5)$$

where ε_w^p and ε_l^p are the plastic strain components. Through decomposition of the total longitudinal and transverse strains, the plastic components can be expressed as

$$\varepsilon_l^p = \varepsilon_l - \varepsilon_l^e \quad \text{and} \quad \varepsilon_w^p = \varepsilon_w - \varepsilon_w^e.$$

The elastic strain component ε_l^e is calculated from

$$\varepsilon_l^e = \frac{\sigma}{E_m}.$$

The definition of the Poisson's ratio gives

$$\nu_e = -\frac{\varepsilon_w^e}{\varepsilon_l^e} \Rightarrow \varepsilon_w^e = -\nu_e \varepsilon_l^e = -\nu_e \frac{\sigma}{E_m}$$

where σ is the uniaxial stress from Figure 5.1 where $\varepsilon = \varepsilon_l$. By substitution of the presented relations into Equation 5.5, the plastic retraction coefficient can be expressed as

$$\nu_p = -\frac{\varepsilon_w^p}{\varepsilon_l^p} = -\frac{\varepsilon_w + \nu_e \frac{\sigma}{E_m}}{\varepsilon_l - \frac{\sigma}{E_m}}. \quad (5.6)$$

Figure 5.3 presents the variation of Equation 5.6 as a function of time. Strains sampled before experiment time equal to approximately 400 seconds are omitted as these represent elastic material behavior. The true stress data available in [11] is limited to $\varepsilon_l \leq 1.0$ which corresponds to an experiment time approximately equal to 900 seconds, the results presented in Figure 5.3 are limited to experiment time less than 900 seconds. A constant value for ν_p is estimated by taking the average value of Equation 5.6 between 400 and 900 seconds, and becomes

$$\nu_p = 0.42.$$

5.2.2.3 Strain hardening law

The coefficients in Equation 3.6 was calibrated with the data presented in Figure 5.1. The Young's modulus for the matrix material has already been established as 1508 MPa. In Figure 5.4, the experimental uniaxial results from Figure 5.1 are displayed along with the elastic stress relation

$$\sigma = E_m \varepsilon.$$

The two graphs intersect at

$$\sigma = 17.4 \text{ MPa}$$

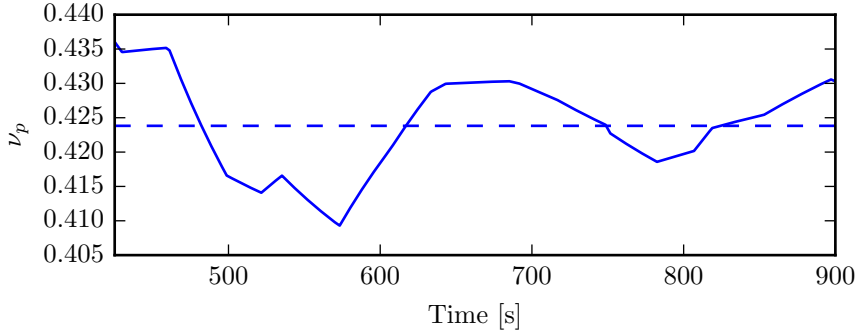


Figure 5.3: A single value for the plastic contraction coefficient was established as the average value of ν_p as a function of experiment time. ν_p was estimated using Equation 5.6.

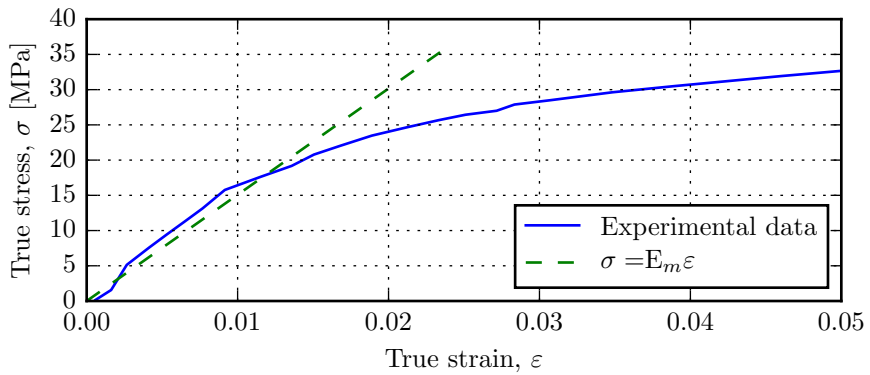


Figure 5.4: The experimental tensile test data presented along with $\sigma = E_m \epsilon$ in order to determine a suitable starting point to fit the implemented strain hardening relation.

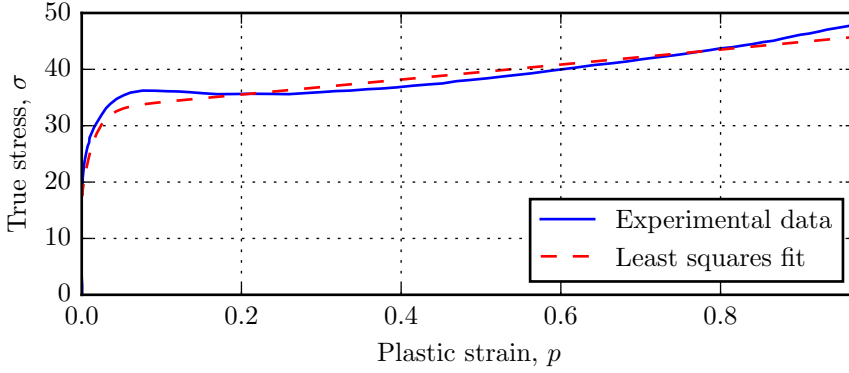


Figure 5.5: Equation 3.6 fitted to experimental results for true stress as a function of the plastic strain p according to Equation 5.7.

which then becomes the natural choice of model yield stress rather than the nominal value from Table 5.1. Equation 3.6 is a function of the equivalent plastic strain p , and in the case of uniaxial tension

$$p = \varepsilon^p = \varepsilon - \varepsilon^e = \varepsilon - \frac{\sigma}{E_m}. \quad (5.7)$$

A non-linear least squares method was used to fit Equation 3.6 to the data in Figure 5.1 with the elastic contribution subtracted as in Equation 5.7. If $\sigma_{y,i}$ denotes a stress point produced by Equation 3.6, and σ_i denotes the corresponding experimental stress point from Figure 5.1 at p_i , a least squares method will find the optimal set of k_1 , k_2 and m so that

$$\sum_{i=1}^n (\sigma_{y,i} - \sigma_i)^2$$

is minimised. The results are illustrated in Figure 5.5 and the parameters are presented in Table 5.3 along with the rest of the material parameters related to the matrix model used in this work. As no compression results are presented for PP in [11], it is assumed that

$$\sigma_{0,T} = \sigma_0 \text{ and } \sigma_{0,C} = -\sigma_0.$$

Table 5.3: Established material parameters for the matrix model used in Chapter 5.

$\sigma_{0,T}$ [MPa]	$\sigma_{0,C}$ [MPa]	E_m [MPa]	ν_e	ν_p	k_1 [MPa]	k_2 [MPa]	m
17.4	-17.4	1508	0.48	0.42	13.3	15.5	66.1

5.3 Tensile test specimen

The uniaxial tensile test specimens used by Amundsen [11] were machined from injection moulded plates made out of PP, PP10 and PP30. The nominal geometry of the specimens is presented in Figure 5.6. For all three materials, specimens were cut in 0° , 45° and 90° relative to the injection flow direction as illustrated in Figure 5.7. Three repetitions were performed of each material and orientation configuration. A total of 27 uniaxial tensile tests were performed. It should be emphasised that the specimens were cut from a variety of places on the plate. The fibre orientation study presented in Section 5.4 was made with *one* sample cut from left-over material of PP10. Due to the nature of the material flow (e.g. influence of boundaries) during the moulding process, the variation of the fibre orientations across the whole plate may not necessarily be adequately represented by one sample.

5.3.1 Finite element model

The finite element discretisation of the specimen is presented Figure 5.8. A velocity was prescribed to the node set marked with the colour yellow (over the thickness of the specimen) while fixing the node set marked with the colour green. The prescribed velocity was sufficiently low to ensure quasi-static conditions.

The different specimen orientations illustrated in Figure 5.7 were simulated by rotating the local material basis in each element in Abaqus as illustrated in

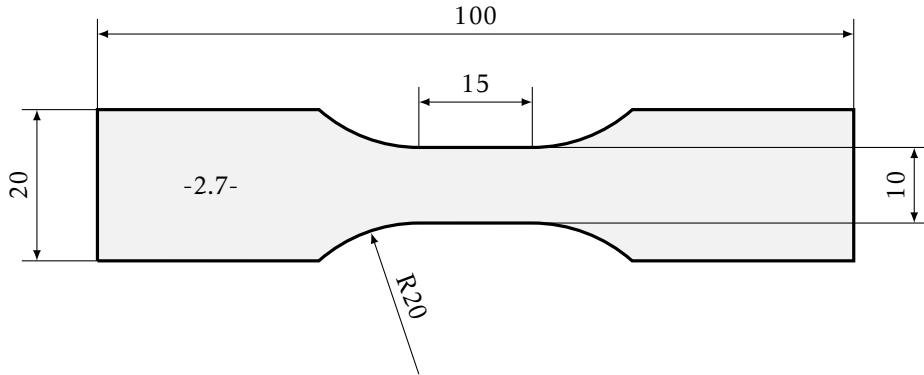


Figure 5.6: Geometry of uniaxial tensile test specimen. Dimensions are in millimetres [mm].

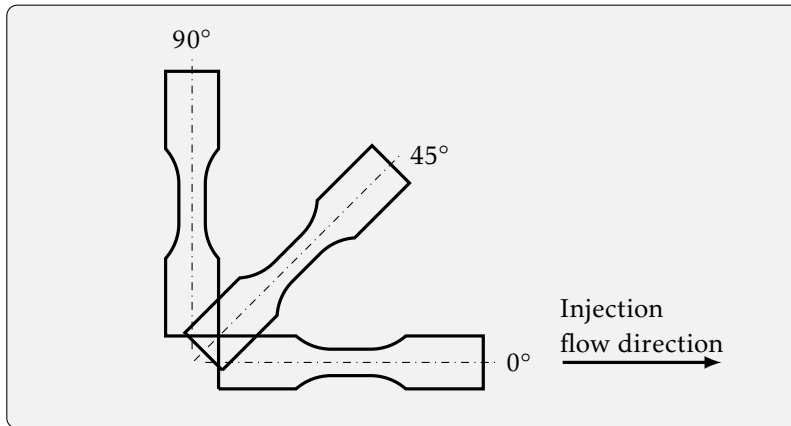


Figure 5.7: Illustration of the three specimen orientations with respect to the injection flow direction. The surrounding box illustrates *one half* of the injection moulded plate from where the specimens were cut from. The dimensions of the illustrated plate and the specimens are proportional, but the position of the specimen outlines do not necessarily represent the position from where they were cut.

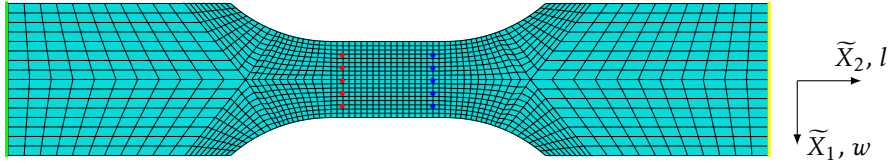


Figure 5.8: The finite element discretisation of the uniaxial tensile test specimen. The model consists of C3D8R-elements (i.e. eight node solid linear element with reduced integration). There are three elements across the thickness of the model. The colour codes in the figure represents node sets relevant to the establishment of state variables during post-processing. The volume between the red and blue nodes are referred to as the *gauge area*.

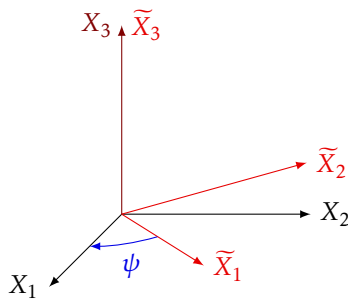


Figure 5.9: Illustration of how the different specimen orientations in Figure 5.7 was modelled by rotating the local material orientation for the elements in the finite element model. \tilde{X}_2 corresponds to the direction of the applied load.

Figure 5.9. The three specimen orientations corresponds to

$$\psi \in \{0^\circ, 45^\circ, 90^\circ\}$$

in the figure. The $X_1X_2X_3$ -system refers to the local material orientation, while the $\tilde{X}_1\tilde{X}_2\tilde{X}_3$ -system corresponds to the global basis of the finite element model.

5.3.1.1 Variable calculation

The single nodes which are marked with blue and red colours are used to measure relative displacement over the gauge area of the specimen in Figure 5.8. In order to replicate the procedure of strain extraction in [11] for PP10 and PP30, the average displacement of all the red nodes, u_{red}^{avg} , were subtracted from the average displacement of the blue nodes, u_{blue}^{avg} , in the direction of the applied load so that

$$\Delta l = u_{blue}^{avg} - u_{red}^{avg} = l_{cur} - l_{ref} \quad \Rightarrow \quad l_{cur} = \Delta l + l_{ref}.$$

From Equation 2.7 and Equation 2.9, true strain can be formulated as

$$\varepsilon = \ln\left(\frac{l_{cur}}{l_{ref}}\right) = \ln\left(1 + \frac{\Delta l}{l_{ref}}\right) \quad \text{where} \quad \varepsilon_{eng} = \frac{\Delta l}{l_{ref}}$$

The distance between the red and blue nodes in the undeformed reference configuration was

$$l_{ref} = 11.84mm.$$

The sum of the reaction forces in \tilde{X}_2 -direction measured across the green node set is denoted F . The cross sectional area of the gauge volume is

$$A_{ref} = 2.7mm \times 10mm = 27mm^2.$$

The *engineering* stress across the gauge area is defined as

$$\sigma_{eng} = \frac{F}{A_{ref}}.$$

Amundsen [11] states that the reinforced polypropylene did not exhibit any significant volume change during testing. The matrix model for the analyses in this chapter is implemented with some volume variation ($\nu_e, \nu_p \neq 0.5$). It was chosen to base the calculation of the true stress on the assumption of isochoric deformation to allow for comparison with the calculations in Amundsen [11]. The relationship between σ_{eng} and the true stress σ then becomes

$$\sigma = \sigma_{eng}(1 + \varepsilon_{eng}).$$

5.4 Fibre orientation distribution mapping

To include quantitative information about the fibre orientations of the material tested in [11] in the SFRM-model, data from a X-ray computed tomography (CT) was analysed. The raw CT data which was used, originated from a scan performed at the RECX laboratory at the Department of Physics at NTNU in June 2014. It was achieved from a sample of PP10 cut from the same plates as the tensile test specimens used in [11]. The raw data was analysed using the *Fiber composite Material Analysis*-plugin to the CT post-processing software *VGStudio MAX*. For more information regarding the software and plugin used in this fibre study, the reader is referred to the developer's website [32]. The objective of this analysis was to quantify the fibre orientation distributions for the injection moulded fibre-reinforced composite. Although a more extensive and structured mapping of the internal structure of the sample could be performed, the produced results gives an indication of the fibre orientation distributions in the injection moulded plate. The trends observed for the fibre distributions will later be applied to the SFRM-model.

5.4.1 Scan of PP10 sample

A column-shaped material sample with a square cross-section was extracted from the same injection moulded plate of PP10 as the tensile test specimens. The sample was scanned with CT. Due to the limited computing resources available, only a smaller volume of the scanned sample was analysed using *VGStudio MAX*. An illustration of the injection moulded plate, the CT scanned material sample, the analysed volume V_0 and the tensile test specimen corresponding to $\psi = 0^\circ$ is displayed in Figure 5.10. The yellow outline in the figure illustrates V_0 . The size of the analysed volume was

$$V_0 = 2.6\text{mm} \times 2.7\text{mm} \times 5.1\text{mm} = 35.8\text{mm}^3. \quad (5.8)$$

The software separates and displays the different phases (or material densities) using gray-scale values. As the glass fibres are denser than the polypropylene, separate gray-scale value ranges are assigned to the two phases. Figure 5.11 presents the visual results from the analysis of V_0 where the gray-scale values corresponding to the density range of the polypropylene material are excluded.

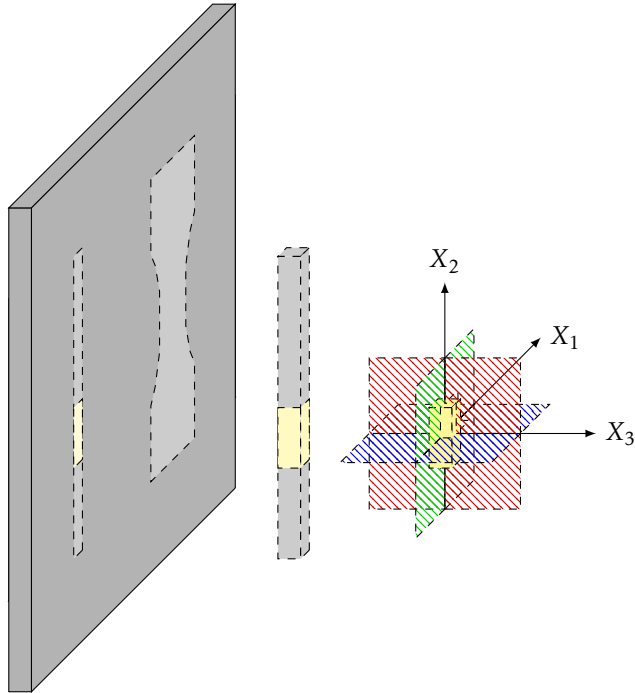


Figure 5.10: Illustration of the injection moulded plate of PP10 which the tensile test specimens and the CT sample were machined from. The illustration is not in proportions to exact *dimensions*, but illustrates the correct *orientations*. X_2 is parallel to injection flow direction. The whole outlined column illustrates the sample scanned with CT, while the yellow outline illustrates a smaller volume analysed in VGStudio MAX.

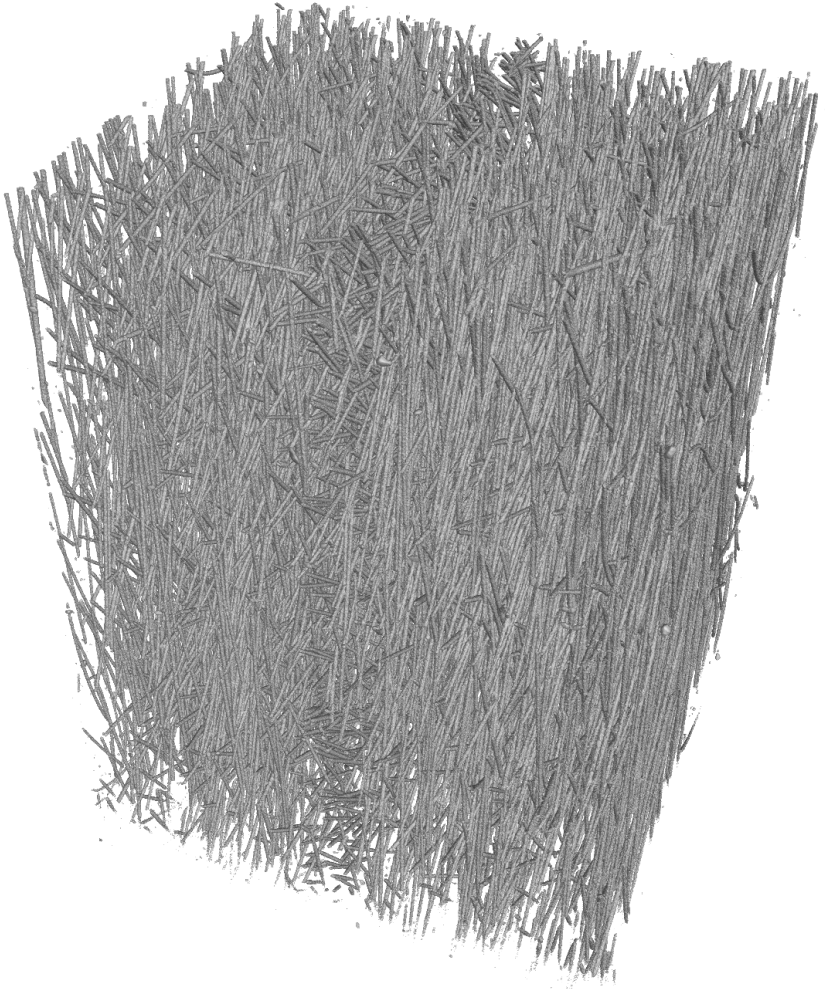


Figure 5.11: Analysis sample from CT scan of PP10. The sample displayed in this figure corresponds to the yellow outline (V_0) in Figure 5.10. The grey-scale values of the matrix material is here excluded leaving only the dispersed fibres. (Screen caption taken in VGStudio MAX)

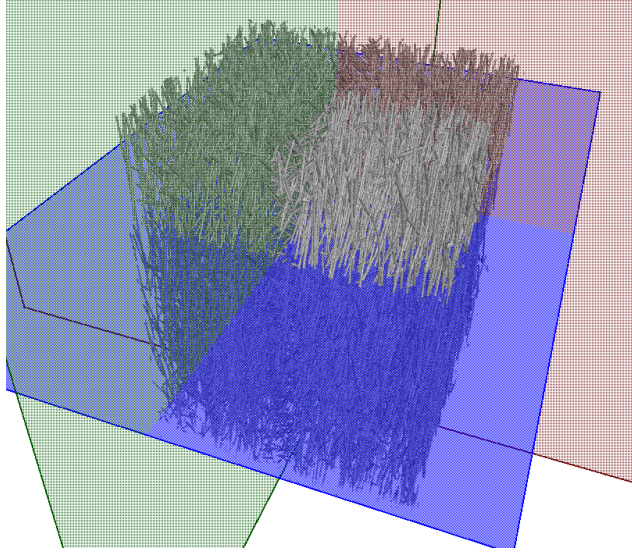


Figure 5.12: Same screen caption as in Figure 5.11, but with colour coded coordinate planes included. The colours of the planes corresponds to illustration in Figure 5.10. (Screen caption taken in VGStudio MAX)

5.4.2 Analysis of PP10 sample

A coordinate system where the origin was placed at the volume center of V_0 was established. The planes of this coordinate system is displayed in Figure 5.12. The coordinate system and the colours of the planes are equivalent to that illustrated in Figure 5.10. In order study the variation in the fibre orientation distributions over the plate thickness, the distributions were sampled from three layers. Three center-planes of the three layers were placed at $X_3^{layer} = \{-0.70, 0.00, 0.70\}$ and with surface normals parallel to the X_3 -axis. The fibres which are included in the layers are illustrated in Figure 5.13. All the layers have thickness $0.20mm$ (i.e. between $X_3^{layer} \pm 0.10mm$).

The results from the fibre analyses of the three layers where the distributions are projected onto coordinate planes, are displayed in Figure 5.14, Figure 5.15

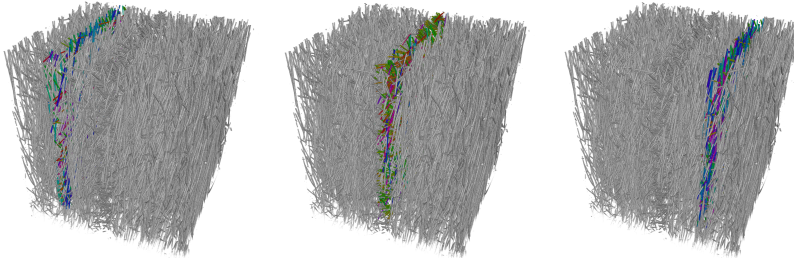


Figure 5.13: Illustration of the layers where the projected fibre orientation distributions were studied. The layers are denoted *lower*, *middle* and *upper layer*. The names correspond to the three figures, starting from the leftmost to the far-right figure, respectively. (Screen captions taken in VGStudio MAX)

and Figure 5.16. The vertical axes are displayed without a measure of unit, but the total area under the graphs equals one in order to represent the whole distribution. Each figure presents the projected fibre orientation distributions for the three layers, projected onto the planes stated in the lower right corners. These planes corresponds with what was illustrated in Figure 5.10.

Clear orientation trends can be observed in Figure 5.14 and Figure 5.16. β has a larger deviation from its distribution peak than the variations of α and γ , and there is an observable difference in shape of the distributions between the three layers in Figure 5.15. The fibre orientations seem to be more random in the X_1X_2 -plane, but based on the two other projections, the majority of the fibres seem to lay in this plane. This planar orientation is consistent with what presented by Singh and Kamal [33]. Based on these findings, the fibre orientation distributions applied to the succeeding analyses will have an expected orientation parallel to the injection flow direction (i.e. X_2 -axis) and in the X_1X_2 -plane. Multiple configurations for the user-defined fibre distributions corresponding to the cases 1 and 2 in Table 3.1 in the defined coordinate system in Figure 5.10, will be used.

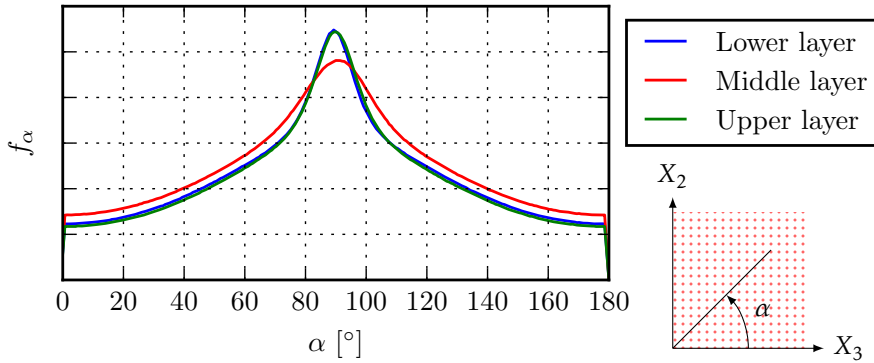


Figure 5.14: The distribution of fibre orientations projected onto the X_2X_3 -plane. The projected fibre orientations are given by the angle α as defined in the figure.

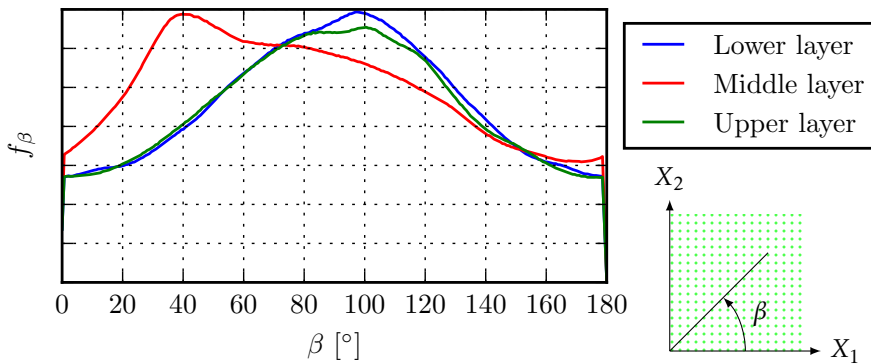


Figure 5.15: The distribution of fibre orientations projected onto the X_1X_2 -plane. The projected fibre orientations are given by the angle β as defined in the figure.

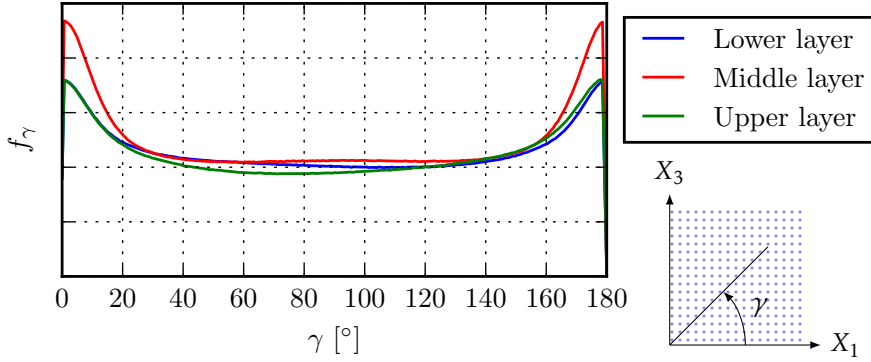


Figure 5.16: The distribution of fibre orientations projected onto the X_1X_3 -plane. The projected fibre orientations are given by the angle γ as defined in the figure.

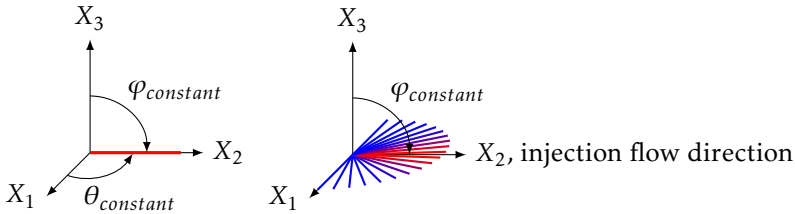


Figure 5.17: Illustration of the two fibre configurations used with the SFRM-model in Section 5.5. The left figure models the situation where the whole fibre phase is aligned in the injection flow direction while the right figure shows a normally distributed weighting over a group discretisation of $\theta \in [0^\circ, 180^\circ)$. Red to blue colour variation illustrates decreasing group weighting.

5.5 Comparison with experimental results

This section presents the comparison of the results produced by the calibrated SFRM-model with the corresponding uniaxial tensile tests in [11]. The matrix model is analysed and compared to the results of unreinforced polypropylene

in [11] as a means of validating the matrix implementation with the calibrated parameters.

For the two materials of fibre-reinforced polypropylene, PP10 and PP30, two fibre configurations are examined using two of the fibre distribution cases which are implemented in the SFRM-model (Case 1 and Case 2). In the analyses related to the different fibre configurations, the matrix model parameters will remain the same (Table 5.3). The analyses where a range of values for a single fibre parameter is studied are grouped into *analysis sets*. The following configurations are used:

- A configuration where the whole fibre phase is aligned with X_2 is examined using fibre distribution Case 1. This configuration is used with $\psi = 0^\circ, 45^\circ$ and 90° .
- A configuration where the fibre phase is oriented according to a normal distribution in the X_1X_2 -plane using fibre distribution Case 2. The expected value of the distribution is parallel to the X_2 -axis, while a range of standard deviations is studied in an analysis set. Analyses sets with this configuration is presented for $\psi = 0^\circ, 45^\circ$ and 90° .

These fibre configurations are illustrated in Figure 5.17. The comparisons will be made for both PP10 and PP30 in order to study the effect of fibre volume content. The user-defined fibre parameters are presented for each configuration for each material using the convention established in Section 3.5. The Young's modulus for the glass fibres will be the same as in Chapter 4 (i.e. $E_f = 72$ GPa).

A clarification: *Experimental test scatter*

Representative graphs from the experimental uniaxial tensile tests made with the fibre-reinforced composites presented by Amundsen [11] will be used in the succeeding comparison. Amundsen [11] performed three repetitions for each material and orientation, which produced some scatter in the results related to PP10 and PP30. The graphs which are stated to be retrieved from [11] are the respective representatives, presented by Amundsen [11], for each material. However, the results from the uniaxial tensile tests made with PP yielded very little scatter.

5.5.1 PP

The matrix implementation with the user-defined parameters from Table 5.3 was compared to the retrieved graph in Figure 5.1. The true stress and strain were computed differently from what was presented in Section 5.3.1.1. Unlike PP10 and PP30, PP experienced necking during testing. By following the methodology of Amundsen [11], the average strain components, ε_l and ε_w , were sampled directly from the elements across the necking region. Amundsen [11] also argues that PP experience non-isochoric flow so the true stress is therefore computed by

$$\sigma = \sigma_{eng} e^{-2\varepsilon_w}.$$

The results are compared in Figure 5.18. The red dashed outline shows a good correspondence at strains lower than 0.05 which is the magnitude for the global strains seen in the tensile experiments related to PP10 and PP30. The local strains may reach a higher level than the global strains for the reinforced polypropylene. An modification of the implemented strain hardening relation may be considered in the future as the current implementation for the evolution of the flow stress may not give an optimal fit at higher levels of strains. The current implementation with the stated matrix parameters will be used to model the matrix phase in the following sections.

5.5.2 PP10

A sample of PP10 was scanned using X-ray CT and analysed in Section 5.4. It was observed that the fibre phase has a tendency to be oriented in the injec-

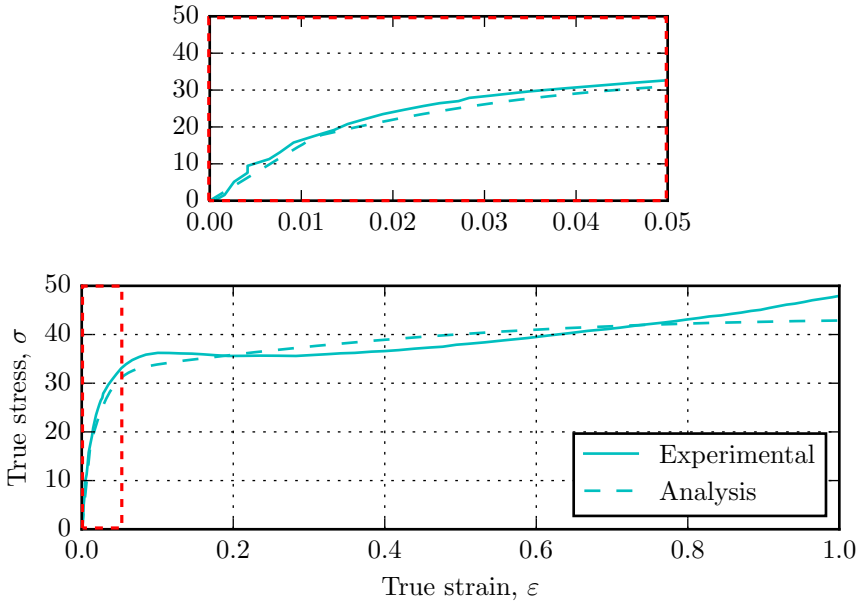


Figure 5.18: Results from the uniaxial tensile test of PP from [11] compared with the matrix model using the calibrated matrix parameter stated in Table 5.3. The red outline illustrates the results at lower strain values which are at the magnitude relevant for the global strains level of PP10 and PP30. The unit of measure for the vertical axis is MPa.

tion flow direction and distributed mainly in the X_1X_2 -plane. In this section, multiple fibre orientation distributions will be examined and compared to the experimental results found in [11] for PP10. The two different fibre configurations were studied for all value of ψ . The first applies the SFRM-model with totally aligned fibres parallel to X_2 (using Case 1) while the second configuration uses a normally distributed orientation of fibres with a variety of standard deviation values, but with a constant expected orientation parallel to X_2 (using Case 2).

5.5.2.1 Aligned fibre orientations

Table 5.4 contains the parameters for the applied with Case 1 in order to simulate a fully aligned fibre phase. The fibres are represented with one group parallel to X_2 (i.e. $\theta = 90^\circ$ and $\varphi = 90^\circ$). The results for all ψ are presented in Figure 5.19. The dashed lines in the figures displays the results from the analyses made with the SFRM-model while the full drawn lines corresponds to equivalent experimental results presented in [11]. The colours of the graphs corresponds to the same specimen orientation. It is seen that for $\psi = 0^\circ$, the SFRM-model overestimates the stress, while underestimating for the ψ equal to 45° to 90° . It is also observed that the result at $\psi = 45^\circ$ falls below that of $\psi = 0^\circ$. This is seen to be caused by the fibres constraining the analysis for $\psi = 90^\circ$ from transverse contraction and in that way providing a stiffness contribution. For $\psi = 45^\circ$, the developing stress state will have significant shear components due to the stress introduced by the fibre.

In Figure 5.20, contour plots of the axial stress in the load direction for PP, PP10 at $\psi = 0^\circ$, PP10 at $\psi = 45^\circ$ and PP10 at $\psi = 90^\circ$, is presented from the top down, respectively. The effects of the fibres are especially visible at $\psi = 45^\circ$ where a clear shear pattern emerges.

In Figure 5.19, the analysis results for $\psi = 0^\circ$ ends at around $\varepsilon = 0.029$. An instability occurs when introducing the fibres. The instability, which causes the analysis to abort, is prominent for the other values of ψ , but at a higher global strain. It is observed to occur in areas where the difference in strain across the elements are large.

Table 5.4: Fibre parameters applied in Section 5.5.2.1.

V_f	E_f [GPa]	Groups	Case	$\theta_{constant}$	$\varphi_{constant}$
0.038	72.0	1	1	90°	90°

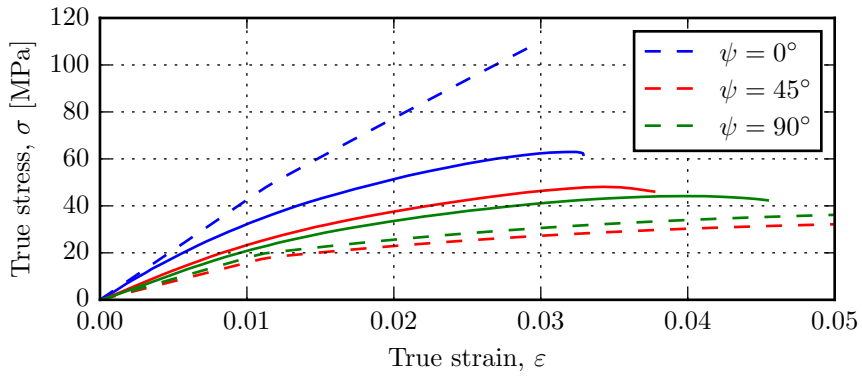


Figure 5.19: Results from the aligned fibre configuration for all ψ for PP10. The colours of the dashed lines corresponds to the colours of the full drawn graphs which is the experimental data from [11]. The applied fibre parameters are stated in Table 5.4.

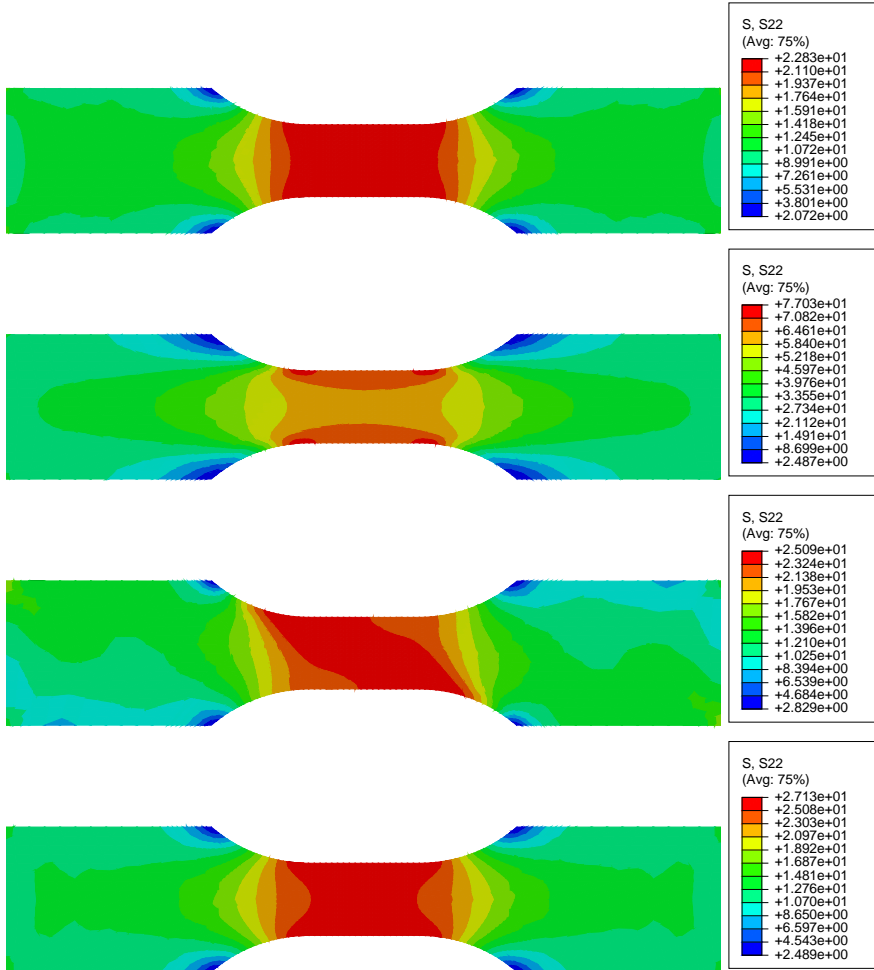


Figure 5.20: Contour plots for variation of the axial stress component in X_2 corresponding to a global displacement of 1.11 mm for aligned fibres. From top to bottom: Unreinforced PP, PP10 at $\psi = 0^\circ$, PP10 at $\psi = 45^\circ$, and PP10 at $\psi = 90^\circ$.

Table 5.5: Fibre parameters applied in Section 5.5.2.2.

V_f	E_f [GPa]	Groups	Case	$\varphi_{constant}$	θ_μ	θ_σ	a_θ
0.038	72.0	16	2	90°	90°	{10°, 20°, 30°, 40°, 50°, 60°}	$\frac{90^\circ}{\theta_\sigma}$

5.5.2.2 Distributed fibre orientations

Table 5.5 contains the parameters related to the fibre implementation of SFRM-model for the analysis sets in this section. Case 2 in Table 3.1 is applied to distributed the fibre phase. A set of standard deviations for the normal distribution of θ is studied for all ψ . This set is presented in Table 5.5 under θ_σ and the expected value for the distribution is stated under θ_μ . It is reminded that a_θ governs the upper and lower limit of the domain for θ as presented in Chapter 3. The domain for θ is $[0^\circ, 180^\circ)$, so a_θ becomes a function of θ_σ . An increase in θ_σ increases the weights of the fibre groups with large X_1 -components while decreasing the weights of the fibre groups with large X_2 -components. Figure 5.21 presents the results for $\psi = 0^\circ$. The effect of increasing the standard deviation of the normal distribution is obvious. For an increase in standard deviation, a decrease in the true stress is seen for $\psi = 0^\circ$. However, as seen in Figure 5.22 and Figure 5.23, the true stresses increase with an increase in standard deviation for $\psi = 45^\circ$ and $\psi = 90^\circ$.

The SFRM-model yields a fairly linear response while the experiments are seen to deflect as the specimen is strained beyond certain strain values for all the different values of ψ . Fibre-reinforced materials experience failure mechanisms such as fibre breakage, matrix cracking and decohesion in the interface between the fibres and surrounding matrix [34]. It not unlikely that the experimental tensile tests are experiencing the mentioned damage phenomena which the current implementation of the SFRM-model does not account for. Good correspondence in all three comparisons are seen for low strain values, however, at different values of θ_σ .

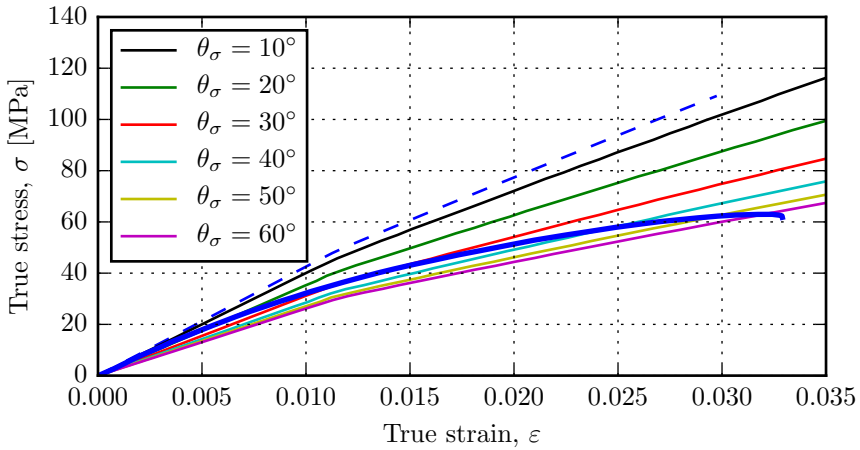


Figure 5.21: Results from the normally distributed configuration studied over a range of standard deviations for $\psi = 0^\circ$ for PP10. The blue full drawn graph and the blue dashed graph correspond to the graphs of same colour in Figure 5.19. The applied fibre parameters are stated in Table 5.5.

5.5.3 PP30

Although the mapping of the fibre orientations presented in Section 5.4 was made using a sample of PP10, the same fibre distributions were used to analyse PP30. The difference in fibre content for PP30 compared to PP10, may have an influence on the orientations of the fibres. This means that the same distributions seen in Section 5.4 may not apply for the fibre phase in PP30. In order to observe the effects of the increase in volume fraction, the same analysis sets presented in Section 5.5.2 are also studied in this section. According to Table 5.2, the volume fraction of the fibre phase in PP30 is

$$v_f = 0.134.$$

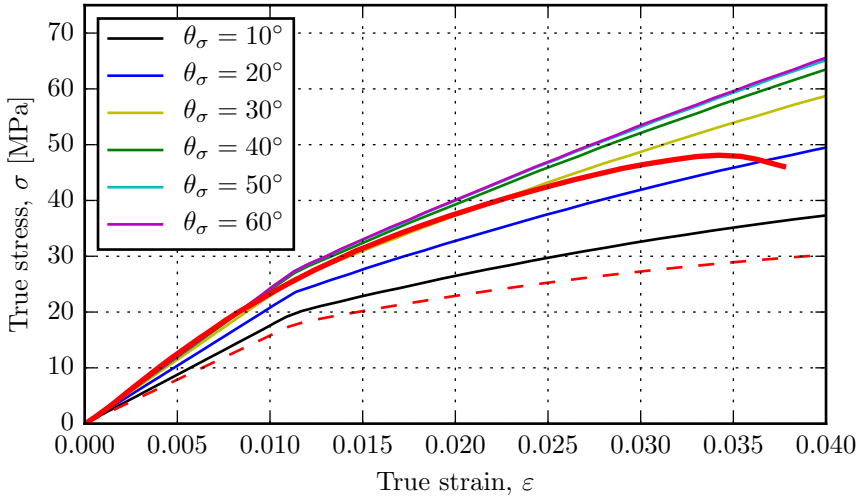


Figure 5.22: Results from the normally distributed configuration studied over a range of standard deviations for $\psi = 45^\circ$ for PP10. The red full drawn graph and the red dashed graph correspond to the graphs of same colour in Figure 5.19. The applied fibre parameters are stated in Table 5.5.

5.5.3.1 Aligned fibre orientations

The current fibre parameters for this section are stated in Table 5.6. The results produced by the SFRM-model with aligned fibres and the experimental graphs for PP30, are given in Figure 5.24. The figure gives the same tendencies as for PP10, but the increase in v_f is seen to produce a major increase in stress for $\psi = 0^\circ$. For $\psi = 45^\circ$ and $\psi = 90^\circ$, this increase is minor. This increase in stress levels is also observed in the experimental data. The instability observed for PP10 is also observed in the analyses for PP30.

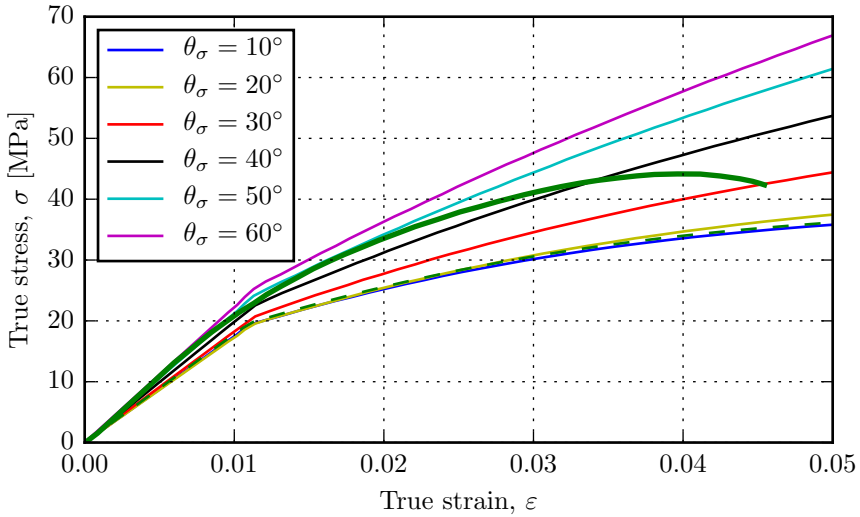


Figure 5.23: Results from the normally distributed configuration studied over a range of standard deviations for $\psi = 90^\circ$ for PP10. The green full drawn graph and the green dashed graph correspond to the graphs of same colour in Figure 5.19. The applied fibre parameters are stated in Table 5.5.

Table 5.6: Fibre parameters applied in Section 5.5.3.1.

V_f	E_f [GPa]	Groups	Case	$\theta_{constant}$	$\varphi_{constant}$
0.134	72.0	1	1	90°	90°

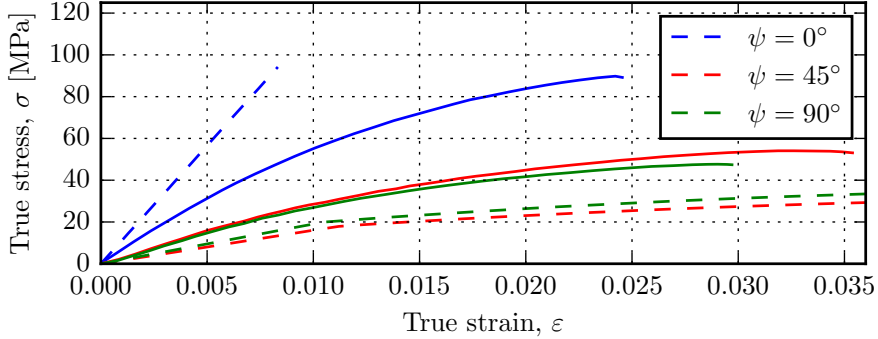


Figure 5.24: Results from the aligned fibre configuration for all ψ for PP30. The colours of the dashed lines corresponds to the colours of the full drawn graphs which is the experimental data from [11]. The applied fibre parameters are stated in Table 5.6.

Table 5.7: Fibre parameters applied in Section 5.5.3.2.

V_f	E_f [GPa]	Groups	Case	$\varphi_{constant}$	θ_μ	θ_σ	a_θ
0.134	72.0	16	2	90°	90°	{10°, 20°, 30°, 40°, 50°, 60°}	$\frac{90^\circ}{\theta_\sigma}$

5.5.3.2 Distributed fibre orientations

The fibre parameters used for this configuration are stated in Table 5.7. The results of the SFRM-model applied to PP30 for $\psi = 0^\circ$, 45° and 90° are presented in Figure 5.25, 5.26 and 5.27, respectively. As the fibre content increases with a distributed fibre phase, the influence of fibre phase becomes greater. Changing θ_σ is seen to generally have a greater effect on the axial stress compared to what seen for equivalent analyses for PP10.

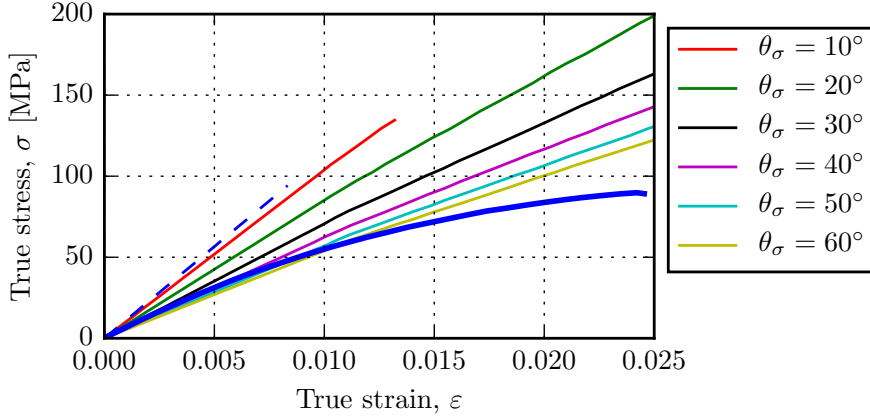


Figure 5.25: Results from the normally distributed configuration studied over a range of standard deviations for $\psi = 0^\circ$ for PP30. The blue full drawn graph and the blue dashed graph correspond to the graphs of same colour in Figure 5.24. The applied fibre parameters are stated in Table 5.7.

5.6 Evaluation of validation

From the comparisons made in this chapter, it is seen that the introduction of fibres to the neat matrix model has a significant impact on the total mechanical behaviour. The most important observations made were:

- An increase in fibre volume content yielded a stiffer response. This was more prominent for the configurations where the fibre phase was mostly oriented in the direction of loading.
- The configurations where the fibre phase was modelled as fully aligned produced either an over- or underestimation in tensile response depending on the value of ψ with respect to the corresponding experimental results from Amundsen [11]. However, a planar distribution of the fibre phase was observed in the CT analysis of PP10, and distributed fibre representations are also seen to coincide better with the compared ex-

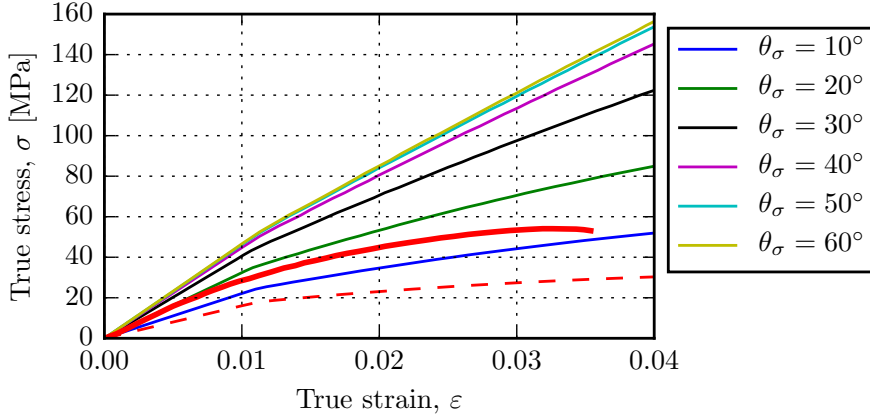


Figure 5.26: Results from the normally distributed configuration studied over a range of standard deviations for $\psi = 45^\circ$ for PP30. The red full drawn graph and the red dashed graph correspond to the graphs of same colour in Figure 5.24. The applied fibre parameters are stated in Table 5.7.

perimental data.

- The effects of varying the standard deviation in the planar normal distributions for the fibre phase was evident. An increase in standard deviation yields a lower tensile stress in the case of $\psi = 0^\circ$ while contributes to a higher tensile stress response for the other two values of ψ .
- Higher stress levels were observed for $\psi = 90^\circ$ compared to that of $\psi = 45^\circ$ for the fully aligned fibre configuration. Although the fibre representation in $\psi = 45^\circ$ has a larger directional component in the tensile direction, the fibre in $\psi = 90^\circ$ seem to have a greater impact on the tensile response in the analyses. It is seen that in the aligned analyses for PP10 and PP30 for $\psi = 90^\circ$, the specimen is constrained from transverse contraction.
- A pattern of occurring instabilities are observed in the majority of the analyses performed with the SFRM-model. The instability produces ex-

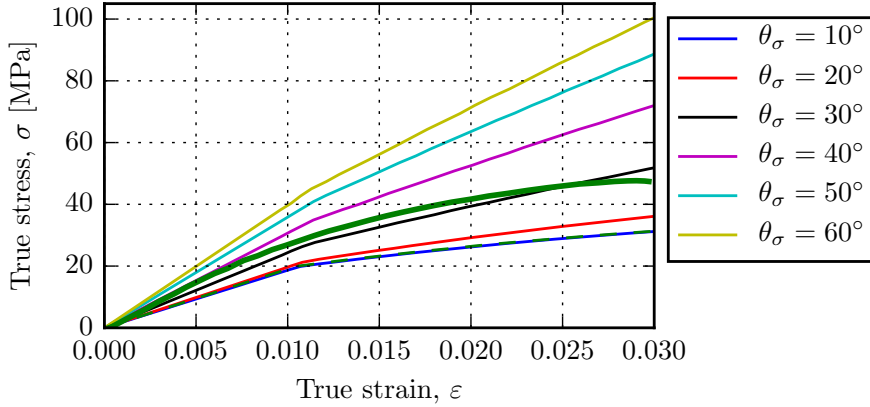


Figure 5.27: Results from the normally distributed configuration studied over a range of standard deviations for $\psi = 90^\circ$ for PP30. The green full drawn graph and the green dashed graph correspond to the graphs of same colour in Figure 5.24. The applied fibre parameters are stated in Table 5.7.

cessive element deformation which causes the analysis to abort. Through visual inspections of deformation plots, the starting point of the instability seems to be traced back to areas with large strain gradients. The observed instabilities seem to occur in the analyses where the stress in the fibres are high, as for $\psi = 0^\circ$ in to comparison of PP10 and PP30.

- As the tensile specimens are strained, progressive loss of stiffness are seen the experimental tensile test results from Amundsen [11]. Figure 5.28 presents the change in tangent stiffness for $\psi = 0^\circ$ for PP10 as an example. The degree of non-linearity is not replicated well with the current implementation of the SFRM-model. Although a noticeable change in tangent stiffness is observed as plasticity starts to dominate the global response of the matrix model, the linear constitutive mechanical behaviour of the fibres seems to dominate the total response. Karger-Kocsis et al. [35] and Barré and Benzeggagh [36] investigated the development of different damage mechanisms in fibre-reinforced

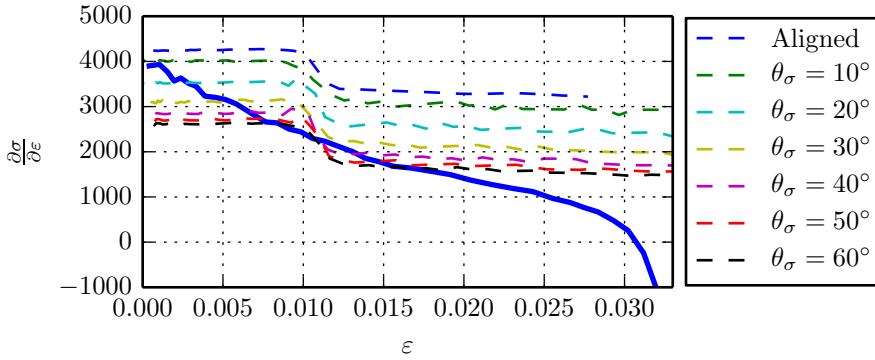


Figure 5.28: $\frac{\partial \sigma}{\partial \varepsilon}$ versus ε for $\psi = 0^\circ$ for PP10. Both aligned and distributed fibre representations are presented. The blue full drawn graph is the corresponding experimental tensile results from Amundsen [11].

polypropylene by recording the acoustic signals emitted during various tests. The occurrences of these signals are associated with increasing levels of damage in the material [36]. It was observed that the accumulation of acoustic signals started at early stages and had an increasing growth rate as testing progressed. This has a great impact on modelling of such materials. As damage phenomena are present from early stages of deformation, they should also be included in the modelling. Damage modelling is not implemented in neither the matrix model nor the fibre definition of the current version of the SFRM-model.

Chapter 6

Conclusion

This thesis presents the foundation, implementation, verification and validation of a two-phase constitutive relation for the mechanical behaviour of short fibre-reinforced materials which is very similar to the model presented by Notta-Cuvier et al. [7]. By combining the weighted contributions of both the matrix phase and the orientation distribution of the fibre phase, a potent method for calculating the total mechanical response was established.

The mathematical framework was established and presented via an illustrative and intuitive approach while still firmly grounded in the presented theory. The presentation was enriched with illustrations, examples and chronological procedures that represents important aspects of the model. A pseudo formulation of the mathematical equations was then presented in order to easier get an understanding of the source code implementation.

The source code implementation in FORTRAN was then created based on this framework. A modularised subroutine structure was strived in order to form a computational effective and generic model compatible with different matrix models and fibre distribution configurations. A set of predefined fibre distribution schemes was also implemented in order to represent the plausible distributions of the fibre orientations found in fabricated short fibre-reinforced materials.

A thorough verification was then conducted where the implementation was controlled and evaluated. Known solutions and models, such as the model

by Notta-Cuvier et al. [7], were used as comparisons to equivalent results produced by the SFRM-model. The verification process yielded reasonable results, but with some minor discrepancies. The observed discrepancies were reasoned to not be associated with the implemented model presented herein. The SFRM-model was therefore deemed as functioning.

As the established constitutive model was working properly according to the mathematical foundation, a validation was performed in order to study the validity of the mathematical foundation. The SFRM-model was calibrated and compared to the results from experimental uniaxial tensile tests conducted by Anne Amundsen [11]. Three injection molded materials in the form of plates, were examined by Amundsen. The material were unreinforced polypropylene (PP), fibre-reinforced polypropylene with 10% fibre weight content (PP10) and fibre-reinforced polypropylene with 30% fibre weight content (PP30). The matrix module of the SFRM-model was adapted and validated using the unreinforced polypropylene. The results yielded by the validation of the matrix was acceptable, but more advanced plasticity models may be considered in the future.

Raw data from a previously performed X-ray computed tomography of a PP10-sample was analysed in order to quantify the fibre orientation distributions within the material. The fibres were found to be mostly distributed in the plate plane. The SFRM-model was therefore applied to multiple analysis sets where the planar distribution of fibres were studied. Configurations for completely aligned and normally distributed fibre orientations were applied for both PP10 and PP30. Interesting observations were made during the validation process which shed light on different behavioural aspects of the current SFRM-model, such as:

- A general increase in stress levels were caused by an increase in fibre volume content.
- A variation in fibre orientation distribution had a significant impact on results. A distributed fibre phase had generally a better correspondence with experimental tests than a fully aligned fibre representation.

The SFRM-model developed in this thesis is seen to be a potent framework which models the behaviour of fibre-reinforced composites in a satisfying manner for low levels of strain.

A possible need for modelling progressive damage in both the matrix and the fibres were seen in order replicate damage mechanisms seen in fibre-reinforced composites. Such features are already implemented in the model by Notta-Cuvier et al. [8, 9, 10]. The constitutive relation of the fibres may also need to be re-evaluated to more accurately reproduce the behaviour of fibre-reinforced materials. This is further discussed in Chapter 7.

Chapter 7

Future work

As the development of the model herein was limited by time, some concerns and ideas still remain unresolved and unexplored. This chapter presents some concrete suggestions to future activities related to the SFRM-model.

7.1 Failure modes

In Chapter 5, it was observed that the SFRM-model tend to produce a linear response for uniaxial tension tests while equivalent experiments shows a decrease in tangent stiffness. Failure modes such as fracture in the reinforcing fibres, and decohesion of the interface between the fibre and matrix phase are yet to be accounted for in the SFRM-model. An implementation of these phenomena may contributed to give a more realistic global response as strains develop [37, 34, 38, 39, 40]. Notta-Cuvier et al. have already implemented phase decohesion in [10] with seemingly good results.

Fracture in the fibres may be implemented via a simple strain energy based fracture criterion, such as

$$U \geq U_{max} \quad \text{where} \quad U = \int_0^{\varepsilon_f} \sigma_f d\varepsilon_f = \frac{1}{2} E_f \varepsilon_f^2$$

for linear elastic fibres. If the strain energy in the representative for a fibre group i , U^i , exceeds the critical U_{max} , all the fibres in the group may be thought of as fractured, and unable to bear any future loading.

Decohesion of the interface between the fibre and matrix phase (also known as fibre pull-out) may be implemented based on the notion of an interfacial shear strength τ_{max} which governs the interface's ability to transfer the load between the matrix and fibre phase. A possible criterion for modelling the pull-out phenomenon may, for example, be based on the shear components of $\bar{\sigma}_m$. If the established criterion is exceeded, the fibres in group i may be considered decohered from the matrix phase, and unable to bear any future loading.

Independent of the failure mode, the fibres in group i will still take up a portion of the volume which is represented by the relation

$$W_f^i v_f.$$

If a failure criterion is exceeded, the one-dimensional fibre stress σ_f^i could be thought to take on the value of $\bar{\sigma}_{11,m}$ or simply be put equal to zero.

7.2 Constitutive modelling of fibre phase

In the current implementation of the SFRM-model, the fibres' mechanical behavior is assumed to be linear elastic with the same properties in both compression and tension. It may be reasonable to assume that the fibres may experience buckling when subjected to compression. Figure 7.1 illustrates the current and possible future implementations where the fibres' possible lack of load bearing capabilities in compression, are accounted for. The left most figure illustrates Equation 7.1 which is the current implementation where the mechanical response is linear in both compression and tension according to the slope E_f .

$$\sigma_f = E_f \varepsilon_f \quad \forall \quad \varepsilon_f \quad (7.1)$$

Equation 7.2 is illustrated by the middle figure of Figure 7.1. The possible constitutive relation suggests that the fibres are unable to bear *any* compressive stress.

$$\sigma_f = \begin{cases} E_f \varepsilon_f & \text{if } \varepsilon_f > 0 \\ 0 & \text{if } \varepsilon_f \leq 0 \end{cases} \quad (7.2)$$

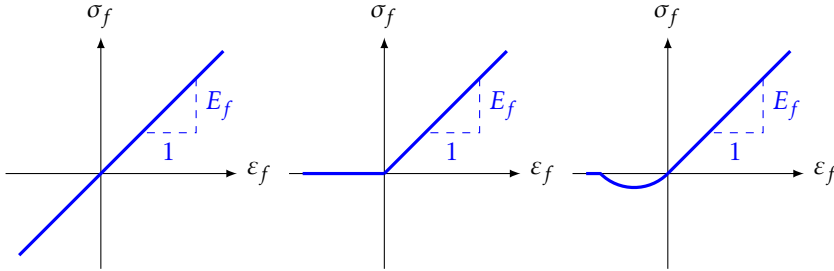


Figure 7.1: Illustration of constitutive relation for the fibres. The figures illustrates, from left to right, Equation 7.1, Equation 7.2 and Equation 7.3, respectively.

The figure on the right illustrates the relation expressed in Equation 7.3 where the fibres are allowed to take some compressive stress.

$$\sigma_f = \begin{cases} E_f \varepsilon_f & \text{if } \varepsilon_f > 0 \\ F(\varepsilon_f) & \text{if } \varepsilon_f \leq 0 \end{cases} \quad (7.3)$$

An explicit definition of $F(\varepsilon_f)$ is not suggested herein, but may for example take the shape of the rightmost illustration in Figure 7.1.

7.3 Including other fibre properties

Apart from orientation which is described by an orientational vector, every single fibre may have an individual set of properties such as length, thickness, fracture strength, interfacial shear strength, etc. Some of these properties may have an influence on the total mechanical response of the short fibre reinforced material [[41], [42], [34], [43], [44], [19]]. These properties may follow a certain distribution or assume a constant value.

The method of grouping fibre orientation and weighting the groups based on the amount of members they hold, can be extended to include other fibre properties as well. For example, if the fibre orientation is given in spherical coordinates, two variables are sufficient to represent fibre orientation (θ and

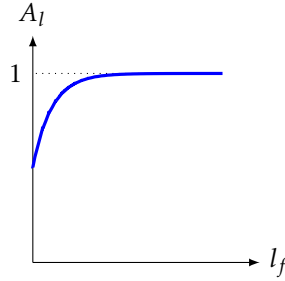


Figure 7.2: Possible relationship between the fibre length efficiency scaling factor A_l and fibre length l_f .

φ). These two variables are used to establish N_f^i which in turn is used to establish σ_f^i . The variations in both θ and φ are according to a given distribution. The domain for these two variables are $[0^\circ, 180^\circ]$ which is discretised into k_φ and k_θ number of groups for φ and θ , respectively. This alone produces a total of k groups where $k = k_\varphi k_\theta$.

Continuing, the fibre length l_f has also a given distribution, and discretised into k_l groups. Since l_f does not have a constitutive influence on σ_f^i , a scaling is suggested. As presented in Section 2.2.2, the strength of the composite material increases with fibre length. Miwa and Horiba [18] study the effect of fibre length in epoxy resin reinforced with short glass and carbon fibres. A typical relation looks something like the shape in Figure 7.2, but the tensile strength has been replaced with a scaling factor A_l . A_l is a function of l_f , and may range below and above factor 1.

$$\sigma_f = \sum_{i=1}^k \sigma_f^i W_f^i A_l(l_f^i)$$

The total number of groups for this extended case, is

$$k = \prod_{prop} k_{prop} = k_\varphi k_\theta k_l$$

The product $W_f^i A_l(l_f^i)$ may be thought of as the effective weight for the fibre

group, and

$$\sum_{i=1}^k W_f^i A_l(l_f^i) \neq 1$$

The notion of introducing factors that governs the fibre's efficiency in a modified rule of mixtures is not unlike what presented in [2, 17, 34, 37].

7.4 Development of fibre distribution cases

The currently implemented fibre distribution cases presented in Table 3.1, may not necessarily be suited to represent all distributions found within a fibre-reinforced material. Apart from the Monte Carlo case, the fibre distribution cases can be viewed as performing two jobs: the discretisation of the fibre groups into directional vectors, and the weighting of each individual group. In the event of fully random three-dimensional orientation of the fibres, a problem with the current Case 4 will emerge. The discretisation of the fibre phase is currently made by discretising the domains for φ and θ into, respectively, k_φ and k_θ number of points. The total number of discretisation points which represents each fibre group's orientation, will then be

$$k = k_\varphi k_\theta.$$

For every value of φ , the domain of θ will be represented by k_θ number of points. This three-dimensional discretisation is applied with $k_\theta = k_\varphi$ in Case 4. In Figure 7.3, the group discretisation applied in Case 4 is illustrated with $k = 36$. This uniform discretisation scheme in θ and φ , i.e. the left figure of Figure 7.3, will not produce a uniform discretisation of the direction vectors as seen in to the right in the Figure 7.3. If an uniform weighting distribution is applied, all the fibre groups are weighted equal so that

$$W_f^i = \frac{1}{k}.$$

This will produce a non-uniform discretisation as the density of groups is higher for φ values close to 0° and 180° . The need for a uniform group discretisation is therefore evident and is suggested in future development of the model.

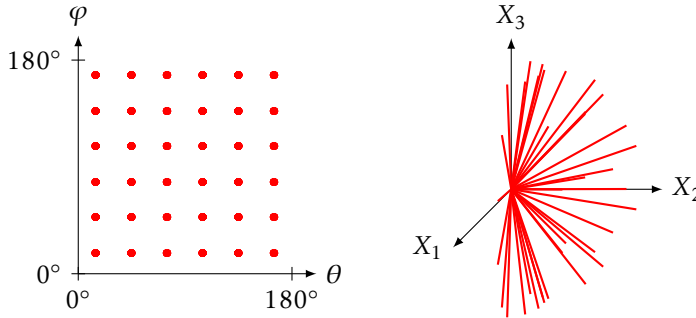


Figure 7.3: Illustration of the discretisation of the groups direction vector as it is done in Case 4 for $k_\theta = k_\varphi = 6 \Rightarrow k = 36$.

7.5 Further exploration

Future exploration of aspects related to the SFRM-model should be performed. Some suggestions for future activities follows in the list below:

- Amundsen [11] used a brittle polymer model made at SIMLab at NTNU to analyse the experimental data in the thesis. The performance of this model could be compared to that of the SFRM-model.
- Amundsen also conducted experiments with bending and plates with a centric hole to which the SFRM-model could be applied and studied.
- A more advanced rate-dependent matrix model could be integrated with the SFRM-model to better model the matrix phase.
- A difference between the distributions over the thickness of an injection molded plate is observed. A material sectioning in the finite element model where different fibre distributions are used, may be considered.
- A thorough study of Case 5 which is the Monte Carlo distribution of discrete fibres. The distribution scheme is interesting as it does not directly homogenise the fibre phase into groups. This case may be able to represent the scatter which is often seen in composites' mechanical properties.

Bibliography

- [1] A. Kelly and W.R. Tyson. Tensile properties of fibre-reinforced metals: Copper/tungsten and copper/molybdenum. *Journal of the Mechanics and Physics of Solids*, 13(6):329 – 350, 1965.
- [2] W.H. Bowyer and M.G. Bader. On the re-inforcement of thermoplastics by imperfectly aligned discontinuous fibres. *Journal of Materials Science*, 7(11):1315–1321, 1972.
- [3] I. Doghri and L. Tinel. Micromechanical modeling and computation of elasto-plastic materials reinforced with distributed-orientation fibers. *International Journal of Plasticity*, 21(10):1919 – 1940, 2005.
- [4] S. Kammoun, I. Doghri, L. Adam, G. Robert, and L. Delannay. First pseudo-grain failure model for inelastic composites with misaligned short fibers. *Composites Part A: Applied Science and Manufacturing*, 42(12):1892 – 1902, 2011.
- [5] B. Nedjar. An anisotropic viscoelastic fibrematrix model at finite strains: Continuum formulation and computational aspects. *Computer Methods in Applied Mechanics and Engineering*, 196(912):1745 – 1756, 2007.
- [6] S. Klinkel, C. Sansour, and W. Wagner. An anisotropic fibre-matrix material model at finite elastic-plastic strains. *Computational Mechanics*, 35(6):409–417, 2005.
- [7] D. Notta-Cuvier, F. Lauro, B. Bennani, and R. Balieu. An efficient modelling of inelastic composites with misaligned short fibres. *International Journal of Solids and Structures*, 50(19):2857 – 2871, 2013.

- [8] D. Notta-Cuvier, F. Lauro, B. Bennani, and R. Balieu. Damage of short-fibre reinforced materials with anisotropy induced by complex fibres orientations. *Mechanics of Materials*, 68(0):193 – 206, 2014.
- [9] D. Notta-Cuvier, F. Lauro, and B. Bennani. An original approach for mechanical modelling of short-fibre reinforced composites with complex distributions of fibre orientation. *Composites Part A: Applied Science and Manufacturing*, 62(0):60 – 66, 2014.
- [10] D. Notta-Cuvier, F. Lauro, and B. Bennani. Modelling of progressive fibre/matrix debonding in short-fibre reinforced composites up to failure. *International Journal of Solids and Structures*, 66(0):140 – 150, 2015.
- [11] A.H. Amundsen. Behaviour and modelling of fibre-reinforced polymers. Master's thesis, Norwegian University of Science and Technology, 2014.
- [12] O.S. Hopperstad and T. Børvik. *TKT4135 Materials mechanics - Lecture Notes, Part 1*. Department of Structural Engineering, 2013.
- [13] Fridtjov Irgens. *Continuum Mechanics*. Springer, 2008 edition, 3 2008.
- [14] William D. Callister and David G. Rethwisch. *Materials Science and Engineering*. John Wiley & Sons Ltd, 8th international student edition edition, 5 2010.
- [15] Krishan K. Chawla. *Composite Materials: Science and Engineering (Materials Research and Engineering)*. Springer, 3rd edition, 5 2013.
- [16] J.L. Thomason. The influence of fibre length and concentration on the properties of glass fibre reinforced polypropylene. 6. the properties of injection moulded long fibre {PP} at high fibre content. *Composites Part A: Applied Science and Manufacturing*, 36(7):995 – 1003, 2005.
- [17] Shao-Yun Fu and Bernd Lauke. Effects of fiber length and fiber orientation distributions on the tensile strength of short-fiber-reinforced polymers. *Composites Science and Technology*, 56(10):1179 – 1190, 1996.
- [18] M. Miwa and N. Horiba. Effects of fibre length on tensile strength of carbon/glass fibre hybrid composites. *Journal of Materials Science*, 29(4):973–977, 1994.

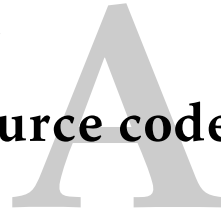
- [19] A. Bernasconi and F. Cosmi. Analysis of the dependence of the tensile behaviour of a short fibre reinforced polyamide upon fibre volume fraction, length and orientation. *Procedia Engineering*, 10(0):2129 – 2134, 2011. 11th International Conference on the Mechanical Behavior of Materials (ICM11).
- [20] A. C. Kak and Malcolm Slaney. *Principles of Computerized Tomographic Imaging*. IEEE Press, 1988.
- [21] O.S. Hopperstad and T. Børvik. *KT8306 Plasticity Theory - Lecture notes, Part 2*. Department of Structural Engineering, 2014.
- [22] PhD Bob McGinty. *Deformation Gradient*, accessed April 8, 2015. <http://www.continuummechanics.org/cm/deformationgradient.html>.
- [23] School of Engineering Brown University. *Continuum Mechanics - Kinematics*, accessed April 8, 2015. <http://www.brown.edu/Departments/Engineering/Courses/En221/Notes/Kinematics/Kinematics.htm>.
- [24] Robert Cook, David Malkus, Michael Plesha, and Robert Witt. *Concepts and applications of finite element analysis*. John Wiley and Sons. Inc., 2002.
- [25] E. A. de Souza Neto, D. Perć, and D. R. J. Owen. *Computational Methods for Plasticity: Theory and applications*. John Wiley & Sons, Ltd, 2008.
- [26] PhD Bob McGinty. *Stress Transformations*, accessed April 9, 2015. <http://www.continuummechanics.org/cm/stressxforms.html>.
- [27] Robert A. Adams, Christopher Essex, John Polking, Albert Boggess, David Arnold, and David C. Lay. *Differential equations, linear algebra and its applications*. Pearson Education Limited, 2012.
- [28] PhD Bob McGinty. *Coordinate Transformations*, accessed April 9, 2015. <http://www.continuummechanics.org/cm/coordxforms.html>.
- [29] G. E. P. Box and Mervin E. Muller. A note on the generation of random normal deviates. *Ann. Math. Statist.*, 29(2):610–611, 06 1958.

- [30] Dassault Systemes Simulia Corp. *ABAQUS 6.14 Documentation*. Dassault Systemes Simulia Corp., Providence, RI, USA, 2014.
- [31] Andreas Koukal. *Crash- und Bruchverhalten von Kunststoffen im Fußgängerschutz von Fahrzeugen*. PhD thesis, Technische Universität München, 2014.
- [32] Volume Graphics GmbH. *VGStudio MAX*, accessed May 18, 2015. <http://www.volumegraphics.com/products/vgstudio-max/basic-functionality/>.
- [33] P. Singh and M. R. Kamal. The effect of processing variables on microstructure of injection molded short fiber reinforced polypropylene composites. *Polymer Composites*, 10(5):344–351, 1989.
- [34] S.-Y. Fu, B. Lauke, E. Mäder, C.-Y. Yue, and X. Hu. Tensile properties of short-glass-fiber- and short-carbon-fiber-reinforced polypropylene composites. *Composites Part A: Applied Science and Manufacturing*, 31(10):1117 – 1125, 2000.
- [35] J. Karger-Kocsis, T. Harmia, and T. Czigány. Comparison of the fracture and failure behavior of polypropylene composites reinforced by long glass fibers and by glass mats. *Composites Science and Technology*, 54(3):287 – 298, 1995.
- [36] S. Barré and M.L. Benzeggagh. On the use of acoustic emission to investigate damage mechanisms in glass-fibre-reinforced polypropylene. *Composites Science and Technology*, 52(3):369 – 376, 1994.
- [37] K. Friedrich. Microstructural efficiency and fracture toughness of short fiber/thermoplastic matrix composites. *Composites Science and Technology*, 22(1):43 – 74, 1985.
- [38] N. Sato, T. Kurauchi, S. Sato, and O. Kamigaito. Microfailure behaviour of randomly dispersed short fibre reinforced thermoplastic composites obtained by direct sem observation. *Journal of Materials Science*, 26(14):3891–3898, 1991.

- [39] Norio Sato, Toshio Kurauchi, Shigeyuki Sato, and Osami Kamigaito. Mechanism of fracture of short glass fibre-reinforced polyamide thermoplastic. *Journal of Materials Science*, 19(4):1145–1152, 1984.
- [40] E. Mäder, K. Grundke, H.-J. Jacobasch, and G. Wachinger. Surface, interphase and composite property relations in fibre-reinforced polymers. *Composites*, 25(7):739 – 744, 1994. Third International Conference on Interfacial Phenomena in Composite Materials.
- [41] JL Thomason. The influence of fibre properties on the properties of glass-fibre-reinforced polyamide 6, 6. *Journal of composite materials*, 34(2):158–172, 2000.
- [42] J.L. Thomason and M.A. Vlug. Influence of fibre length and concentration on the properties of glass fibre-reinforced polypropylene: 1. tensile and flexural modulus. *Composites Part A: Applied Science and Manufacturing*, 27(6):477 – 484, 1996.
- [43] Bernd Lauke and Shao-Yun Fu. Strength anisotropy of misaligned short-fibre-reinforced polymers. *Composites Science and Technology*, 59(5):699 – 708, 1999.
- [44] Guo-Zheng Kang and Qing Gao. Tensile properties of randomly oriented short -al₂o₃ fiber reinforced aluminum alloy composites: Ii. finite element analysis for stress transfer, elastic modulus and stress–strain curve. *Composites Part A: Applied Science and Manufacturing*, 33(5):657 – 667, 2002.

Chapter

Source code



A.1 SFIBER.for

SFIBER.for

```
1 *****
2 *** "SFIBER.for" *****
3 *** Written by Ole Vestrum *****
4 *** Spring, 2015 *****
5 *****
6 !-----
7 !   SFIBER ()
8 !-----
9   SUBROUTINE SFIBER (STRESS,SM,F,dm,nf ,nlq)
10  implicit none
11  real*8 STRESS(nlq,6),SM(nlq,6),F(nlq,9)
12  real*8 STRESSFiber(nlq,6),dm(250)
13  integer nf,nlq,i,j
14  real*8 Vf,Ef
15  real*8 SMTRA(nlq,6,nf)
16  real*8 lambda(nlq,nf),SF(nlq,nf)
17  real*8 SMF(nlq,6,nf)
18  real*8 Q(600,9,625),Wf(600,625)
19  common /rotmat/ Q
20  common /weight/ Wf
21  !-----
22  !   EXECUTABLE STATEMENTS
23  !-----
24  !   Initializing values
25  !-----
26  Vf = dm(1)
27  Ef = dm(2)
28  !-----
29  !   Rotating the matrix stress (SM) into fiber subspace which is
30  !   spanned by the row space of Q. [ SMTRA = Q.SM.Q^T ]
```

```

31 | -----
32 |      do i=1,nf
33 |          do j=1,nlq
34 |              SMTRA(j,1,i)=Q(j,1,i)*Q(j,1,i)*SM(j,1)+Q(j,2,i)*SM(j,4)
35 |              +
36 |              +Q(j,3,i)*SM(j,6))+Q(j,2,i)*(Q(j,2,i)*SM(j,2)
37 |              +
38 |              +Q(j,1,i)*SM(j,4)+Q(j,3,i)*SM(j,5))
39 |              +
40 |              +Q(j,3,i)*(Q(j,3,i)*SM(j,3)+Q(j,1,i)*SM(j,6)
41 |              +
42 |              +Q(j,2,i)*SM(j,5))
43 |              SMTRA(j,2,i)=Q(j,4,i)*(Q(j,4,i)*SM(j,1)+Q(j,5,i)*SM(j,4)
44 |              +
45 |              +Q(j,6,i)*SM(j,6))+Q(j,5,i)*(Q(j,5,i)*SM(j,2)
46 |              +
47 |              +Q(j,4,i)*SM(j,4)+Q(j,6,i)*SM(j,5))
48 |              +
49 |              +Q(j,6,i)*(Q(j,6,i)*SM(j,3)+Q(j,4,i)*SM(j,6)
50 |              +
51 |              +Q(j,5,i)*SM(j,5))
52 |              SMTRA(j,3,i)=Q(j,7,i)*(Q(j,7,i)*SM(j,1)+Q(j,8,i)*SM(j,4)
53 |              +
54 |              +Q(j,9,i)*SM(j,6))+Q(j,8,i)*(Q(j,8,i)*SM(j,2)
55 |              +
56 |              +Q(j,7,i)*SM(j,4)+Q(j,9,i)*SM(j,5))
57 |              +
58 |              +Q(j,9,i)*(Q(j,9,i)*SM(j,3)+Q(j,7,i)*SM(j,6)
59 |              +
60 |              +Q(j,8,i)*SM(j,5))
61 |              SMTRA(j,4,i)=Q(j,4,i)*(Q(j,1,i)*SM(j,1)+Q(j,2,i)*SM(j,4)
62 |              +
63 |              +Q(j,3,i)*SM(j,6))+Q(j,5,i)*(Q(j,2,i)*SM(j,2)
64 |              +
65 |              +Q(j,1,i)*SM(j,4)+Q(j,3,i)*SM(j,5))
66 |              +
67 |              +Q(j,6,i)*(Q(j,3,i)*SM(j,3)+Q(j,1,i)*SM(j,6)
68 |              +
69 |              +Q(j,2,i)*SM(j,5))
70 |              SMTRA(j,5,i)=Q(j,7,i)*(Q(j,4,i)*SM(j,1)+Q(j,5,i)*SM(j,4)
71 |              +
72 |              +Q(j,6,i)*SM(j,6))+Q(j,8,i)*(Q(j,5,i)*SM(j,2)
73 |              +
74 |              +Q(j,4,i)*SM(j,4)+Q(j,6,i)*SM(j,5))
75 |              +
76 |              +Q(j,9,i)*(Q(j,6,i)*SM(j,3)+Q(j,4,i)*SM(j,6)
77 |              +
78 |              +Q(j,5,i)*SM(j,5))
79 |              SMTRA(j,6,i)=Q(j,1,i)*(Q(j,7,i)*SM(j,1)+Q(j,8,i)*SM(j,4)
80 |              +
81 |              +Q(j,9,i)*SM(j,6))+Q(j,2,i)*(Q(j,8,i)*SM(j,2)
82 |              +
83 |              +Q(j,7,i)*SM(j,4)+Q(j,9,i)*SM(j,5))
84 |              +
85 |              +Q(j,3,i)*(Q(j,9,i)*SM(j,3)+Q(j,7,i)*SM(j,6)
86 |              +
87 |              +Q(j,8,i)*SM(j,5))
88 |          enddo
89 |      enddo
90 | -----
91 |      ! Calculating the stretch introduced into the fiber by the
92 |      ! deformation gradient F. [ LAMBDA = SQRT( n.F^T.F.n ) ]
93 |      ! -----
94 |      do i=1,nf
95 |          do j=1,nlq
96 |              lambda(j,i) = sqrt(Q(j,1,i)*(F(j,1)*(F(j,1)*Q(j,1,i)
97 |              +
98 |              +F(j,2)*Q(j,2,i)+F(j,3)*Q(j,3,i))
99 |              +
100 |              +F(j,4)*(F(j,4)*Q(j,1,i)+F(j,5)*Q(j,2,i)
101 |              +
102 |              +F(j,6)*Q(j,3,i))+F(j,7)*(F(j,7)*Q(j,1,i)
103 |              +
104 |              +F(j,8)*Q(j,2,i)+F(j,9)*Q(j,3,i)))
105 |              +
106 |              +Q(j,2,i)*(F(j,2)*(F(j,1)*Q(j,1,i)
107 |              +
108 |              +F(j,2)*Q(j,2,i)+F(j,3)*Q(j,3,i))
109 |              +
110 |              +F(j,5)*(F(j,4)*Q(j,1,i)+F(j,5)*Q(j,2,i)
111 |              +
112 |              +F(j,6)*Q(j,3,i))+F(j,8)*(F(j,7)*Q(j,1,i)
113 |              +
114 |              +F(j,8)*Q(j,2,i)+F(j,9)*Q(j,3,i)))
115 |              +
116 |              +Q(j,3,i)*(F(j,3)*(F(j,1)*Q(j,1,i)

```

```

83      +          +F(j,2)*Q(j,2,i)+F(j,3)*Q(j,3,i))
84      +          +F(j,6)*(F(j,4)*Q(j,1,i)+F(j,5)*Q(j,2,i)
85      +          +F(j,6)*Q(j,3,i))+F(j,9)*(F(j,7)*Q(j,1,i)
86      +          +F(j,8)*Q(j,2,i)+F(j,9)*Q(j,3,i)))
87      +          +F(j,8)*Q(j,2,i)+F(j,9)*Q(j,3,i)))
88      +          +F(j,8)*Q(j,2,i)+F(j,9)*Q(j,3,i)))
89      +          +F(j,8)*Q(j,2,i)+F(j,9)*Q(j,3,i)))
90      +          +F(j,8)*Q(j,2,i)+F(j,9)*Q(j,3,i)))
91      +          +F(j,8)*Q(j,2,i)+F(j,9)*Q(j,3,i)))
92      +          +F(j,8)*Q(j,2,i)+F(j,9)*Q(j,3,i)))
93      +          +F(j,8)*Q(j,2,i)+F(j,9)*Q(j,3,i)))
94      +          +F(j,8)*Q(j,2,i)+F(j,9)*Q(j,3,i)))
95      +          +F(j,8)*Q(j,2,i)+F(j,9)*Q(j,3,i)))
96      +          +F(j,8)*Q(j,2,i)+F(j,9)*Q(j,3,i)))
97      +          +F(j,8)*Q(j,2,i)+F(j,9)*Q(j,3,i)))
98      +          +F(j,8)*Q(j,2,i)+F(j,9)*Q(j,3,i)))
99      +          +F(j,8)*Q(j,2,i)+F(j,9)*Q(j,3,i)))
100     +          +F(j,8)*Q(j,2,i)+F(j,9)*Q(j,3,i)))
101     +          +F(j,8)*Q(j,2,i)+F(j,9)*Q(j,3,i)))
102     +          +F(j,8)*Q(j,2,i)+F(j,9)*Q(j,3,i)))
103     +          +F(j,8)*Q(j,2,i)+F(j,9)*Q(j,3,i)))
104     +          +F(j,8)*Q(j,2,i)+F(j,9)*Q(j,3,i)))
105     +          +F(j,8)*Q(j,2,i)+F(j,9)*Q(j,3,i)))
106     +          +F(j,8)*Q(j,2,i)+F(j,9)*Q(j,3,i)))
107     +          +F(j,8)*Q(j,2,i)+F(j,9)*Q(j,3,i)))
108     +          +F(j,8)*Q(j,2,i)+F(j,9)*Q(j,3,i)))
109     +          +F(j,8)*Q(j,2,i)+F(j,9)*Q(j,3,i)))
110     +          +F(j,8)*Q(j,2,i)+F(j,9)*Q(j,3,i)))
111     +          +F(j,8)*Q(j,2,i)+F(j,9)*Q(j,3,i)))
112     +          +F(j,8)*Q(j,2,i)+F(j,9)*Q(j,3,i)))
113     +          +F(j,8)*Q(j,2,i)+F(j,9)*Q(j,3,i)))
114     +          +F(j,8)*Q(j,2,i)+F(j,9)*Q(j,3,i)))
115     +          +F(j,8)*Q(j,2,i)+F(j,9)*Q(j,3,i)))
116     +          +F(j,8)*Q(j,2,i)+F(j,9)*Q(j,3,i)))
117     +          +F(j,8)*Q(j,2,i)+F(j,9)*Q(j,3,i)))
118     +          +F(j,8)*Q(j,2,i)+F(j,9)*Q(j,3,i)))
119     +          +F(j,8)*Q(j,2,i)+F(j,9)*Q(j,3,i)))
120     +          +F(j,8)*Q(j,2,i)+F(j,9)*Q(j,3,i)))
121     +          +F(j,8)*Q(j,2,i)+F(j,9)*Q(j,3,i)))
122     +          +F(j,8)*Q(j,2,i)+F(j,9)*Q(j,3,i)))
123     +          +F(j,8)*Q(j,2,i)+F(j,9)*Q(j,3,i)))
124     +          +F(j,8)*Q(j,2,i)+F(j,9)*Q(j,3,i)))
125     +          +F(j,8)*Q(j,2,i)+F(j,9)*Q(j,3,i)))
126     +          +F(j,8)*Q(j,2,i)+F(j,9)*Q(j,3,i)))
127     +          +F(j,8)*Q(j,2,i)+F(j,9)*Q(j,3,i)))
128     +          +F(j,8)*Q(j,2,i)+F(j,9)*Q(j,3,i)))
129     +          +F(j,8)*Q(j,2,i)+F(j,9)*Q(j,3,i)))
130     +          +F(j,8)*Q(j,2,i)+F(j,9)*Q(j,3,i)))
131     +          +F(j,8)*Q(j,2,i)+F(j,9)*Q(j,3,i)))
132     +          +F(j,8)*Q(j,2,i)+F(j,9)*Q(j,3,i)))
133     +          +F(j,8)*Q(j,2,i)+F(j,9)*Q(j,3,i)))
134     +          +F(j,8)*Q(j,2,i)+F(j,9)*Q(j,3,i)))

```

```

135 +           +Q(j,6,i)*(Q(j,3,i)*SMTRA(j,4,i)
136 +           +Q(j,6,i)*SMTRA(j,2,i)+Q(j,9,i)*SMTRA(j,5,i))
137 +           +Q(j,9,i)*(Q(j,3,i)*SMTRA(j,6,i)
138 +           +Q(j,6,i)*SMTRA(j,5,i)+Q(j,9,i)*SMTRA(j,3,i))
139 SMF(j,4,i)=Q(j,2,i)*(Q(j,1,i)*SMTRA(j,1,i)
140 +           +Q(j,4,i)*SMTRA(j,4,i)+Q(j,7,i)*SMTRA(j,6,i))
141 +           +Q(j,5,i)*(Q(j,1,i)*SMTRA(j,4,i)
142 +           +Q(j,4,i)*SMTRA(j,2,i)+Q(j,7,i)*SMTRA(j,5,i))
143 +           +Q(j,8,i)*(Q(j,1,i)*SMTRA(j,6,i)
144 +           +Q(j,4,i)*SMTRA(j,5,i)+Q(j,7,i)*SMTRA(j,3,i))
145 SMF(j,5,i)=Q(j,3,i)*(Q(j,2,i)*SMTRA(j,1,i)
146 +           +Q(j,5,i)*SMTRA(j,4,i)+Q(j,8,i)*SMTRA(j,6,i))
147 +           +Q(j,6,i)*(Q(j,2,i)*SMTRA(j,4,i)
148 +           +Q(j,5,i)*SMTRA(j,2,i)+Q(j,8,i)*SMTRA(j,5,i))
149 +           +Q(j,9,i)*(Q(j,2,i)*SMTRA(j,6,i)
150 +           +Q(j,5,i)*SMTRA(j,5,i)+Q(j,8,i)*SMTRA(j,3,i))
151 SMF(j,6,i)=Q(j,1,i)*(Q(j,3,i)*SMTRA(j,1,i)
152 +           +Q(j,6,i)*SMTRA(j,4,i)+Q(j,9,i)*SMTRA(j,6,i))
153 +           +Q(j,4,i)*(Q(j,3,i)*SMTRA(j,4,i)
154 +           +Q(j,6,i)*SMTRA(j,2,i)+Q(j,9,i)*SMTRA(j,5,i))
155 +           +Q(j,7,i)*(Q(j,3,i)*SMTRA(j,6,i)
156 +           +Q(j,6,i)*SMTRA(j,5,i)+Q(j,9,i)*SMTRA(j,3,i))
157         enddo
158     enddo
159 !-----
160 !           Summing fiber families' stress contributions.
161 !-----
162     STRESSFiber = 0.0d0
163     do i=1,nf
164         do j=1,nlq
165             STRESSFiber(j,1) = STRESSFiber(j,1)+SMF(j,1,i)*Wf(j,i)
166             STRESSFiber(j,2) = STRESSFiber(j,2)+SMF(j,2,i)*Wf(j,i)
167             STRESSFiber(j,3) = STRESSFiber(j,3)+SMF(j,3,i)*Wf(j,i)
168             STRESSFiber(j,4) = STRESSFiber(j,4)+SMF(j,4,i)*Wf(j,i)
169             STRESSFiber(j,5) = STRESSFiber(j,5)+SMF(j,5,i)*Wf(j,i)
170             STRESSFiber(j,6) = STRESSFiber(j,6)+SMF(j,6,i)*Wf(j,i)
171         enddo
172     enddo
173 !-----
174 !           Applying a law of mixture
175 !-----
176     do j=1,nlq
177         STRESS(j,1) = Vf*STRESSFiber(j,1)+(1.0-Vf)*SM(j,1)
178         STRESS(j,2) = Vf*STRESSFiber(j,2)+(1.0-Vf)*SM(j,2)
179         STRESS(j,3) = Vf*STRESSFiber(j,3)+(1.0-Vf)*SM(j,3)
180         STRESS(j,4) = Vf*STRESSFiber(j,4)+(1.0-Vf)*SM(j,4)
181         STRESS(j,5) = Vf*STRESSFiber(j,5)+(1.0-Vf)*SM(j,5)
182         STRESS(j,6) = Vf*STRESSFiber(j,6)+(1.0-Vf)*SM(j,6)
183     enddo
184 !-----
185 !           End subroutine
186 !-----

```



```

187     RETURN
188     END SUBROUTINE SFIBER

```

A.2 SFD.for

SFD.for

```

1  *****
2  *** "SFD.for" *****
3  *** Written by Ole Vestrum *****
4  *** Spring, 2015 *****
5  *****
6  !-----
7  !   SFD()
8  !-----
9  !!! Material parameter overview !!!!!!!!!!!!!!!!!!!!!!!!!!!!!!!!!!!!!!!
10 !!!   HARD VARIABLES                SOFT VARIABLES (Case specific)  !!!
11 !!! |<----->|<----->|!!!
12 !!! 1   2   3   4   5   6   7   8   9   10  !!!
13 !!! Vf,  Ef,  kf,  CASEFLAG, var1, var2, var3, var4, var5, var6 !!!
14 !!! !!!!!!!!!!!!!!!!!!!!!!!!!!!!!!!!!!!!!!!!!!!!!!!!!!!!!!!!!!!!!!!
15   SUBROUTINE SFD(dm, nf, nlq)
16     implicit none
17     real*8 dm(250)
18     integer nf, nlq, sqnf
19     real*8 theta(nlq, nf), phi(nlq, nf), Pl, df1,
20           2      df2, Wftmp(nlq,nf), tmp1, tmp2, phsta, phend, phinc, tol,
21           3      thtmp(nf), phtmp(nf), tmp3, tmp4, tmp5, tmp6, tmp7, tmp8,
22           4      tmp9, tmp10, tmp11, tmp12, tmp13, random, U1, U2, Z, seed,
23           5      check
24     real*8 thmin, thmax, phmin, phmax
25     integer i, j, n, m, FDFLAG
26     real*8 Q(600,9,625), Wf(600, 625)
27     PARAMETER(PI=4*atan(1.0d0), tol=1e-5)
28     common /rotmat/ Q
29     common /weight/ Wf
30 !-----
31 !   EXECUTABLE STATEMENTS
32 !-----
33 !   Initializing values
34 !-----
35     FDFLAG = int(dm(4))
36 !-----
37 !   Selecting fibre distribution case.
38 !-----
39     select case (FDFLAG)
40 !-----
41 !       Case 1: Constant theta and phi values
42 !         dm(5) = constant, theta

```

```

43 !      dm(6) = constant, phi
44 !-----
45 case (1)
46     tmp1 = 1/real(nf)
47     do j=1,nlq
48         do i=1,nf
49             theta(j,i) = dm(5)
50             phi(j,i)   = dm(6)
51             Wf(j,i)    = tmp1
52         end do
53     end do
54 !-----
55 !      Case 2: Gaussian distributed theta and constant phi
56 !      dm(5) = mu, theta
57 !      dm(6) = std, theta
58 !      dm(7) = range cut off, theta
59 !      dm(8) = constant, phi
60 !-----
61 case (2)
62     thmin = dm(5) - dm(7)*dm(6)
63     thmax = dm(5) + dm(7)*dm(6)
64     thinc = (thmax - thmin)/(nf-1)
65     df1 = (1/(dm(6)*sqrt(2*PI)))
66     df2 = (2*dm(6)**2)
67     do j=1,nlq
68         tmp1 = 0
69         do i=1,nf
70             theta(j,i) = thmin + thinc*(i-1)
71             phi(j,i)   = dm(8)
72             Wftmp(j,i) = df1*exp(-(theta(j,i)-dm(5))**2/df2)
73             tmp1       = tmp1 + Wftmp(j,i)
74         end do
75         tmp2 = 1/tmp1
76         do i=1,nf
77             Wf(j,i) = Wftmp(j,i)*tmp2
78             tmp1 = theta(j,i)
79             theta(j,i) = tmp1 - 180*floor(tmp1/180)
80         end do
81     end do
82 !-----
83 !      Case 3: Constant theta and gaussian distributed phi
84 !      dm(5) = constant, theta
85 !      dm(6) = mu, phi
86 !      dm(7) = std, phi
87 !      dm(8) = range cut off, phi
88 !-----
89 case (3)
90     phmin = dm(6) - dm(8)*dm(7)
91     phmax = dm(6) + dm(8)*dm(7)
92     phinc = (phmax - phmin)/(nf-1)
93     df1 = (1/(dm(7)*sqrt(2*PI)))
94     df2 = (2*dm(7)**2)

```

```

95         do j=1,nlq
96             tmp1 = 0
97             do i=1,nf
98                 theta(j,i) = dm(5)
99                 phi(j,i) = phmin + phinc*(i-1)
100                Wftmp(j,i) = df1*exp(-(phi(j,i)-dm(6))*2/df2)
101                tmp1 = tmp1 + Wftmp(j,i)
102            end do
103            tmp2 = 1/tmp1
104            do i=1,nf
105                Wf(j,i) = Wftmp(j,i)*tmp2
106                tmp1 = phi(j,i)
107                phi(j,i) = tmp1 - 180*floor(tmp1/180)
108            end do
109        end do
110 !-----
111 ! Case 4: Bivariate gaussian distributed values for theta and phi
112 ! dm(5) = mu, theta
113 ! dm(6) = std, theta
114 ! dm(7) = range cut off, theta
115 ! dm(8) = mu, phi
116 ! dm(9) = std, phi
117 ! dm(10) = range cut off, phi
118 ! dm(11) = C11, dm(6)**2
119 ! dm(12) = C12
120 ! dm(13) = C21
121 ! dm(14) = C22, dm(9)**2
122 !-----
123     case (4)
124         tmp1 = real(nf)
125         sqnf = int(sqrt(tmp1))
126         nf = int(sqnf**2)
127         thmin = dm(5) - dm(7)*dm(6)
128         thmax = dm(5) + dm(7)*dm(6)
129         thinc = (thmax - thmin) / (sqnf-1)
130         phmin = dm(8) - dm(10)*dm(9)
131         phmax = dm(8) + dm(10)*dm(9)
132         phinc = (phmax - phmin) / (sqnf-1)
133
134         do j=1,nlq
135             do i=1,sqnf
136                 thtmp(i) = thmin + thinc*(i-1)
137                 phtmp(i) = phmin + phinc*(i-1)
138             end do
139             do i=1,sqnf
140                 tmp1 = phtmp(i)
141                 phtmp(i) = tmp1 - 180*floor(tmp1/180)
142                 tmp1 = thtmp(i)
143                 thtmp(i) = tmp1 - 180*floor(tmp1/180)
144             end do
145             i = 1
146         do n=1,sqnf

```

```

147         do m=1,sqnf
148             phi(j,i) = phtmp(n)
149             theta(j,i) = thtmp(m)
150             i = i + 1
151         end do
152     end do
153 end do
154 do j=1,nlq
155     tmp1 = 1/(2*PI*sqrt(dm(11)*dm(14)-dm(13)*dm(12)))
156     tmp13 = 0
157     do i=1,nf
158         tmp2 = (dm(5) - theta(j,i))
159         tmp3 = (dm(13)*(dm(8)/2 - phi(j,i)/2))
160         tmp4 = (dm(11)*dm(14) - dm(12)*dm(13))
161         tmp5 = (dm(14)*(dm(5)/2 - theta(j,i)/2))
162         tmp6 = (dm(11)*dm(14) - dm(12)*dm(13))
163         tmp7 = (dm(8) - phi(j,i))
164         tmp8 = (dm(11)*(dm(8)/2 - phi(j,i)/2))
165         tmp9 = (dm(11)*dm(14) - dm(12)*dm(13))
166         tmp10 = (dm(12)*(dm(5)/2 - theta(j,i)/2))
167         tmp11 = (dm(11)*dm(14) - dm(12)*dm(13))
168         tmp12 = tmp2*(tmp3/tmp4 - tmp5/tmp6) -
169             2 tmp7*(tmp8/tmp9 - tmp10/tmp11)
170         Wftmp(j,i) = tmp1*exp(tmp12)
171         tmp13 = tmp13 + Wftmp(j,i)
172     end do
173     tmp1 = 1/tmp13
174     do i=1,nf
175         Wf(j,i) = Wftmp(j,i)*tmp1
176     end do
177 end do
178 tmp13 = 0.0d0
179 do j=1,nlq
180     do i=1,nf
181         tmp13 = tmp13 + Wf(j,i)
182     end do
183 end do
184 ! -----
185 ! Case 5: Monte Carlo case
186 ! dm(5) = mu, theta
187 ! dm(6) = std, theta
188 ! dm(7) = seed value, theta
189 ! dm(8) = constant, phi
190 ! -----
191 case (5)
192     tmp1 = 1/real(nf)
193     do j=1,nlq
194         do i=1,nf
195             U1 = random(int(dm(7)))
196             U2 = random(int(dm(7)))
197             Z = sqrt(-2*log(U1))*cos(2*PI*U2)
198             theta(j,i) = dm(5)+dm(6)*Z

```

```

199         phi(j,i) = dm(8)
200         Wf(j,i) = tmp1
201     end do
202     do i=1,nf
203         if (theta(j,i).LT.0.0) then
204             tmp1 = theta(j,i)
205             theta(j,i) = tmp1 + 180.0*(abs(int(tmp1/180))+1)
206         else if (theta(j,i).GT.180.0) then
207             tmp1 = theta(j,i)
208             theta(j,i) = tmp1 - 180.0*(abs(int(tmp1/180)))
209         end if
210     end do
211 end do
212 !-----
213 ! Case 6: Uniform theta and constant phi
214 ! dm(5) = constant, phi
215 !-----
216 case (6)
217     tmp1 = 1.0d0/real(nf)
218     thmin = 0.0d0
219     thmax = 180.0d0
220     thinc = (thmax - thmin) / (nf-1)
221
222     do i=1,nf
223         do j=1,nlq
224             phi(j,i) = dm(5)
225             theta(j,i) = thmin + thinc*(i-1)
226             Wf(j,i) = tmp1
227         end do
228     end do
229 case default
230 end select
231 !-----
232 ! Creating directional vectors
233 !-----
234     tmp2 = PI/180.0
235     do i=1,nf
236         do j=1,nlq
237             tmp3 = phi(j,i)*tmp2
238             tmp4 = theta(j,i)*tmp2
239             Q(j,1,i) = sin(tmp3)*cos(tmp4)
240             Q(j,2,i) = sin(tmp3)*sin(tmp4)
241             Q(j,3,i) = cos(tmp3)
242             tmp1 = 1/sqrt(Q(j,1,i)**2 + Q(j,2,i)**2 + Q(j,3,i)**2)
243             Q(j,1,i) = Q(j,1,i)*tmp1
244             Q(j,2,i) = Q(j,2,i)*tmp1
245             Q(j,3,i) = Q(j,3,i)*tmp1
246         end do
247     end do
248 !-----
249 ! Creating fiber coordinate systems and transformation matrices
250 !-----

```

```

251 | -----
252 |      do i=1,nf
253 |          do j=1,ntq
254 |              check = abs(Q(j,1,i))
255 |              if ((CHECK.GE.(1.0-tol)).and.(CHECK.LE.(1.0+tol))) then
256 |                  Q(j,1,i) = 1.0d0
257 |                  Q(j,2,i) = 0.0d0
258 |                  Q(j,3,i) = 0.0d0
259 |                  Q(j,4,i) = 0.0d0
260 |                  Q(j,5,i) = 1.0d0
261 |                  Q(j,6,i) = 0.0d0
262 |                  Q(j,7,i) = 0.0d0
263 |                  Q(j,8,i) = 0.0d0
264 |                  Q(j,9,i) = 1.0d0
265 |              else
266 |                  Q(j,7,i) = 0.0d0
267 |                  Q(j,8,i) = -Q(j,3,i)
268 |                  Q(j,9,i) = Q(j,2,i)
269 |                  tmp1 = 1/sqrt(Q(j,7,i)**2 + Q(j,8,i)**2 + Q(j,9,i)**2)
270 |                  Q(j,8,i) = Q(j,8,i)*tmp1
271 |                  Q(j,9,i) = Q(j,9,i)*tmp1
272 |                  Q(j,4,i) = Q(j,3,i)*Q(j,8,i)-Q(j,2,i)*Q(j,9,i)
273 |                  Q(j,5,i) = Q(j,1,i)*Q(j,9,i)-Q(j,3,i)*Q(j,7,i)
274 |                  Q(j,6,i) = Q(j,2,i)*Q(j,7,i)-Q(j,1,i)*Q(j,8,i)
275 |              end if
276 |          end do
277 |      end do
278 | -----
279 |      End subroutine
280 | -----
281 |      RETURN
282 |      END SUBROUTINE SFD

```